UNIVERSITY OF CALIFORNIA, SAN DIEGO

Stability and asymptotic analyses of effects of buoyancy on reactive flows

A dissertation submitted in partial satisfaction of the
requirements for the degree
Doctor of Philosophy

in

Engineering Sciences (Aerospace Engineering)

by

Daniel Moreno Boza

Committee in charge:

Professor Antonio L. Sánchez, Chair
Professor Henry D. I. Abarbanel
Professor David Saintillan
Professor Sutanu Sarkar
Professor Forman A. Williams

2017

The dissertation of Daniel Moreno Boza is approved, and it is acceptable in quality and form for publication on microfilm and electronically:

_____

_____

_____

_____

_____

Chair

University of California, San Diego

2017

DEDICATION

To my parents Salvador and Remedios.

EPIGRAPH

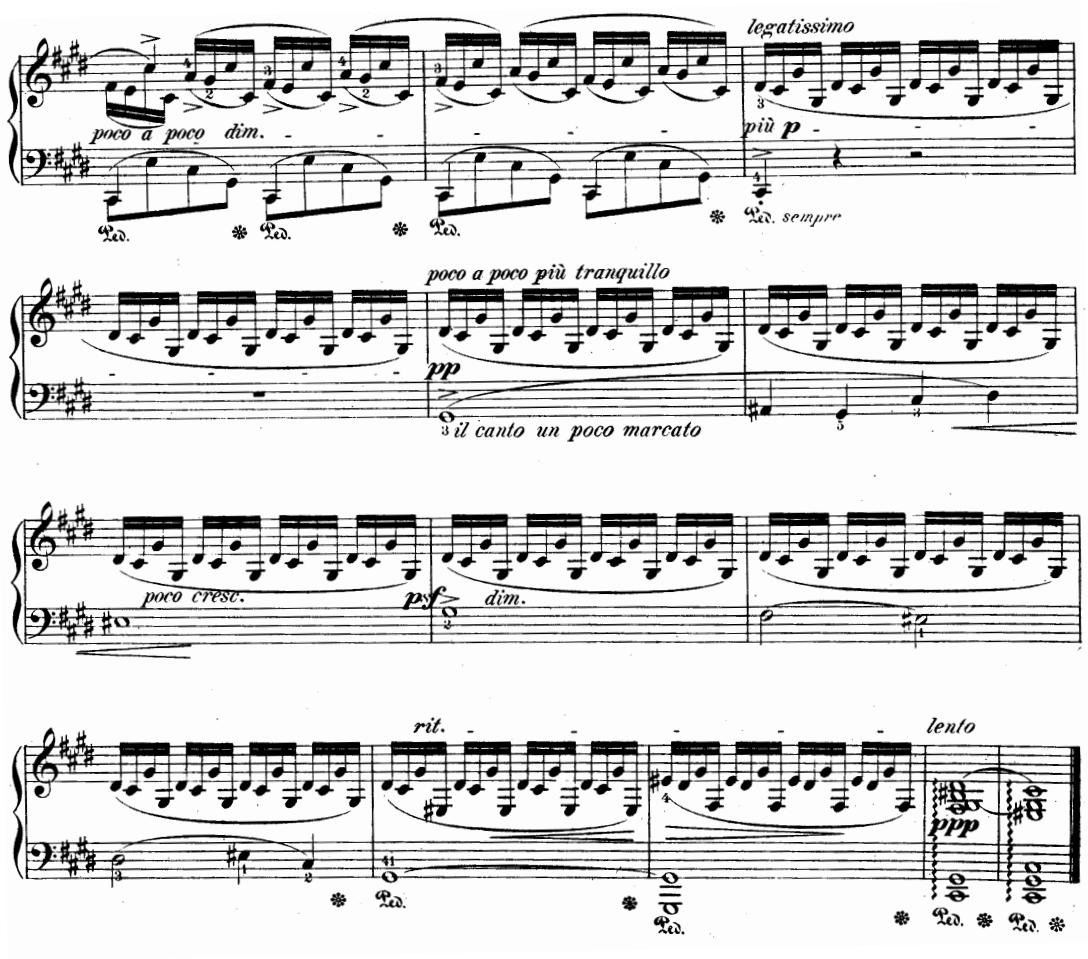

Ending section of Frédéric Chopin's
Fantaisie–Impromptu in C-sharp minor, Op. posth. 66

TABLE OF CONTENTS

LIST OF FIGURES

LIST OF TABLES

ACKNOWLEDGEMENTS

During my stay at UC San Diego, I have had the chance to look at some relevant, challenging and beautiful, at least from a mathematical point of view, problems in Fluid Mechanics and Combustion. It has been thanks to the guidance and support of Professor Antonio Sánchez, who I now see as a role model in Science, that I have become more proficient in analysing the underlying phsysics of the problems I have looked into. His admirable ability to identify the relevant (temporal and spatial) scalings of almost any problem in Fluid Mechanics, combined with outstanding mathematical treatment, has often served as an inspiration for me.

Thanks to Professor Forman A. Williams, who has been always happy to help with any bump in the road I may have found. His office has been always opened to discuss any aspect of the work that I am presenting in this Dissertation, providing a different point of view or adding valuable content to it. Attending some of his Combustion lectures at UCSD has also been a privilege for which I am truly grateful.

Special thanks must go to Wilfried Coenen, who I met back in Madrid and joined us later in San Diego. He has been always willing to share his knowlegde with me in various different aspects: from numerical methods using our beloved FreeFem++ opensource code and its tricks to the importance of being organized and consistent at work. Informal discussions outside the office about life have also been joyful and entertaining.

I am equally thankful to my coauthors, Amable Liñán, Jaime Carpio, Immaculada Iglesias and Alejandro Sevilla who have provided valuable insight to my work.

Chapter 1, in part, has been published in the *Journal of Fluid Mechanics*, "Diffusion-flame flickering as a hydrodynamic global mode", by D. Moreno-Boza, W. Coenen, A. Sevilla, J. Carpio, A. L. Sánchez and A. Liñán (2016) **798**, 997-1014. The dissertation author is the primary investigator in this publication.

Chapter 2 is in preparation for publication in *Combustion and flame*, where the dissertation autor is to be the primary investigator. The experiments depicted in this Chapter have been performed by Wilfried Coenen.

Chapter 3, in part, has been published in *Combustion Theory and Modelling*, "The slowly

reacting mode of combustion of gaseous mixtures in spherical vessels. Part 1: Transient analysis and explosion limits", by A. Liñán, D. Moreno-Boza, I. Iglesias, A. L. Sánchez and F. A. Williams (2016) **20**(6), 1010-1028. The dissertation author is the primary investigator in this publication.

Chapters 4 and 5, in part, has been published in *Combustion Theory and Modelling*, "The slowly reacting mode of combustion of gaseous mixtures in spherical vessels. Part 2: Buoyancy-induced motion and its effect on the explosion limits", by A. L. Sánchez, I. Iglesias, D. Moreno-Boza, A. Liñán and F. A. Williams (2016) **20**(6), 1029-1045. The dissertation author is the primary investigator in this publication.

Chapter 6, in part, has been published in the *Internationl Journal of Heat and Mass Transfer*, "Thermal explosions in spherical vessels at large Rayleigh numbers", by I. Iglesias, D. Moreno-Boza, A. L. Sánchez, A. Liñán and F. A. Williams (2017) **115**, 1042-1053. The dissertation author is the primary investigator in this publication.

Appendix A, in part, has been published in *Combustion and Flame*, "Large-activa-tion-energy analysis of gaseous reacting flow in pipes", by D. Moreno-Boza, I. Iglesias and A. L. Sánchez (2017) **178**, 217-224. The dissertation author is the primary investigator in this publication.

La Jolla, California. October, 2017

VITA

December, 2013	Ingeniero Industrial, Universidad de Málaga, Spain.
2014-2015	Research assistant, Depto. de Ingeniería Térmica y de Fluidos, Universidad Carlos III de Madrid, Spain.
2016	Teaching assistant (MAE 210C), Dept. of Mechanical and Aerospace Engineering, University of California, San Diego.
July, 2016	Ms. C. in Engineering Sciences (Aerospace Engineering), Dept. of Mechanical and Aerospace Engineering, University of California, San Diego.
January, 2017	Advancement to Ph. D. Candidacy, Dept. of Mechanical and Aerospace Engineering, University of California, San Diego.
2017	Teaching assistant (MAE 101A), Dept. of Mechanical and Aerospace Engineering, University of California, San Diego.
2017	Teaching assistant (MAE 212), Dept. of Mechanical and Aerospace Engineering, University of California, San Diego.
2017	Ph. D. in Engineering Sciences (Aerospace Engineering), Dept. of Mechanical and Aerospace Engineering, University of California, San Diego.

PUBLICATIONS

Moreno-Boza D., Coenen W., Sevilla A., Carpio J., Sánchez A.L. & Liñán, A. 2016 Diffusion-flame flickering as a hydrodynamic global mode. *J. Fluid. Mech.* **798**, 997-1014.

Liñán, A., Moreno-Boza, D., Iglesias, I., Sánchez, A.L. & Williams, F.A., 2016 The slowly reacting mode of combustion of gaseous mixtures in spherical vessels. Part 1: Transient analysis and explosion limits. *Combust. Theor. Model.*, **20**(6), 1010-1028.

Sánchez, A.L., Iglesias, I., Moreno-Boza, D., Liñán, A. & Williams, F.A., 2016 The slowly reacting mode of combustion of gaseous mixtures in spherical vessels. Part 2: Buoyancy-induced motion and its effect on the explosion limits. *Combust. Theor. Model.*, **20**(6), 1029-1045.

Moreno-Boza, D., Iglesias, I. & Sánchez, A.L., 2017 Large-activation-energy analysis of gaseous reacting flow in pipes. *Combust. Flame*, **178**, 217-224.

Iglesias, I., Moreno-Boza, D., Sánchez, A. L., Liñán, A. & Williams, F.A., 2017 Thermal explosions in spherical vessels at large Rayleigh numbers. *Int. J. Heat Mass Transfer*, **115**, 1042-1053.

ABSTRACT OF THE DISSERTATION

Stability and asymptotic analyses of effects of buoyancy on reactive flows

by

Daniel Moreno Boza

Doctor of Philosophy in Engineering Sciences (Aerospace Engineering)

University of California San Diego, 2017

Professor Antonio L. Sánchez, Chair

Asymptotic methods and experimental techniques have been used in combination with direct numerical simulations and stability analyses to investigate effects of buoyancy-driven motion in two different reactive problems, namely, flickering of nonpremixed diffusion flames in open atmospheres and slowly reacting combustion of confined mixtures. A brief description of these two separate topics is given below.

Part I of this dissertation deals with the flickering of jet diffusion flames and the puffing of liquid-fuel pool fires. Both phenomena are a manifestation of an axisymmmetric global hydrodynamic instability driven by the interactions of the buoyancy force with the density differences induced by the chemical heat release, which occurs in the flame sheet separating the fuel and oxidizer domains. For these flows, the predictive capability of local quasi-parallel stability analyses is limited by the non-slender character of the resulting eigenmodes, so that a biglobal analysis is needed to accurately determine marginal instability conditions and resulting frequencies. The results for jet diffusion flames, including the Froude number/Reynolds number instability boundaries for different fuel-feed dilutions, are compared with direct numerical simulations, giving good

agreement for the range of conditions explored in our study. For liquid-fuel pool fires, the stability analysis provides the critical value of the Rayleigh number at the onset of the puffing instability. The predictions for different liquid fuels are compared with the results obtained in small-scale laboratory experiments.

Part II is concerned with the "slowly reacting" mode of combustion, and its thermal-explosion limits, of an initially cold gaseous mixture enclosed in a spherical vessel with a constant wall temperature, a relevant problem in connection with the safe storage and transportation of reactant gas mixtures. Following Frank-Kamenetskii's seminal analysis of this problem, the strong temperature dependence of the effective overall reaction rate is taken into account by using a single-reaction model with an Arrhenius rate having a large activation energy, resulting in a critical value Da_c of the controlling Damköhler number above which the slowly reacting mode of combustion no longer exists. A Rayleigh number Ra based on the relevant density difference is seen to measure the relative effect of natural convection. Our numerical computations indicate that the value of Da_c increases with Ra as a result of the enhanced heat-transfer rate. Specific consideration is given to the flow structure in the asymptotic limits $Ra \ll 1$ and $Ra \gg 1$, which yield accurate predictions of critical explosion conditions. For completeness, the application of Frank-Kamenetskii's ideas to the problem of flow of a reactive mixture in a pipe is presented in an appendix for the case of buoyancy-free conditions.

Part I

Global instabilities of buoyant diffusion flames in open atmospheres

Brief overview

Because of their relevance in combustion applications, there is interest in understanding the stability characteristics of low-Mach number gaseous flows with significant density changes for moderately large values of the relevant Reynolds number in the presence of gravity. For particular flow configurations, quasi-parallel linear, spatiotemporal stability analyses suffice to clarify the stability properties of the resulting flows, including their convective/absolute instability character. In other occasions, the predicted wavelength of the eigenmodes (perturbations) is comparable to the flow-development length itself and therefore the perturbation does not *see* the flow as slender anymore. A global linear stability analysis is thus required to ascertain the stability characteristics of such flows.

In Chapters 1 and 2, we apply the latter technique to the analysis of the periodic flow state that characterizes buoyancy-dominated jet diffusion flames, often referred to as *flame flickering*; and *pool-fire puffing*, a similar periodic behaviour found in vaporizing combustible pools, respectively. While early theoretical work assumed a convective instability, later experimental observations suggested that the flame flickering phenomenon was associated instead with a globally excited oscillation forced by a region of absolutely unstable flow near the base of the jet exit, a statement confirmed in Chapter 1 by numerical results. The same underlying instability mechanisms are present in the case of buoyancy-dominated pool-fire combustion, which is evidenced experimentally and assessed numerically through Chapter 2.

Chapter 1

Diffusion-flame flickering as a hydrodynamic global mode

In the present chapter we employ a linear global stability analysis to investigate buoyancy-induced flickering of axisymmetric laminar jet diffusion flames as a hydrodynamic global mode. The instability-driving interactions of the buoyancy force with the density differences induced by the chemical heat release are described in the infinitely fast reaction limit for unity Lewis numbers of the reactants. The analysis determines the critical conditions at the onset of the linear global instability as well as the Strouhal number of the associated oscillations in terms of the governing parameters of the problem. Marginal instability boundaries are delineated in the Froude-number/Reynolds-number plane for different fuel-jet dilutions. The results of the global stability analysis are compared with direct numerical simulations of time-dependent axisymmetric jet flames and also with results of a local spatio-temporal stability analysis.

1.1 Introduction

At sufficiently low Froude numbers, jet diffusion flames undergo a bifurcation to a periodic flow state referred to as *flame flicker* (Chamberlin & Rose, 1948). The associated frequencies observed in laboratory-scale experiments are in the range of 10 to 20 Hz (Chen *et al.*, 1988). The role of buoyancy as the driving mechanism was recognized in the early theoretical analysis of Buckmaster & Peters (1986), who postulated that the flickering was associated with a modified Kelvin-Helmholtz instability of the annular flow induced by buoyancy in the envelope of hot gases surrounding the jet flame. By performing an inviscid, parallel flow stability analysis of a simplified self-similar model problem (the so-called infinite candle) they were able to determine an expression for the flicker frequency, which was predicted to vary with the one fourth power of the streamwise

distance. This dependence, although weak, was readily recognized as a weakness of the results (Mahalingam *et al.*, 1991). As pointed out by Buckmaster & Peters (1986), a "detailed viscous stability analysis of the complete flow field" could help to examine the validity of the results of their simplified study, although they recognized that the suggested analysis was "a formidable undertaking" at the time. As a result of the increase in computer power and of the development of robust numerical techniques that have occurred in the intervening time, such an analysis can be performed nowadays with reasonable computational cost, that being the main purpose of the present work.

While the early theoretical work assumed a convective instability (Buckmaster & Peters, 1986), later experimental observations by Lingens *et al.* (1996*b*) and Maxworthy (1999) suggested that the flame flickering phenomenon was associated instead with a globally excited oscillation forced by a region of absolutely unstable flow near the base of the jet exit (see also Cetegen & Dong, 2000). These findings were later supported by experiments (Juniper *et al.*, 2009), direct numerical simulations (DNS) (Jiang & Luo, 2000; Juniper *et al.*, 2009; Boulanger, 2010) and by local linear stability analyses assuming nearly parallel flow (Lingens *et al.*, 1996*a*; See & Ihme, 2014). The present work is different from these previous attempts, in that it employs a linear global stability analysis to study the problem. The method has been used successfully in recent years to investigate the stability of nonbuoyant jet flows, including constant-density jets (Garnaud *et al.*, 2013*a*,*b*), compressible high-speed jets (Nichols & Lele, 2011), and light jets at low Mach numbers (Lesshafft *et al.*, 2015; Coenen *et al.*, 2016). The global instability of reacting jets has been considered recently by Qadri *et al.* (2015), who studied the buoyancy-free lifted flame investigated earlier by Nichols & Schmid (2008) and Nichols *et al.* (2009) using a combination of DNS and local linear stability analysis. All of the previous linear global stability analyses of jet flows have considered buoyancy-free conditions. The method is to be employed below to examine buoyancy-induced flickering of axisymmetric laminar jet diffusion flames. The study provides the critical conditions at the onset of the linear global instability as well as the Strouhal number of the associated oscillations in terms of the governing parameters of the problem.

An important aspect of jet-flow instability concerns the applicability of spatio-temporal linear stability analyses for the predictions of the critical conditions at the onset of the global instability. When the flow is sufficiently slender, in that the resulting eigenmodes are much shorter than the jet development region, then the assumption of nearly parallel flow becomes accurate and the critical conditions can be identified from the analysis of the region where the flow is absolutely unstable, as shown by Lesshafft *et al.* (2007). This slenderness condition is satisfied in buoyancy-free jet flows, for which the eigenmodes scale with the jet radius, which is much smaller than the jet development length for the moderately large values of the Reynolds number that characterize the

onset of the instability. For instance, local linear stability analyses of light gaseous jets (Coenen *et al.*, 2008; Coenen & Sevilla, 2012) have shown to give predictions in agreement with those of DNS (Lesshafft & Huerre, 2007) and of global stability analyses (Lesshafft *et al.*, 2015; Coenen *et al.*, 2016). This is in contrast with the buoyancy-induced flickering flames investigated below, for which the eigenmodes will be seen to scale with the flame length, rather than with the jet radius. Under those conditions, the quasi-parallel assumption no longer holds and predictions based on the local linear stability analysis become necessarily inaccurate, with resulting critical Froude numbers at the onset of the instability that are off by a factor exceeding two, as shown below.

As observed clearly in flow visualizations of jet flames with nearly uniform exit velocity profiles (Chen *et al.*, 1988), the flickering mode, characterized by large toroidal vortices surrounding the flame, is accompanied by a Kelvin-Helmholtz instability of the shear layer surrounding the fuel jet leading to the formation of an inner train of small discrete vortices. To focus attention on the flickering phenomenon, our analysis will purposely preclude the emergence of these shear instabilities by considering only cases in which the fuel-feed velocity profile is parabolic, an appropriate boundary condition for sufficiently long fuel injectors. Also, unlike previous authors (See & Ihme, 2014), who used in their stability analysis a detailed flow field description including finite-rate chemistry and advanced molecular-transport models, we choose to employ instead a simplified flow model that retains all relevant aspects involved in the hydrodynamic instability leading to flame flicker while neglecting secondary effects that complicate unnecessarily the description, thereby facilitating both development of fundamental physical understanding and extraction of parametric dependences. For instance, since the variations of density and transport properties in combustion flows are mainly associated with the temperature changes induced by the chemical heat release, a constant average molecular weight will be employed when writing the equation of state and the different transport coefficients will be assumed to be independent of the composition, while their temperature dependence will be approximated by a power law. A Fickian description with unity Lewis numbers will be used for the diffusion velocity of the reactants. Furthermore, we shall consider nonpremixed jet-flame configurations in which the rates of the chemical reactions involved in the fuel-oxidation process are sufficiently fast for the burning rate to be diffusion controlled (Liñán *et al.*, 2015). Under these conditions, the resulting nonpremixed flame remains anchored in the vicinity of the injector rim and the interaction between the envelope of hot gases surrounding the jet flame and the gravitational acceleration leading to the onset of the flickering mode can be investigated by using the limit of infinitely fast reaction, with the composition and temperature described in terms of a single passive scalar, the so-called mixture-fraction variable. Consideration of finite-rate chemistry is necessary in stability analyses of lifted flames, such as that performed recently by Qadri *et al.* (2015).

The Chapter is structured as follows. The nondimensional equations and boundary conditions are presented in § 2.2, which is followed in § 1.3 by relevant numerical results, including sample spectra and transition diagrams in the controlling-parameter plane. Comparisons of the predictions of the global stability analysis with results of DNS of unsteady axisymmetric flows are presented in § 1.4. A local spatio-temporal stability analysis of the transverse profiles of the base flow is performed in § 1.5; the results are seen to significantly overpredict the critical Froude number, thereby underscoring the limited predicting capability of local analyses for buoyancy-induced flickering. Finally, concluding remarks will be offered in § 2.5.

1.2 Problem formulation

As indicated in figure 1.1, the configuration analyzed includes a vertical fuel jet discharging upwards through an injector of inner radius a into an infinite air atmosphere. The specific geometry investigated here involves a thin injector of thickness $e \ll a$. To minimize wake effects, the rim of the injector is knife-like sharpened as indicated in the inset of figure 1.1. For the numerical integrations shown below the injector wall thickness and the slenderness ratio of the wedge tip were selected to be $e/a = 10^{-3}$ and $d/e = 20$, respectively. Smaller values of e/a and larger values of d/e were used in sample integrations to ensure that the results were independent of these two geometric parameters, so that the solution given below is representative of infinitesimally thin injectors.

For generality, the analysis considers dilution of the fuel with an inert gas, with $Y_{\mathrm{F},0}$ denoting the fuel mass fraction in its feed stream, while $Y_{\mathrm{O}_2,\mathrm{A}} = 0.232$ is the oxygen mass fraction in air. In the description, focused on the fluid mechanical aspects of the flow, we adopt the one-step irreversible overall reaction $\mathrm{F} + s\,\mathrm{O}_2 \rightarrow (1+s)\,\mathrm{Products} + q$, according to which the unit mass of fuel reacts with a mass s of oxygen, releasing in the process an amount of energy q. The above representation of the underlying stoichiometry for the oxidation of the fuel embodies the two fundamental thermochemical parameters involved in nonpremixed combustion (Liñán *et al.*, 2015),

$$S = \frac{sY_{\mathrm{F},0}}{Y_{\mathrm{O}_2,A}} \quad \text{and} \quad \gamma = \frac{qY_{\mathrm{F},0}}{c_pT_0'(1+S)}, \tag{1.1}$$

the former representing the mass of air that one needs to mix with the unit mass of the gaseous fuel stream to generate a stoichiometric mixture and the latter being the corresponding dimensionless temperature increment resulting from the adiabatic combustion of that mixture. Here, T_0' is the initial temperature of the feed streams, assumed to be equal for the fuel jet and for the surrounding air atmosphere, and c_p represents the specific heat at constant pressure, taken to be constant in the following analysis. Typical values for undiluted hydrocarbon-air flames initially at normal ambient temperature are $S_u = s/Y_{\mathrm{O}_2,A} \simeq 15$ and $\gamma_u \simeq 6-7$. Diluting the fuel stream with an inert gas to

give a fuel mass fraction $Y_{\mathrm{F},0} < 1$ in its feed stream has a direct effect on the value of $S = Y_{\mathrm{F},0} S_u$, but a much more limited effect on the heat-release parameter, as can be seen by writing the second expression in (1.1) for $S_u \gg 1$ in the approximate form $(\gamma_u - \gamma)/\gamma_u \simeq (1 + Y_{\mathrm{F},0} S_u)^{-1}$, which indicates that significant variations of γ require extremely dilute fuel mixtures such that $Y_{\mathrm{F},0} \sim S_u^{-1}$.

In the limit of infinitely fast reaction adopted here the reaction takes place in an infinitesimally thin layer, outside of which the chemical-equilibrium condition $\hat{Y}_{\mathrm{F}} \hat{Y}_{\mathrm{O}_2} = 0$ applies, with $\hat{Y}_{\mathrm{F}} = Y_{\mathrm{F}}/Y_{\mathrm{F},0}$ and $\hat{Y}_{\mathrm{O}} = Y_{\mathrm{O}_2}/Y_{\mathrm{O}_2,A}$ representing the fuel and oxygen mass fractions normalized with their values in their respective feed streams. The reaction-rate terms in the conservation equations for energy and species appear as Dirac-delta distributions located at the flame, which becomes in this limit an infinitesimally thin surface attached to the injector separating a near-axis region without oxygen from a fuel-free outer atmosphere (Burke & Schumann, 1928). For equidiffusive reactants, Shvab (1948) and Zel'dovich (1949) showed how the computation can be facilitated by the introduction of conserved scalars satisfying transport equations, obtained by combinations of the species and energy conservation equations that eliminate the chemical-source terms. Two conveniently normalized forms of these passive scalars are the mixture fraction and the excess enthalpy, defined as

$$Z = \frac{S\hat{Y}_{\mathrm{F}} - \hat{Y}_{\mathrm{O}} + 1}{S + 1} \quad \text{and} \quad H = T - 1 + \gamma(\hat{Y}_{\mathrm{F}} + \hat{Y}_{\mathrm{O}} - 1), \tag{1.2}$$

where the nondimensional temperature T has been scaled with T_0'. The mixture fraction is defined to be zero in the air stream and unity in the fuel stream, respectively, whereas at the flame, where both reactants appear in zero concentrations, Z takes the stoichiometric value $Z_S = 1/(S + 1)$. On the other hand, the excess enthalpy is defined to be zero in both feed streams, so that when the injector walls are adiabatic, the case considered here, the solution for the associated transport equation reduces to $H = 0$ everywhere in the flow field, thereby facilitating the description. The piecewise-linear expressions

$$\hat{Y}_{\mathrm{F}} = 0, \quad \hat{Y}_{\mathrm{O}} = 1 - \frac{Z}{Z_S}, \quad T - 1 = \gamma \frac{Z}{Z_S}; \qquad \text{for } 0 \le Z \le Z_S, \tag{1.3a}$$

$$\hat{Y}_{\mathrm{O}} = 0, \quad \hat{Y}_{\mathrm{F}} = \frac{Z - Z_S}{1 - Z_S}, \quad T - 1 = \gamma \frac{1 - Z}{1 - Z_S}; \qquad \text{for } Z_S \le Z \le 1, \tag{1.3b}$$

obtained from the definitions (1.2) with use made of the equilibrium condition $\hat{Y}_{\mathrm{F}} \hat{Y}_{\mathrm{O}_2} = 0$ and of the result $H = 0$, provide the reactant mass fractions and temperature in terms of Z. Evaluation of the expressions for T at $Z = Z_S$ indicates that the temperature at the flame surface is everywhere equal to the stoichiometric adiabatic flame temperature $T = 1 + \gamma$, a known result of the infinitely fast reaction limit that holds in adiabatic configurations with unity Lewis numbers of the reactants.

The problem reduces to that of integrating the continuity and momentum equations to-

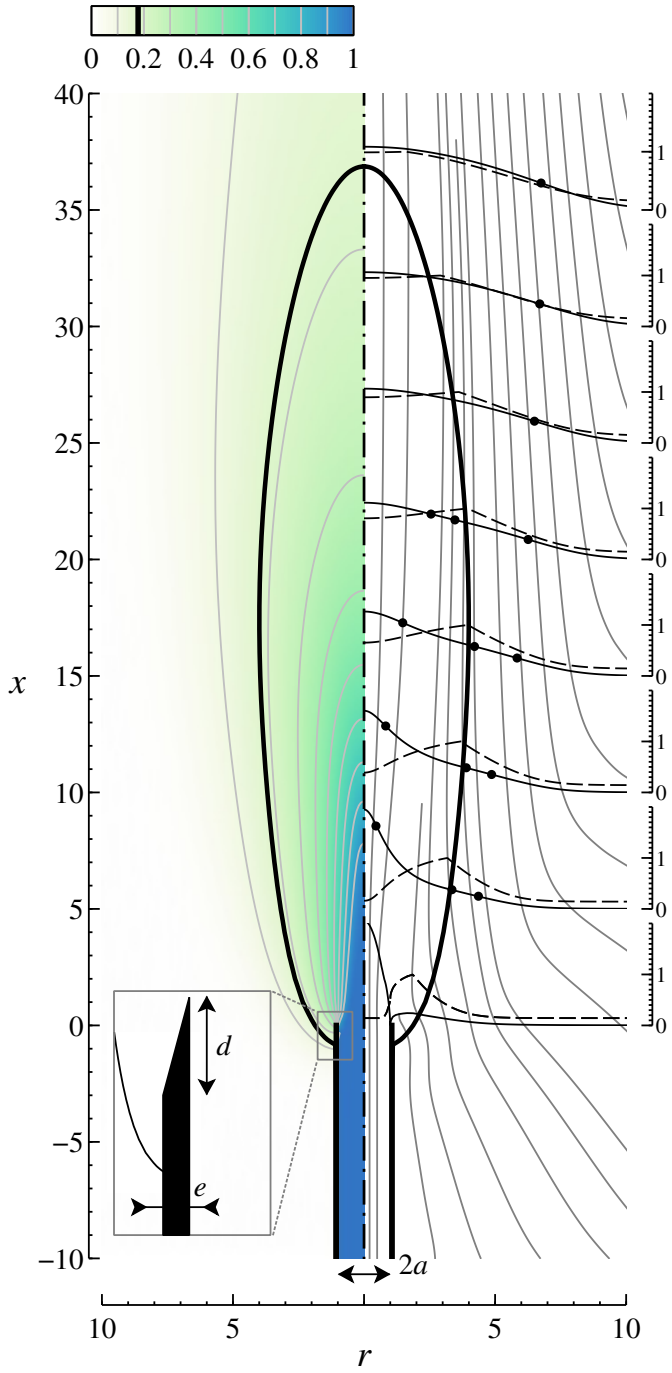

Figure 1.1: Base-flow isocontours of $\bar{Z}$ (left-hand side) and streamlines (right-hand side) together with radial profiles of $\bar{v}_x$ (solid curves) and $\bar{T}/(\gamma+1)$ (dashed curves) at $x = (0, 5, 10, 15, 20, 25, 30, 35)$ for $Pr = 0.7$, $S = 4.62$, $\gamma = 6$, $Re = 100$ and $Fr = 300$. The dot on the velocity profiles indicates the location of the inflection points. The thick solid line represents the stoichiometric flame surface $\bar{Z} = Z_S$, where $\bar{T} = 1 + \gamma$.

gether with the transport equation for Z, which are written in the dimensionless form

$$\frac{\partial \rho}{\partial t} + \nabla \cdot (\rho \boldsymbol{v}) = 0, \tag{1.4}$$

$$\rho \frac{\partial \boldsymbol{v}}{\partial t} + \rho \boldsymbol{v} \cdot \nabla \boldsymbol{v} = -\nabla p + \frac{1}{Re} \nabla \cdot \bar{\bar{\tau}} + \frac{1}{Fr}(1-\rho)\boldsymbol{e}_x, \tag{1.5}$$

$$\rho \frac{\partial Z}{\partial t} + \rho \boldsymbol{v} \cdot \nabla Z = \frac{1}{Re\, Pr} \nabla \cdot \left[\rho D_{\mathrm{T}} \nabla Z\right], \tag{1.6}$$

where $Pr = 0.7$ is the Prandtl number and

$$Re = \frac{\rho_0' U_0 a}{\mu_0'} \quad \text{and} \quad Fr = \frac{U_0^2}{ga} \tag{1.7}$$

are the Reynolds number and the Froude number for the jet flow, respectively, with ρ_0' and μ_0' representing the density and shear viscosity in the feed streams. The jet radius a and the average jet velocity $U_0 = \dot{m}/(\pi a^2 \rho_0')$ based on the fuel mass flow rate $\dot{m}$ are used to scale the problem. The development employs cylindrical coordinates $\boldsymbol{x} = (x, r)$ centered at the injector exit plane with an associated velocity vector $\boldsymbol{v} = (v_x, v_r)$; the streamwise coordinate x pointing against the gravity vector $\boldsymbol{g} = -g\boldsymbol{e}_x$.

In the low-Mach number approximation utilized here, the pressure variations can be neglected in the first approximation when writing the equation of state, which therefore reduces to $\rho T = 1$ when the additional assumption of constant molecular weight is adopted to achieve maximum simplification, with $\rho = \rho'/\rho_0'$ denoting the dimensionless density. Furthermore, in this low-Mach number limit, the viscous-stress term proportional to the second viscosity coefficient can be incorporated in the definition of the variable p that represents in (1.5) the pressure difference from the unperturbed ambient distribution. Correspondingly, the resulting viscous-stress tensor reduces to $\bar{\bar{\tau}} = \mu\left(\nabla \boldsymbol{v} + \nabla \boldsymbol{v}^{\mathrm{T}}\right)$, with both p and $\bar{\bar{\tau}}$ scaled with the characteristic value of the dynamic pressure $\rho_0' U_0^2$. The power-law expressions $\mu = \rho D_{\mathrm{T}} = T^{\sigma}$, with $\sigma = 0.7$, are employed for the temperature dependence of the shear viscosity μ and thermal diffusivity D_{T}, both scaled with their feed-stream values.

Equations (1.4)–(1.6) must be integrated with appropriate conditions on the boundaries of the computational domain, which includes an outer cylindrical boundary with radius $r_{\max} \gg 1$, with downstream and upstream boundaries located at $x = x_d$ and at $x = x_u$. The results corresponding to the most unstable mode were tested to be independent of the size of the computational domain, with the values $r_{\max} = 45$, $x_d = 450$, and $x_u = -10$ selected for the computations shown below. The injector is assumed to be sufficiently long for the fuel flow to be fully developed, thereby giving $\boldsymbol{v} = 2\,(1 - r^2)\boldsymbol{e}_x$ and $Z = 1$ in the fuel boundary upstream from the injector exit (i.e. at $x = x_u$ for $0 \le r \le 1$). On the injector walls the solution satisfies the nonslip condition $\boldsymbol{v} = 0$, together with the condition $\boldsymbol{n} \cdot \nabla Z = 0$ corresponding to an impermeable wall, with $\boldsymbol{n}$ representing here the

normal unit vector. To let the air enter or leave the computational domain as required to satisfy the development and the entrainment needs of the jet, a stress-free condition $-p\boldsymbol{n} + \bar{\bar{\tau}} \cdot \boldsymbol{n}/Re = 0$ is applied all around the outer air boundary. Air enters the flow field through the lateral boundary and through the upstream boundary, so that the condition $Z = 0$ applies there, whereas $\boldsymbol{n} \cdot \nabla Z = 0$ must be used on the downstream boundary to allow for the evacuation of the combustion products.

1.3 The global linear stability analysis

1.3.1 The eigenvalue problem

Introduction of the temporal normal-mode decomposition

$$(\boldsymbol{v}, p, Z) = (\bar{\boldsymbol{v}}, \bar{p}, \bar{Z}) + \varepsilon(\hat{\boldsymbol{v}}, \hat{p}, \hat{Z})e^{-\mathrm{i}\omega t}, \tag{1.8}$$

involving the steady base flow $(\bar{\boldsymbol{v}}, \bar{p}, \bar{Z})(\boldsymbol{x})$, the eigenfunctions $(\hat{\boldsymbol{v}},\ \hat{p}, \hat{Z})(\boldsymbol{x})$ multiplied by an arbitrarily small factor ε, and the complex angular frequency $\omega = \omega_r + \mathrm{i}\omega_i$, leads to a set of nonlinear equations for the base flow (i.e. the steady counterpart of (1.4)–(1.6)), to be integrated with the boundary conditions stated in the last paragraph of the preceding section. The associated linear equations for the perturbed flow

$$-\mathrm{i}\omega\hat{\rho} + \nabla \cdot \hat{\rho}\bar{\boldsymbol{v}} + \nabla \cdot \bar{\rho}\hat{\boldsymbol{v}} = 0, \tag{1.9}$$

$$\begin{aligned} -\mathrm{i}\omega\bar{\rho}\hat{\boldsymbol{v}} + \hat{\rho}\bar{\boldsymbol{v}} \cdot \nabla\bar{\boldsymbol{v}} + \bar{\rho}\hat{\boldsymbol{v}} \cdot \nabla\bar{\boldsymbol{v}} + \bar{\rho}\bar{\boldsymbol{v}} \cdot \nabla\hat{\boldsymbol{v}} = &- \nabla\hat{p} - \frac{1}{Fr}\hat{\rho}\boldsymbol{e}_x \\ &+ \frac{1}{Re}\nabla \cdot \left[\hat{\mu}(\nabla\bar{\boldsymbol{v}} + \nabla\bar{\boldsymbol{v}}^{\mathrm{T}}) + \bar{T}^{\sigma}\left(\nabla\hat{\boldsymbol{v}} + \nabla\hat{\boldsymbol{v}}^{\mathrm{T}}\right)\right], \end{aligned} \tag{1.10}$$

$$-\mathrm{i}\omega\bar{\rho}\hat{Z} + \hat{\rho}\bar{\boldsymbol{v}} \cdot \nabla\bar{Z} + \bar{\rho}\hat{\boldsymbol{v}} \cdot \nabla\bar{Z} + \bar{\rho}\bar{\boldsymbol{v}} \cdot \nabla\hat{Z} = \frac{1}{RePr}\nabla \cdot \left[(\hat{\mu}\nabla\bar{Z} + \bar{T}^{\sigma}\nabla\hat{Z})\right], \tag{1.11}$$

arise from linearization of (1.4)–(1.6); these must be supplemented with $\hat{\rho}/\bar{\rho} = -\hat{T}/\bar{T}$ and $\hat{\mu} = \sigma\bar{T}^{\sigma-1}\hat{T}$, which follow from the equation of state and from the transport description, and with $\hat{T} = \gamma\hat{Z}/Z_S$ for $0 \le \bar{Z} \le Z_S$ and $\hat{T} = -\gamma\hat{Z}/(1 - Z_S)$ for $Z_S \le \bar{Z} \le 1$, which follow from (1.3). Boundary conditions for (1.10)–(1.11) are $\hat{\boldsymbol{v}} = \hat{Z} = 0$ in the fuel stream and $\hat{\boldsymbol{v}} = \boldsymbol{n} \cdot \nabla\hat{Z} = 0$ on the injector wall. On the air boundary, the stress-free condition for the perturbed flow reduces to $-\hat{p}\boldsymbol{n} + (\nabla\hat{\boldsymbol{v}} + \nabla\hat{\boldsymbol{v}}^{\mathrm{T}}) \cdot \boldsymbol{n}/Re = 0$ on the upstream and lateral air boundaries, where $\hat{Z} = 0$, and to $\sigma\gamma\left[(\bar{p}/\bar{T})(\hat{Z}/Z_S) - \hat{p}\right]\boldsymbol{n} + \bar{T}^{\sigma}\left(\nabla\hat{\boldsymbol{v}} + \nabla\hat{\boldsymbol{v}}^{\mathrm{T}}\right) \cdot \boldsymbol{n}/Re = 0$ on the downstream boundary, where $\boldsymbol{n} \cdot \nabla\hat{Z} = 0$. Nontrivial solutions $(\hat{\boldsymbol{v}}, \hat{p}, \hat{Z}) \neq 0$ are found for a discrete set of values of ω, which is determined as an eigenvalue. The real part of ω is the frequency of the perturbation, defining a Strouhal number $St = \omega_r/\pi$ (the ratio of the residence time $2a/U_0$ to the period of the oscillation); the imaginary part is the growth rate, which dictates whether the flame is globally stable ($\omega_i < 0$) or unstable ($\omega_i > 0$).

1.3.2 Sample numerical results

The base flow was integrated using a finite-element method with $P1$ elements for the pressure field and $P2$ elements for the remaining variables, combined with a Newton-Raphson root-finding algorithm; details of the discretization method, used for instance by Garnaud *et al.* (2013*b*), can be found in Hecht (2012). The same finite-element formalism was employed to discretize the perturbed equations, resulting in a generalized eigenvalue problem that was solved using a shifted inverse power method (Lehoucq *et al.*, 1997).

The integrations explored in particular configurations with $2.08 \leq S \leq 9.66$ and moderately large values of Re, for which the resulting flame height is much larger than the injector radius, as shown in figure 1.1 for the case $S = 4.62$, $Re = 100$, and $Fr = 300$. A thick solid curve is used to denote the flame location, where $\bar{Z} = Z_S \simeq 0.178$ and $\bar{T}/(\gamma + 1) = 1$. Besides isocontours of $\bar{Z}$, the plot includes streamlines, which serve to illustrate the motion of the air induced by the entrainment of the mixing layer surrounding the flame envelope.

Radial profiles of axial velocity $\bar{v}_x$ and normalized temperature $\bar{T}/(\gamma + 1)$ are represented in figure 1.1 at different axial locations. Even for this relatively large Froude number, buoyancy is seen to accelerate the flow in the flame envelope, leading to the appearance of two inflection points in the velocity profile near the flame, additional to the inflection point associated with the shape of the initial velocity profile (the location of these inflection points is marked with a dot). As shown previously for mixing layers (Soteriou & Ghoniem, 1995) and low-density jets (Lesshafft & Huerre, 2007), the action of the baroclinic torque, induced in jet flames by the radial density gradient present in the near-flame region where the velocity profile displays inflection points, plays a key role in the development of a region of absolute stability (Lingens *et al.*, 1996*a*), which in turn triggers the global oscillations. The rate at which the induced perturbations are convected away from this wave-maker region depends on the local value of the axial velocity, with smaller velocities favouring the development of absolute instabilities (Lesshafft & Marquet, 2010).

Figure 1.2(a) shows the eigenvalue spectra computed for $Re = 100$ and different values of Fr. For all cases, the most unstable eigenmode is indicated with a bigger symbol in red. Decreasing the Froude number is seen to destabilize the flow, so that for $Fr = 300$ the growth rate ω_i of the most unstable mode is still negative, but it is already positive for $Fr = 250$. For completeness, eigenmodes corresponding to the subcritical case $Fr = 300$ are plotted in figure 1.2(b). As can be seen, both the radial extent of the eigenmodes and their wavelength scale with the flame dimensions. Although the length $x_d = 450$ of the computational domain was not long enough to capture the downstream decay of the eigenmodes, the associated values of ω for the most unstable mode were seen to be independent of x_d provided that $x_d > 400$, as verified in a series of computations.

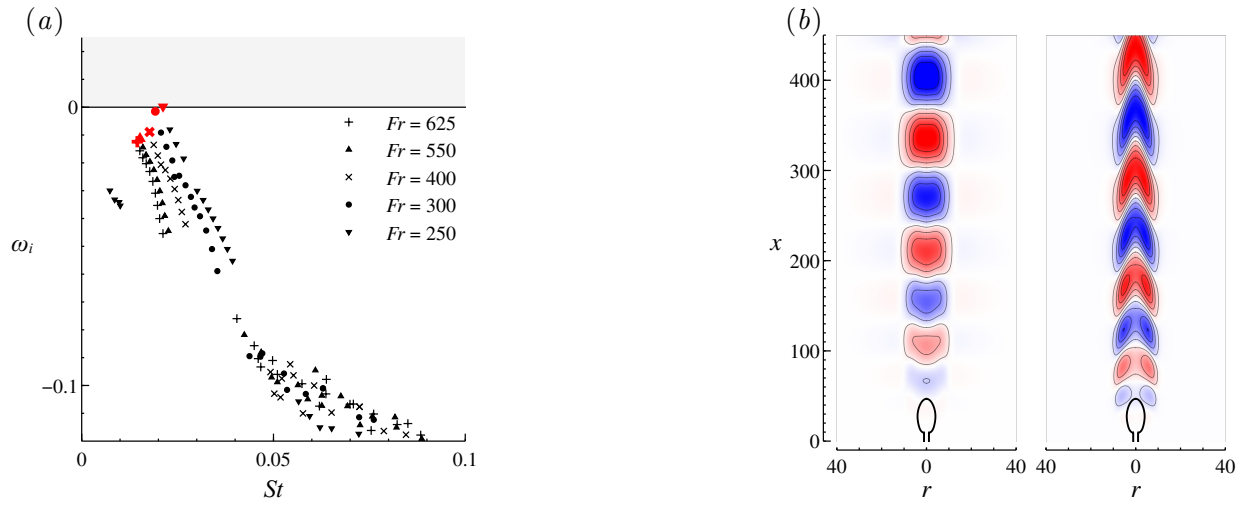

Figure 1.2: (a) Eigenvalue spectra for $Pr = 0.7$, $S = 4.62$, $\gamma = 6$, $Re = 100$, and $Fr = (250, 300, 400, 550, 625)$. (b) Real part of the streamwise velocity $\hat{v}_x$ (left) and mixture fraction $\hat{Z}$ (right) for the eigenfunctions of the most unstable mode with $Re = 100$ and $Fr = 300$.

1.3.3 Transition diagrams

Marginal conditions were determined by linear interpolation of the results of stability spectra computed for given values of S and Re and decreasing values of Fr (including stable and unstable cases), giving the transition diagrams and accompanying frequencies shown in figure 1.3. The resulting marginal curves serve to assess effects of fuel-feed dilution and of molecular transport. Increasing Re for a given value of S is seen to have a destabilizing effect, in that the global instability sets in at a higher value of Fr, in agreement with recent observations for low-density jets (Coenen *et al.*, 2016). Conversely, fuel-feed dilution (i.e. decreasing values of S) tends to stabilize the flow, a result that can be explained by noticing that dilute flames sit closer to the axis, where the downstream convective rate of the perturbations is higher, thereby hindering the development of a region of absolute instability and resulting in smaller critical values of Fr.

The large variations in critical values of Fr observed in figure 1.3 would be considerably reduced should the characteristic scales of the flame, rather than those associated with fuel injection, be used in defining the relevant Froude number (Liñán *et al.*, 2015). Thus, with $Re \gg 1$ and $S \gg 1$ the flame length is of order $SRea$. At these distances, the jet velocity has decreased to values of order U_0/S, which must be compared with the buoyancy-induced velocity $gSRea$, the square of their ratio giving $Fr/(S^3Re)$ as the relevant Froude number for jet flames. Inspection of the results in figure 1.3 reveals that this alternative definition would result in a transition diagram with less pronounced variations of the critical Froude number over the range of conditions explored.

For the range of Reynolds numbers explored in figure 1.3, the effective Froude number accounting for the residence time in the flame region $Fr/(S^3Re)$ is somewhat smaller than unity,

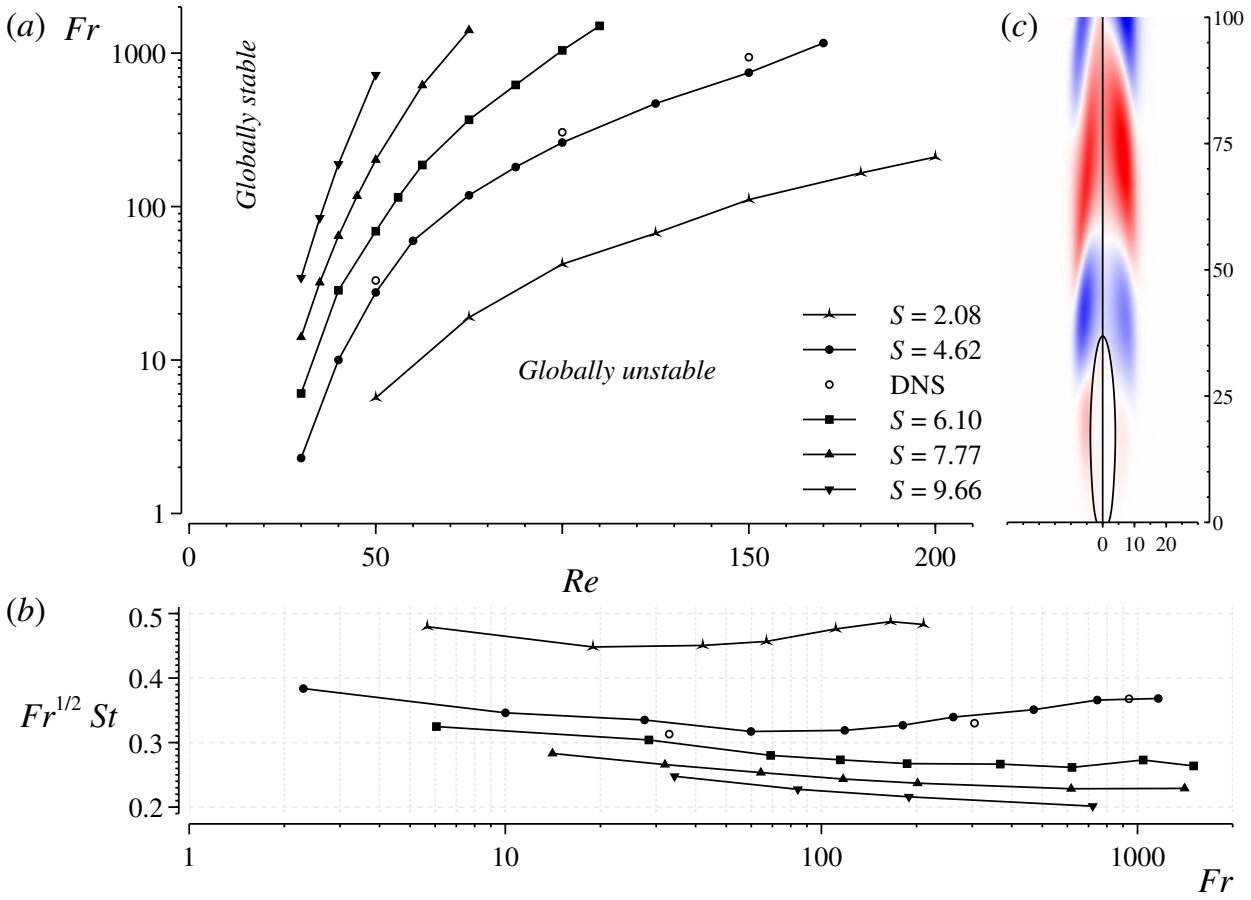

Figure 1.3: (a) Transition diagram in the $Re-Fr$ parametric plane for different values of S, with the (b) accompanying panel showing the variation with Fr of the nondimensional frequency $Fr^{1/2}St = (\omega_r/\pi)/\sqrt{g/a}$ at the margin of instability and the empty symbols in both plots representing DNS predictions for $Re = (50, 100, 150)$. As explained in the text, (c) a comparison for $S = 4.62$, $Re = 100$, and $Fr = 261.40$ of the eigenmode $\hat{T}(\boldsymbol{x})$ (right-hand side) with a snapshot extracted from the DNS results (left-hand side).

corresponding to jet flames with significant buoyancy effects. Consequently, the dynamics of the resulting oscillations at the margin of stability is characterized by the buoyancy time $\sqrt{a/g}$, rather than by the residence time a/U_0 employed initially in nondimensionalizing the problem. This scaling is tested in figure 1.3, where the frequency is represented in terms of $(\omega_r/\pi)/\sqrt{g/a} = Fr^{1/2}St$. As can be seen, for each value of S the resulting frequencies change only by about 10% over the whole range of Froude numbers explored in the figure, thereby demonstrating the prevalence of the buoyancy scaling. This is in agreement with the experimental observations of Durox & Villermaux (1997) and Sato *et al.* (2000), who found that $St \sim Fr^{-1/2}$.

The buoyancy-dominated flickering mode observed here is markedly different from that corresponding to buoyancy-free light jets and flames, for which the resulting frequencies scale with a/U_0, with associated eigenmodes scaling with the jet radius, rather than with the flame length.

This alternative buoyancy-free mode, which must become dominant at sufficiently high Froude numbers (and sufficiently high accompanying Reynolds numbers), was not observed in the computations carried out here. For the Poiseulle exit-velocity profile considered in our work, preliminary computations for $Fr = \infty$ and $S = 6.10$ indicated that nonbuoyant flames are globally stable up to the largest Reynolds number considered ($Re = 1000$). A critical Reynolds number exceeding 1000 for buoyancy-free jet flames is consistent with previous results concerning the influence of the exit velocity profile on the stability of light jets (Hallberg & Strykowski, 2006). Smaller critical values of the Reynolds number are expected, for instance, for nearly uniform profiles, encountered with shorter fuel injectors.

1.4 Comparison with DNS results

The predictions of the stability analysis at the margin of stability were compared with DNS results obtained with a time-dependent axisymmetric code (Carpio *et al.*, 2016) using the same grid employed in the global stability computations. The numerical simulations at three different points along the marginal curve for $S = 4.62$, namely, $(Re, Fr) = (50, 26.60)$, $(Re, Fr) = (100, 261.40)$, and $(Re, Fr) = (150, 745.64)$, yielded periodic solutions with small amplitude. The associated Strouhal numbers, $St = (0.0628, 0.0200, 0.0132)$, obtained by fitting the oscillations of the numerical solutions to a sinusoidal function, were seen to be in excellent agreement with the values $St = (0.0638, 0.0190, 0.0134)$ predicted by the stability analysis. The agreement extends to the morphology of the flickering mode, as can be seen in the inset of figure 1.3, which compares the eigenmode $\hat{T}(\boldsymbol{x})$ corresponding to $(Re, Fr) = (100, 261.40)$ with the near-critical DNS results, the latter obtained by subtracting the time-averaged temperature from the instantaneous distribution $T(\boldsymbol{x}; t^*)$, with the time t^* appropriately selected to minimize the observed differences. As can be seen, there exist excellent agreement not only in the predicted wavelength but also in the shape of the cells representing the traveling rollers.

As mentioned above, for the parametric values corresponding to the marginal conditions of the stability analysis, the DNS results were seen to exhibit small oscillations of nonnegligible amplitude. Additional computations for increasing values of Fr, resulting in periodic solutions with decreasing amplitude, were performed to determine the marginal curve predicted by the DNS results. The transition to the flickering state is governed by a supercritical Hopf bifurcation. Correspondingly, with the Froude number being the relevant bifurcation parameter for fixed values of S and Re, the amplitude of the oscillations near the margin of stability is expected to exhibit the proportionality $A^2 \sim (Fr - Fr^*)$ (Landau & Lifshitz, 1959, § 27), where Fr^* is the critical value of Fr. This is illustrated in figure 1.3(a), which shows the squared amplitude of the

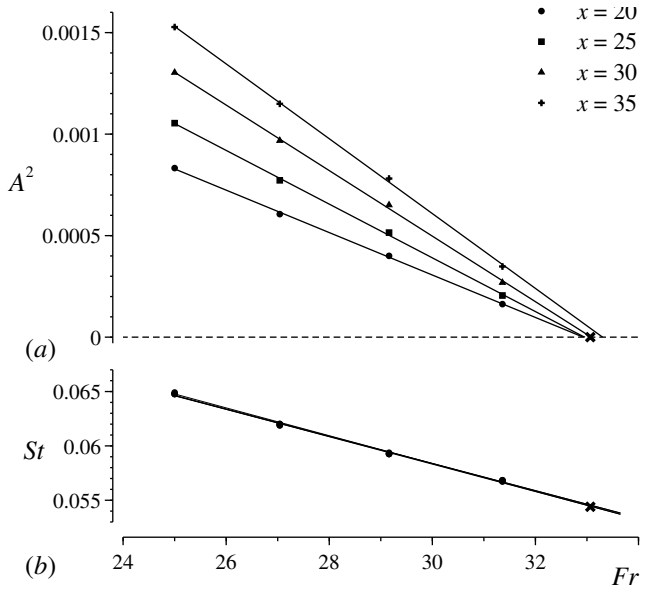

Figure 1.4: DNS computations of the (a) squared amplitude of oscillations, A^2, and (b) Strouhal numbers St, measured at different downstream axial locations, $x = 20, 25, 30$ and 35 for $Re = 50$ and $S = 4.62$. The solid lines in the upper part of the plot represent linear fits of the points (Fr, A^2) in order to determine the critical Froude number, Fr^*, for which the amplitude of the oscillations is zero. Upon extrapolation, a critical value $Fr^* = 33.065$ was found, with an associated Strouhal number $St^* = 0.0544$, marked with a cross, whereas the Strouhal number for the conditions predicted by the global stability analysis was found to be $St = 0.0628$.

mixture-fraction oscillations along the axis at four different downstream locations, as obtained in numerical simulations for $Re = 50$, $S = 4.62$, and decreasing values of Fr. Extrapolating the corresponding results to zero amplitude provides the critical value Fr^* of Fr, giving for instance $Fr^* = (33, 305, 940)$ for $Re = (50, 100, 150)$. These values are compared in figure 1.3 with the values $Fr^* = (26.60, 261.40, 745.64)$ corresponding to the linear stability analysis.

The direct numerical simulations also indicate that near the margin of stability there exists a linear dependence of the oscillation frequency on the Froude number. As shown in figure 1.3(b), the observed frequency is identical at all four locations—confirming the global nature of the flicker instability—with the critical value $St^* = 0.054$ approached as $Fr \to Fr^* \simeq 33$. This is to be compared with the value $St = 0.0628$ predicted by the global stability analysis at the corresponding critical Froude number $Fr = 26.60$. The differences observed, for both critical Froude numbers and associated frequencies, whose relative magnitude is on the order of 20% in the range of Reynolds numbers investigated, may be attributed to the fact that disturbances experience very large gains in slightly subcritical settings, leading to a substantial amplification of small numerical noise in the DNS integrations that results in the larger critical values of Fr shown in figure 1.3. Clearly, the origin of the observed discrepancies warrants further investigation in future work.

1.5 Comparison with a local stability analysis

As explained in Huerre & Monkewitz (1990), for slender flows there exists a close relationship between the evolution of the local stability characteristics at each streamwise position x, and the global instability properties of the flow. However, this relationship depends crucially on the requirement that the wavelength λ be much smaller than the typical evolution length scale L of the basic flow; and, quoting Huerre & Monkewitz (1990), "A breakdown of this assumption would preclude any possible connection between local and global instability properties". For the diffusion flame presented in figure 1.3, it can be seen that the wavelength λ of the global instability is comparable to the flame height, which characterizes the spatial evolution of the base flow. Therefore, the conditions needed for applicability of the local spatio-temporal analysis are not satisfied, which may result in significant inaccuracies in inferred predictions of global instability properties. This aspect of the problem is to be investigated here. Specifically, we shall study the downstream evolution of the local spatio-temporal stability properties of the base flow used earlier for the global stability analysis. We begin by formulating the local stability analysis, and then show results for the case $S = 6.1$ and $Re = 75$, with $Fr = 375$ and $Fr = 800$. In analyzing the results it is worth bearing in mind that the global instability analysis predicts a critical Froude number $Fr = 368$ for $S = 6.1$ and $Re = 75$, so that the flow should be globally stable under these conditions.

At each downstream position x, the basic flow is assumed to be locally parallel, with radial profiles of velocity $\bar{\boldsymbol{v}}(r) = (\bar{v}_x(r), 0)$ and mixture fraction $\bar{Z}(r)$; small perturbations are introduced as normal modes $[\hat{v}_x(r), \mathrm{i}\hat{v}_r(r), \hat{p}(r), \tilde{Z}(r)] \exp[\mathrm{i}(kx - \omega t)]$, with complex axial wavenumber $k = k_\mathrm{r} + \mathrm{i}k_\mathrm{i}$ and complex angular frequency $\omega = \omega_r + \mathrm{i}\omega_i$. Here k, ω, and t are nondimensionalized using a and U_0. In section 1.5.1 it is shown how substitution of the normal modes into the equations of motion (1.4)–(1.6), linearized around the steady base flow, yields the system of ordinary differential equations (1.12)–(1.15) that, together with the boundary conditions (1.22)–(1.23), provides a generalized eigenvalue problem. The local stability properties can be obtained by solving the latter, whereby eigenfunctions $\hat{v}_x(r)$, $\hat{v}_r(r)$, $\hat{p}(r)$, $\tilde{Z}(r)$ only exist if k and ω satisfy a dispersion relation $D(k, \omega; Re, Fr, S, \gamma, \ldots, \bar{v}_x, \bar{v}_r, \bar{p}, \bar{Z}) = 0$. In the present section we are concerned with the absolute or convective character of the instability. Therefore we need to find the spatio-temporal instability modes with zero group velocity, i.e. modes for which $\mathrm{d}\omega/\mathrm{d}k = 0$. The growth rate $\omega_{0,\mathrm{i}}$ of these is called the absolute growth rate and determines whether the instability is convective, $\omega_{0,\mathrm{i}} < 0$, or absolute, $\omega_{0,\mathrm{i}} > 0$. The condition $\mathrm{d}\omega/\mathrm{d}k = 0$ is equivalent to the existence of a double root, or saddle point, in the complex k-plane, $\partial D/\partial k|_{k=k_0} = 0$. Among all the saddle points that may exist, only the one with the largest value of $\omega_{0,\mathrm{i}}$, while satisfying the Briggs–Bers criterion, determines the large-time impulse response of the flow (see, for instance, Huerre, 2000, and references therein).

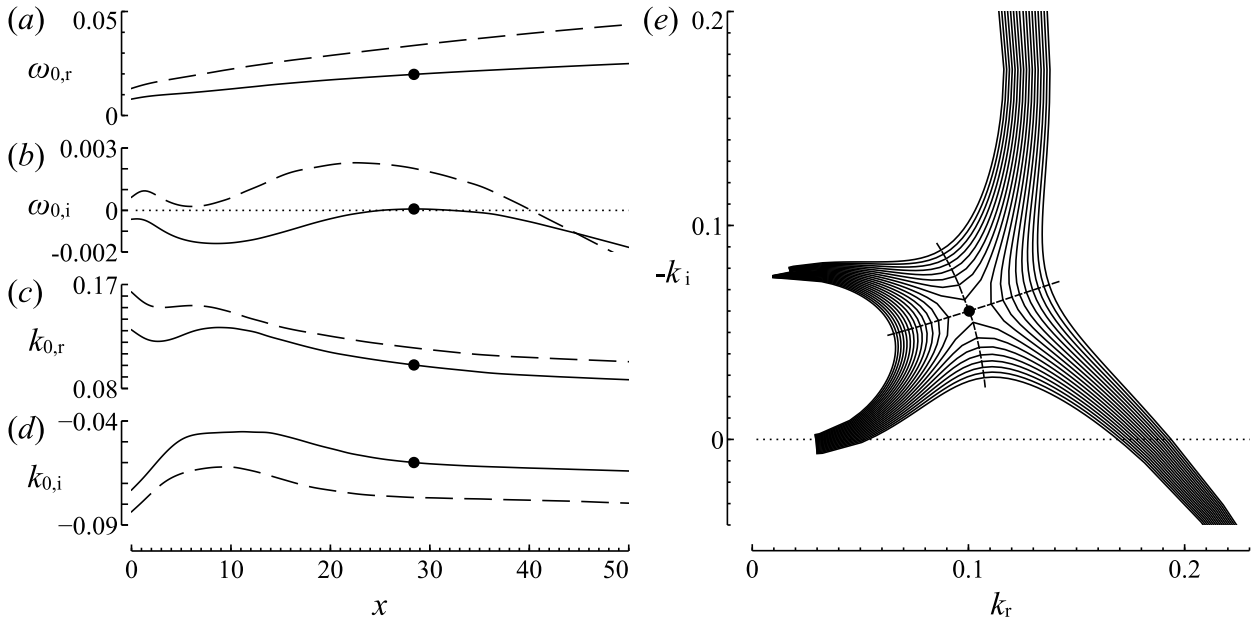

Figure 1.5: (a)–(d) Downstream evolution of the local spatio-temporal stability properties for $S = 6.1$ and $Re = 75$, with $Fr = 800$ (solid line) and $Fr = 375$ (dashed line). (e) Location of the saddle point (ω_0, k_0) in the complex k-plane at the downstream position $x = 28.4$, as indicated in figures (a)–(d) by the dots; the solid lines are spatial branches with a constant value of ω_i; the dashed lines are lines of constant $\omega_r = \omega_{0,\mathrm{r}}$.

Somme remarks on the numerical method used to determine (ω_0, k_0) are given in section 1.5.2.

Figures 1.5(a)–(d) show the downstream evolution of the spatio-temporal stability properties for the case $S = 6.1$ and $Re = 75$, with two values of the Froude number: $Fr = 800$ (solid lines), and $Fr = 375$ (dashed lines). The location of the saddle point $k = k_0$ in the complex k-plane is shown in figure 1.5(e), where the solid lines indicate spatial branches of constant ω_i, and the dashed lines have a constant value of $\omega_i = \omega_{0,\mathrm{i}}$. It can be seen how for $Fr \lesssim 800$ a pocket of absolute instability emerges around $x = 28$, with absolute frequency $\omega_{0,\mathrm{r}} = 0.02$ ($St = 0.006$) and wavelength $\lambda_0 = 2\pi/k_{0,\mathrm{r}} = 63$. In numerical simulations of weakly nonparallel heated jets, the appearance of such a pocket of absolute instability was shown to destabilize the nonlinear global mode responsible for the self-excited behaviour (Lesshafft *et al.*, 2007). Moreover, at criticality, the corresponding global frequency was found to coincide with the value given by the local stability analysis at the downstream position where the character of the instability changes from convective to absolute, in agreement with the theory developed by Pier *et al.* (1998) for weakly nonparallel flows.

The spatio-temporal stability analysis therefore predicts the flow to be globally unstable for $Fr \lesssim 800$, with a frequency at the margin of instability such that $St = 0.006$. These predictions differ significantly from those of the global stability analysis, which gives a critical Froude number

$Fr = 368$ with an associated Strouhal number $St \simeq 0.014$. These departures can be attributed to the failure of the condition $\lambda \ll L$ needed for applicability of the quasi-parallel analysis. Similar overpredictions in the growth rate of the perturbations have been reported in previous comparative studies of local/global stability analyses for wakes (Juniper *et al.*, 2011).

A pocket of absolutely unstable flow, away from boundaries, was also found by Qadri *et al.* (2015) in the context of nonbuoyant flames for their "mode B". As in the present work, they found this region of local absolute instability to lie at the basis of the excitation of a global low-frequency flickering mode. In the buoyancy-free configuration analyzed by Qadri *et al.* (2015) the density of the fuel jet upstream from the lifted flame is significantly lower than that of the surrounding atmosphere, causing a second instability mode ("mode A") to be present in their analysis, with a region of absolute instability that starts at the outlet of the jet, similar to that found by Coenen & Sevilla (2012) in the context of light jets.

1.5.1 The local stability equations

To obtain the stability equations, the normal modes

$$\{\hat{v}_x(r), \mathrm{i}\hat{v}_r(r), \hat{p}(r)\tilde{Z}(r)\} \exp[\mathrm{i}(kx - \omega t)]$$

are substituted into the equations of motion (1.4)–(1.6), linearized around the base flow $\{\bar{v}_x(r)$, $\bar{v}_r(r)$, $\bar{p}(r)$, $\bar{Z}(r)\}$, yielding the system of ordinary differential equations

$$-\omega\tilde{\rho} + k\bar{\rho}\hat{v}_x + \bar{\rho}(\hat{v}_r' + \hat{v}_r/r) + \bar{\rho}'\hat{v}_r + k\bar{v}_x\tilde{\rho} = 0, \tag{1.12}$$

$$\begin{aligned}\mathrm{i}\bar{\rho}\left(-\omega\hat{v}_x + k\bar{v}_x\hat{v}_x + \bar{v}_x'\hat{v}_r\right) &= -\mathrm{i}k\hat{p} - Fr^{-1}\tilde{\rho} \\ &+ Re^{-1}\left[\bar{\mu}(\hat{v}_x'' + \hat{v}_x'/r - k^2\hat{v}_x) + \bar{\mu}'(\hat{v}_x' - k\hat{v}_r) + (\bar{v}_x'' + \bar{v}_x'/r)\tilde{\mu} + \bar{v}_x'\tilde{\mu}'\right],\end{aligned} \tag{1.13}$$

$$\begin{aligned}\mathrm{i}\bar{\rho}\left(-\omega\hat{v}_r + k\bar{v}_x\hat{v}_r\right) &= \mathrm{i}\hat{p}' \\ &+ Re^{-1}\left[\bar{\mu}(\hat{v}_r'' + \hat{v}_r'/r - \hat{v}_r/r^2 - k^2\hat{v}_r) + \bar{\mu}'(\hat{v}_r' - \hat{v}_r/r - k\hat{v}_x) + k\bar{v}_x'\tilde{\mu}\right],\end{aligned} \tag{1.14}$$

$$\begin{aligned}\mathrm{i}\bar{\rho}\left(-\omega\tilde{Z} + k\bar{v}_x\tilde{Z} + \bar{Z}'\hat{v}_r\right) &= \\ &+ (Re\,Pr)^{-1}\left[\bar{\mu}(\tilde{Z}'' + \tilde{Z}'/r - k^2\tilde{Z}) + \bar{\mu}'\tilde{Z}' + (\bar{Z}'' + \bar{Z}'/r)\tilde{\mu} + \bar{Z}'\tilde{\mu}'\right],\end{aligned} \tag{1.15}$$

where the prime indicates differentiation with respect to r. Note that

$$\bar{T} = \begin{cases} 1 + \gamma\bar{Z}/Z_\mathrm{S} & \text{for } 0 \le \bar{Z} \le Z_\mathrm{S}, \\ 1 + \gamma(1-\bar{Z})/(1-Z_\mathrm{S}) & \text{for } Z_\mathrm{S} \le \bar{Z} \le 1, \end{cases} \tag{1.16}$$

$$\bar{\rho} = \bar{T}^{-1}, \tag{1.17}$$

$$\bar{\mu} = \bar{T}^{\sigma}, \tag{1.18}$$

and

$$\tilde{T} = \begin{cases} \gamma\tilde{Z}/Z_{\mathrm{S}} & \text{for } 0 \leq \bar{Z} \leq Z_{\mathrm{S}}, \\ -\gamma\tilde{Z}/(1-Z_{\mathrm{S}}) & \text{for } Z_{\mathrm{S}} \leq \bar{Z} \leq 1, \end{cases} \tag{1.19}$$

$$\tilde{\rho} = -\bar{T}^{-2}\tilde{T}, \tag{1.20}$$

$$\tilde{\mu} = \sigma\bar{T}^{\sigma-1}\tilde{T}. \tag{1.21}$$

The stability equations are accompanied by suitable boundary conditions. In the far field, all perturbations must vanish,

$$(\tilde{Z}, \hat{v}_x, \hat{v}_r, \hat{p}) \to 0 \text{ as } r \to \infty, \tag{1.22}$$

whereas at the centerline, a vanishing azimuthal dependence of the perturbations as $r \to 0$ may be imposed (Batchelor & Gill, 1962), leading to

$$\hat{v}_r = \hat{v}_x' = 0 \text{ and } (\tilde{Z}, \hat{v}_x, \hat{p}) \text{ finite at } r = 0. \tag{1.23}$$

Note that a Taylor expansion of (1.13)–(1.15) around the centerline yields

$$\bar{\mu}\hat{v}_x' + \tilde{\mu}\bar{v}_x' = 0, \tag{1.24}$$

$$Re^{-1}k(\bar{\mu}\hat{v}_x' + \bar{\mu}'\hat{v}_x) - 3Re^{-1}\bar{\mu}\hat{v}_r''/2 - \mathrm{i}\hat{p}' = 0, \tag{1.25}$$

$$\bar{Z}'\tilde{\mu} + \bar{\mu}\tilde{Z}' = 0. \tag{1.26}$$

1.5.2 Numerical method

The numerical method that is employed to obtain the saddle point (ω_0, k_0) is identical to that of Coenen & Sevilla (2012). A quadratic Taylor expansion of $\omega(k)$ around (ω_0, k_0) permits the employment of a Newton-Raphson root-finding algorithm, whereby at each iteration the temporal eigenvalue problem must be solved (Deissler, 1987). To that end, a spectral collocation method is used with a function $\xi = [r_{\mathrm{c}} - r(1 + 2r_{\mathrm{c}}/r_{\max})]/(r_{\mathrm{c}} + r)$ that maps the N collocation points from the Chebyshev interval $-1 \leq \xi \leq 1$ to the physical domain $0 \leq r \leq r_{\max}$ (Khorrami *et al.*, 1989). Values $r_{\mathrm{c}} = 3$, $r_{\max} = 50000$ and $N = 300$ are found to be adequate. For more details on the numerical method, we refer to Coenen & Sevilla (2012, Appendix B).

1.6 Concluding remarks

The present investigation has employed, for the first time, a global stability analysis to study the buoyancy-induced flickering of jet diffusion flames as a hydrodynamic global mode. It also provides the parametric dependence of the critical conditions at the onset of instability as

well as the morphology and frequency of the resulting oscillatory modes, giving predictions in fair agreement with results of direct numerical integrations.

While the simplified model employed here contains the fundamental underlying physics involved in the flickering phenomenon, additional effects should be investigated in future work. For instance, influences of shapes of jet-velocity profiles, including interactions of the different instabilities observed previously (Chen *et al.*, 1988), could be investigated by incorporating the boundary-layer thickness as an additional parameter, as done in previous spatio-temporal stability analyses of light jets (Coenen *et al.*, 2008). Preferential diffusion effects, associated with light and heavy fuel molecules, could be addressed in the infinitely fast reaction limit by using coupling-function formulations accounting for reactant Lewis numbers that differ from unity (Liñán, 1991). Consideration of finite-rate effects would be needed to examine the stability characteristics of lifted flames, studied in previous work (Qadri *et al.*, 2015) under buoyancy-free conditions. While the present work pertains to laminar flames, the global instability analysis could also be applied to turbulent conditions, with the steady base flow obtained for instance by time averaging results of large-eddy simulations, as done earlier in connection with local spatiotemporal analyses of jet flames (See & Ihme, 2014).

While the mode identified here is buoyancy-dominated, resulting in frequencies that scale with $(g/a)^{1/2}$, the dynamics at sufficiently large Froude numbers is expected to be controlled by a different mode, with frequencies that scale with U_0/a, similar to those observed in light jets (Hallberg & Strykowski, 2006). Our preliminary computations indicate that the investigation of the transition between the buoyancy-dominated and the momentum-dominated instabilities will require consideration of much higher Froude numbers, with associated critical Reynolds numbers exceeding $Re = 1000$. The associated global instability computation is expected to experience difficulties associated with the existence of resonance modes caused by spurious feedback from the outflow boundary, encountered earlier in the analysis of jets (Garnaud *et al.*, 2013*a*).

Our analysis indicates that the streamwise wavelength of the dominant instability mode scales with the flame height. Correspondingly, the assumption of quasi-parallel flow, necessary to ensure the predictive capability of local stability analyses, does not hold in buoyant jet diffusion flames, resulting in associated predictions of critical Froude numbers at the margin of instability that are off by a factor exceeding two. This finding further underscores the utility of global instability analysis for investigation of buoyancy-induced flickering instabilities.

This Chapter, in part, has been published in the *Journal of Fluid Mechanics*, "Diffusion-flame flickering as a hydrodynamic global mode", by D. Moreno-Boza, W. Coenen, A. Sevilla, J. Carpio, A. L. Sánchez and A. Liñán (2016) **798**, 997-1014. The dissertation author is the primary investigator in this publication.

Bibliography

Batchelor, G. & Gill, A. E. 1962 Analysis of the stability of axisymmetric jets. *J. Fluid Mech.* **14**, 529–551.

Boulanger, J. 2010 Laminar round jet diffusion flame buoyant instabilities: Study on the disappearance of varicose structures at ultra-low froude number. *Combust. Flame* **157**, 757–768.

Buckmaster, J. & Peters, N. 1986 The infinite candle and its stability—a paradigm for flickering diffusion flames. *Proc. Combust. Inst.* **21**, 1829–1836.

Burke, S. P. & Schumann, T. E. W. 1928 Diffusion flames. *Ind. Eng. Chem.* **20**, 998–1004.

Carpio, J., Prieto, J.L. & M., Vera 2016 Local anisotropic adaptive algorithm for the solution of low-mach transient combustion problems. *J. Comput. Phys.* **306**, 19–42.

Cetegen, B. M. & Dong, Y. 2000 Experiments on the instability modes of buoyant diffusion flames and effects of ambient atmosphere on the instabilities. *Exp. Fluids* **28**, 546–558.

Chamberlin, D. S. & Rose, A. 1948 The flicker of luminous flames. *Proc. Combust. Inst.* **1–2**, 27–32.

Chen, L.D., Seaba, J.P., Roquemore, W.M. & Goss, L.P. 1988 Buoyant diffusion flames. *Proc. Combust. Inst.* **22**, 677–684.

Coenen, W., Lesshafft, L., Garnaud, X. & Sevilla, A. 2016 Global instability in low-density jets: physical eigenmodes and spurious feedback effects. *J. Fluid Mech.* p. submitted.

Coenen, W. & Sevilla, A. 2012 The structure of the absolute unstable regions in the near field of low-density jets. *J. Fluid Mech.* **713**, 123–149.

Coenen, W., Sevilla, A. & Sánchez, A.L. 2008 Absolute instability of light jets emerging from circular injector tubes. *Phys. Fluids* **20**, 074104.

Deissler, R. J. 1987 The convective nature of instability in plane poiseuille flow. *Phys. Fluids* **30**, 2303–2305.

Durox, D., Yuan T. & Villermaux, E. 1997 The effect of buoyancy on flickering in diffusion flames. *Combust. Sci. and Tech.* **124**, 277–294.

Garnaud, X., Lesshafft, L., Schmid, P.J. & Huerre, P. 2013*a* Modal and transient dynamics of jet flows. *Phys. Fluids* **25**, 044103.

Garnaud, X., Lesshafft, L., Schmid, P.J. & Huerre, P. 2013*b* The preferred mode of incompressible jets: linear frequency response analysis. *J. Fluid Mech.* **716**, 189–202.

Hallberg, M. P. & Strykowski, P. J. 2006 On the universality of global modes in low-density axisymmetric jets. *J. Fluid Mech.* **569**, 493–507.

Hecht, F. 2012 New development in FreeFem++. *J. Numer. Math.* **20** (3-4), 251–265.

Huerre, P. 2000 Open shear flow instabilities. In *Perspectives in fluid dynamics* (ed. G. Batchelor, K. Moffatt & G. Worster), pp. 159–229. Cambridge.

Huerre, P. & Monkewitz, P. A. 1990 Local and global instabilities in spatially developing flows. *Annu. Rev. Fluid Mech.* **22**, 473–537.

Jiang, X. & Luo, K. H. 2000 Combustion-induced buoyancy effects of an axisymmetric reactive plume. *Proc. Combust. Inst.* **28**, 1989–1995.

Juniper, M. P., Li, L. K. B. & Nichols, J. W. 2009 Forcing of self-excited round jet diffusion flame. *Proc. Combust. Inst.* **32**, 1191–1198.

Juniper, M. P., Tammisola, O. & Lundell, F. 2011 The local and global stability of confined planar wakes at intermediate reynolds number. *J. Fluid Mech.* **686**, 218–238.

Khorrami, M. R., Malik, M. R. & Ash, R. L. 1989 Application of spectral collocation techniques to the stability of swirling flows. *J. Comp. Phys.* **81**, 206–229.

Landau, L.D. & Lifshitz, E.M. 1959 *Fluid Mechanics*, 3rd edn. Pergamon Press.

Lehoucq, R.B., Sorensen, D.C. & Yang, C. 1997 Arpack users guide: Solution of large scale eigenvalue problems by implicitly restarted arnoldi methods.

Lesshafft, L., Coenen, W., Garnaud, X. & Sevilla, A. 2015 Modal instability analysis of light jets. In *Procedia IUTAM*, , vol. 14, pp. 137–140.

Lesshafft, L. & Huerre, P. 2007 Linear impulse response in hot round jets. *Phys. Fluids* **19**, 024102.

Lesshafft, L., Huerre, P. & Sagaut, P. 2007 Frequency selection in globally unstable round jets. *Phys. Fluids* **19** (5), 054108.

Lesshafft, L. & Marquet, O. 2010 Optimal velocity and density profiles for the onset of absolute instability in jets. *J. Fluid Mech.* **662**, 398–408.

Liñán, A. 1991 The structure of diffusion flames. In *Fluid Dynamical Aspects of Combustion Theory* (ed. M. Onofri & A. Tesev), pp. 11–29. Harlow, UK. Longman Sci. Tech.

Liñán, A., Vera, M. & Sánchez, A.L. 2015 Ignition, liftoff, and extinction of gaseous diffusion flames. *Annu. Rev. Fluid. Mech.* **47**, 293–314.

Lingens, A., Neemann, K., Meyer, J. & Schreiber, M. 1996*a* Instability of diffusion flames. *Proc. Combust. Inst.* **26**, 1053–1061.

Lingens, A., Reeker, M. & Schreiber, M. 1996*b* Instability of buoyant diffusion flames. *Exp. Fluids* **20**, 241–248.

Mahalingam, S., Cantwell, B.J., & Ferziger, J.H. 1991 Stability of low-speed reacting flows. *Phys. Fluids A* **3**, 1533–1543.

Maxworthy, T. 1999 The flickering candle: transition to a global oscillation in a thermal plume. *J. Fluid Mech.* **390**, 297–323.

Nichols, J., Chomaz, J.-M. & Schmid, P. J. 2009 Twisted absolute instability in lifted flames. *Phys. Fluids* **21**, 015110.

Nichols, J. R. & Lele, S. K. 2011 Global modes and transient response of a cold supersonic jet. *J. Fluid Mech.* **669**, 225–241.

Nichols, J. W. & Schmid, P. J. 2008 The effect of a lifted flame on the stability of round fuel jets. *J. Fluid Mech.* **609**, 275–284.

Pier, B., Huerre, P. & Chomaz, J.-M. 1998 Steep nonlinear global modes in spatially developing media. *Phys. Fluids* **10**, 2433–2435.

Qadri, U.A., Chandler, G.J. & Juniper, M.P. 2015 Self-sustained hydrodynamic oscillations in lifted jet diffusion flames: origin and control. *J. Fluid Mech.* **775**, 201–222.

Sato, H., Amagai, K. & Arai, M. 2000 Flickering frequencies of diffusion flames observed under various gravity fields. *Proc. Comb. Inst.* **28**, 1981–1987.

See, Y.C. & Ihme, M. 2014 Effects of finite–rate chemistry and detailed transport on the instability of jet diffusion flames. *J. Fluid Mech.* **745**, 647–681.

Shvab, V.A. 1948 The relationship between the temperature and velocity fields in a gaseous flame. In *Research on Combustion Processes in Natural Fuel* (ed. G.F. Knorre), pp. 231–248. Moscow: Gosenergoizdat.

Soteriou, M. C. & Ghoniem, A. F. 1995 Effects of the free–stream density ratio on free and forced spatially developing shear layers. *Phys. Fluids* **7**, 2036.

Zel'dovich, Y.B. 1949 Teorii gorenia neperemeshannykh gazov. *Z. Tekh. Fiz.* **19**, 1199–1210.

Chapter 2

The onset of puffing of pool fires

Pool fires are known to undergo a bifurcation to a globally unstable puffing state caused by baroclinic and buoyant vorticity production. Although the supercritical puffing regime has been studied extensively in the literature, no detailed account has been given of the critical conditions for its onset, that being the purpose of the present chapter. For the relevant canonical case of round liquid pools, apart from the inherent thermochemical parameters, pool-fire puffing is governed by a single dimensionless number, the Rayleigh number, which scales with the cube of the pool diameter. Consequently, for a fixed fuel and under fixed ambient conditions, there is a critical fuel pool diameter, associated with a critical Rayleigh number, above which the fire starts puffing. This chapter provides a detailed analysis of the onset of pool-fire puffing, using both a global linear stability analysis that accounts for the axisymmetry of the instability, and laboratory experiments. The former is facilitated by a mathematical formulation of the dynamics of small laminar pool fires that takes advantage of the simplifications associated with the limit of infinitely fast reaction Liñán *et al.* (2015), but accounts for the nonunity Lewis number and vaporization characteristics of typical liquid hydrocarbon fuels.

2.1 Introduction

Pool fires are known to exhibit a self-sustained oscillatory behavior, shedding large toroidal coherent structures at a well established frequency, a phenomenon referred to in the literature as "puffing". This behavior influences the rate of air entrainment, soot production, the radiated heat output Smyth *et al.* (1993), and also the spreading of the flame Sibulkin & Hansen (1975); Finney *et al.* (2015). Pool-fire puffing has been studied extensively in the literature, by means of experiments Blinov & Khudyakov (1961); Sibulkin & Hansen (1975); Hertzberg *et al.* (1978); Zukoski *et al.* (1984); Schönbucher *et al.* (1985); Weckman & Sobiesiak (1988); Hamins *et al.*

(1992); Cetegen & Ahmed (1993); Yuan *et al.* (1994); Malalasekera *et al.* (1996); Most *et al.* (1996), numerical simulations Ghoniem *et al.* (1996); Mell *et al.* (1996); Tieszen *et al.* (1996); Prasad *et al.* (1999); Sinai (2000); Ma & Quintiere (2003); Chatterjee *et al.* (2015), and scale modeling Byram & Nelson (1970); Emori & Saito (1983); Pagni (1990); Delichatsios (1996). Extensive reviews on pool fires can be found in Emmons (1980); Heskestad (1998); Joulain (1998); Tieszen (2001). It is well established that under normal conditions of temperature and pressure typical hydrocarbon fuel pools of a few centimeters in diameter puff with a frequency on the order of 10 Hz, and that this frequency decays with the square root of the pool radius a^* as $f^* \sim \sqrt{g^*/a^*}$, as is readily obtained from a balance between the unsteady, convective and buoyancy terms in the Navier–Stokes equations. Viscous effects may enter as a stabilizing mechanism for small-scale pool fires, but these have been given little attention in the literature. More importantly, no detailed account has been given of the critical conditions for the *onset* of puffing.

For the physically similar problem of flickering jet diffusion flames, the authors have recently shown that it corresponds to a hydrodynamic global instability of the flow, the onset of which can successfully be predicted with a global stability analysis Moreno-Boza *et al.* (2016). Such an analysis takes into account the axisymmetric two-dimensional nonparallel character of the flow, the spatial structure of the instability being comparable in length to the flame itself. Since pool fires are typically even less slender than jet diffusion flames, and since the physical mechanisms producing vorticity—hence instability—in both flows are identical, it can be anticipated that the formalism will also yield satisfying results for the onset of pool-fire puffing. In a jet diffusion flame, momentum is injected with the fuel, and consequently the jet Reynolds number plays a role in the flame dynamics, along with the Froude number. In a pool fire however, the momentum that is transferred to the flow by the evaporation of fuel is negligible. Therefore, apart from the inherent thermochemical parameters, a single dimensionless parameter, expressed as a Rayleigh number $Ra = g^* {a^*}^3/(\nu_{\mathrm{A}}^* D_{\mathrm{T,A}}^*)$, characterizes the flow. Here a^* is the radius of the fuel pool, ν_{A}^* and $D_{\mathrm{T,A}}^*$ are the kinematic viscosity and thermal diffusivity of the ambient air, and g^* is the gravitational acceleration. Puffing occurs when the Rayleigh number exceeds a critical value. Note that for given burning conditions the latter is directly equivalent to a critical pool diameter.

The objective of the present work is to determine the critical Rayleigh number for pool-fire puffing, using the simplest possible description that still retains the essential physical ingredients. In particular, we employ the limit of infinitely fast chemical reaction, but account for the nonunity Lewis number and vaporization characteristics of typical liquid hydrocarbon fuels. It is known that radiation can play an important role in luminous sooting flames, lowering the peak temperature, and increasing the heat transfer to the liquid fuel Hertzberg *et al.* (1978); Sher (1982); Akita & Yumoto (1965). Nevertheless, because it is a volumetric effect, it is expected to be small for the

flame sizes associated with the onset of puffing, which, as our analysis will reveal, are on the order of a centimeter. Details of the specific design of the burner, such as the pan lip height, the thermal properties of the pan and its surrounding wall, and the height of the fuel level with respect to the pan rim, can also have a considerable influence on small-scale pool fires Emmons (1961). In our analysis, to eliminate the need for solving the complete coupled heat transfer problem for the solid elements, we purposely focus on a canonical configuration in which the surrounding wall is either an adiabatic surface or an isothermal surface at the ambient temperature, and the fuel level is flush with this wall. Although our description is aimed to be generally valid for all typical liquid fuels—through an adequate choice of the thermochemical parameters—in this work all results are presented for heptane.

The chapter is structured as follows. In section 2.2 a detailed mathematical formulation is given to describe the dynamics of canonical laminar pool fires. A global stability analysis and its predictions for the critical Rayleigh number are presented in section 2.3. Section 2.4 is devoted to an experimental characterization of the onset of puffing. Finally, concluding remarks are given in section 2.5.

2.2 Mathematical description of laminar pool fires

2.2.1 Governing equations

We give below the equations and boundary conditions for the description of the burning of a round pool of liquid fuel with radius a^* in a quiescent air atmosphere with temperature T_{A}^* and density ρ_{A}^*. In the presence of buoyancy, the density differences of order unity associated with the temperature increase caused by the chemical heat release induce velocities of order $v_g^* = g^* a^{*2}/\nu_{\mathrm{A}}^*$, where g^* is the gravitational acceleration, $\nu_{\mathrm{A}}^* = \mu_{\mathrm{A}}^*/\rho_{\mathrm{A}}^*$ is the ambient kinematic viscosity and μ_{A}^* is the dynamic viscosity coefficient at ambient temperature. The Reynolds number based on this velocity is the Grashof number $Gr = g^* a^{*3}/\nu_{\mathrm{A}}^{*2}$, measuring the relative effects of convective acceleration and viscous forces, with the accompanying Rayleigh number

$$Ra = Pr\,Gr = \frac{g^* a^{*3}}{\nu_{\mathrm{A}}^* D_{\mathrm{T,A}}^*}, \tag{2.1}$$

based on the thermal diffusivity of the ambient air $D_{\mathrm{T,A}}^*$, being the corresponding Péclet number that measures the ratio of convective and diffusive energy transport rates. These two parameters, related through the Prandtl number $Pr = \nu_{\mathrm{A}}^*/D_{\mathrm{T,A}}^* \simeq 0.7$, characterize the structure and dynamics of pool fires. In particular, the onset of puffing occurs at a critical value $Gr_c = Ra_c/Pr$, to be determined below.

The pool radius a^* and the characteristic velocity v_g^* will be used as scales for the dimensionless axisymmetric cylindrical coordinates $\boldsymbol{x} = (x, r)$ and velocity $\boldsymbol{v} = (v_x, v_r)$. With the time and the pressure differences from the quiescent ambient hydrodynamic distribution scaled with $t_g^* = a^*/v_g^*$ and $\rho_{\rm A}^* g^* a^*$ to give the variables t and p, respectively, the continuity and momentum equations become

$$-\frac{1}{\rho}\frac{\mathrm{D}\rho}{\mathrm{D}t} = \boldsymbol{\nabla}\cdot\boldsymbol{v}, \tag{2.2}$$

$$\frac{Ra}{Pr}\rho\frac{\mathrm{D}\boldsymbol{v}}{\mathrm{D}t} = -\boldsymbol{\nabla}p + (1-\rho)\boldsymbol{e}_x + \boldsymbol{\nabla}\cdot[\mu(\boldsymbol{\nabla}\boldsymbol{v} + \boldsymbol{\nabla}\boldsymbol{v}^T)], \tag{2.3}$$

where $\mathrm{D}/\mathrm{D}t = \partial/\partial t + \boldsymbol{v}\cdot\boldsymbol{\nabla}$ denotes the substantial derivative and ρ and μ are the density and viscosity scaled with their ambient values. The reaction between the fuel and the oxygen of the air will be considered to occur according to the global irreversible step

$$\mathrm{F} + s\mathrm{O}_2 \rightarrow (1+s)\mathrm{P} + q^*, \tag{2.4}$$

where s and q^* are the mass of oxygen consumed and the amount of heat released per unit mass of fuel burnt. The associated conservation equations for reactants and energy are

$$Ra\,\rho\frac{\mathrm{D}Y_{\rm F}}{\mathrm{D}t} = \frac{1}{Le_{\rm F}}\boldsymbol{\nabla}\cdot(\rho D_T\boldsymbol{\nabla}Y_{\rm F}) - w_{\rm F}, \tag{2.5}$$

$$Ra\,\rho\frac{\mathrm{D}Y_{\rm O}}{\mathrm{D}t} = \boldsymbol{\nabla}\cdot(\rho D_T\boldsymbol{\nabla}Y_{\rm O}) - Sw_{\rm F}, \tag{2.6}$$

$$Ra\,\rho\frac{\mathrm{D}T}{\mathrm{D}t} = \boldsymbol{\nabla}\cdot(\rho D_T\boldsymbol{\nabla}T) + qw_{\rm F}, \tag{2.7}$$

where T is the temperature scaled with $T_{\rm A}^*$, and $Y_{\rm F}$ and $Y_{\rm O} = Y_{\rm O_2}/Y_{\rm O_{2A}}$ are the mass fraction of fuel vapor and oxygen, the latter normalized with its value $Y_{\rm O_{2A}} \simeq 0.232$ in air. The dimensionless reaction rate $w_{\rm F}$ is the mass of fuel consumed by the chemical reaction per unit volume per unit time scaled with $\rho_{\rm A}^*/t_g^*$. The thermochemical parameters s and q^* defined above appear in the reaction-rate factors $S = s/Y_{\rm O_{2A}}$ and $q = q^*/(c_p^* T_{\rm A}^*)$ in (2.6) and (A.8), respectively, where c_p^* denotes the specific heat at constant pressure, assumed to be constant in the following analysis. The parameter S, of order $S = 15$ in hydrocarbon combustion, represents the amount of air needed to burn the unit mass of fuel. The other parameter, q, is the heat release per unit mass of fuel scaled with the ambient enthalpy, which takes fairly large values for typical fuels, such that $q/S \sim 7$.

Similarly to the other transport properties, the thermal diffusivity D_T is scaled with its ambient air value $D_{\rm T,A}^*$. The presumed power laws

$$\mu = \rho D_T = T^\sigma \tag{2.8}$$

will be used below for the temperature variation of the transport properties, with $\sigma = 0.7$ used in the numerical integrations. A Fickian model is used for the diffusion velocities of the reactants, a

sufficiently accurate approximation in fuel-air combustion, where the dominant presence of nitrogen molecules simplifies the description of molecular transport. While a unity Lewis number has been employed for oxygen, an excellent approximation under most conditions, a non-unity Lewis number $Le_{\mathrm{F}} > 1$ is used for the fuel, as is needed for accuracy in computations of most hydrocarbon and alcohol fuels.

The motion induced is very slow, and involves small spatial pressure variations that can be neglected in the first approximation when writing the equation of state

$$\rho T = \left[Y_{\mathrm{F}} \left(\frac{W^*_{\mathrm{A}}}{W^*_{\mathrm{F}}} - 1 \right) + 1 \right]^{-1}. \tag{2.9}$$

The molecular mass of most liquid fuels W^*_{F} is significantly larger than that of the air W^*_{A}, so that the density differences induced by the presence of the fuel vapor have been considered for increased accuracy in (2.9).

The boundary conditions in the surrounding air atmosphere can be written in the form

$$v_x = v_r = p = T - 1 = Y_{\mathrm{F}} = Y_{\mathrm{O}} - 1 = 0 \tag{2.10}$$

as $|\boldsymbol{x}| \to \infty$ for $x \neq 0$. The surface $r > 1$, $x = 0$ that surrounds the fuel pool is assumed to be impermeable and chemically inert, thereby providing the additional boundary conditions

$$v_x = v_r = \frac{\partial Y_{\mathrm{F}}}{\partial x} = \frac{\partial Y_{\mathrm{O}}}{\partial x} = 0. \tag{2.11}$$

The thermal properties of this surface can have a significant influence on the flame, with realistic cases falling in between the limits corresponding to either an adiabatic surface,

$$\frac{\partial T}{\partial x} = 0, \tag{2.12}$$

or an isothermal surface at the ambient temperature,

$$T = 1. \tag{2.13}$$

Fuel vaporization occurs with a prescribed dimensionless boiling temperature T_{B} and dimensionless latent heat of vaporization $L_v = L^*_v/(c^*_p T^*_{\mathrm{A}})$. The energy invested in raising the temperature of the liquid fuel, with specific heat c^*_l, from the ambient to the boiling temperature is taken into account by defining an effective heat of vaporization $l_v = L_v + (T_{\mathrm{B}} - 1)c^*_l/c^*_p$. The resulting boundary conditions on the vaporizing fuel surface (i.e. at $x = 0$ for $r < 1$) become

$$v_r = T - T_{\mathrm{B}} = 0 \tag{2.14}$$

$$Ra\, \rho v_x Y_{\mathrm{F}} - \frac{T^\sigma_{\mathrm{B}}}{Le_{\mathrm{F}}} \frac{\partial Y_{\mathrm{F}}}{\partial x} = Ra\, \rho v_x \tag{2.15}$$

$$Ra\, \rho v_x Y_{\mathrm{O}} - T^\sigma_{\mathrm{B}} \frac{\partial Y_{\mathrm{O}}}{\partial x} = 0 \tag{2.16}$$

$$Ra\, \rho v_x T - T^\sigma_{\mathrm{B}} \frac{\partial T}{\partial x} = -l_v Ra\, \rho v_x. \tag{2.17}$$

2.2.2 Conserved scalars from coupling functions in diffusion flames

Our analysis employs the fast-reaction limit in which the chemical-reaction terms in (2.5)–(A.8) appear as Dirac delta distributions along a flame surface separating an outer ambient region with no fuel vapor from an inner region surrounding the pool surface with no oxygen. To facilitate the analysis of the fast-reaction limit it is convenient to replace two of the equations (2.5)–(A.8) by two chemistry-free conservation equations, obtained by eliminating the reaction terms through appropriate linear combinations Liñán *et al.* (2015). We follow the derivation given in Liñán *et al.* (2016) for the analysis of counterflow gaseous diffusion flames. Thus multiplying (2.6) by q/S and adding (A.8) leads to a chemistry-free conservation equation involving a single coupling function $(T + qY_{\rm O}/S)$, which can be conveniently expressed as a normalized excess thermal and chemical enthalpy

$$\xi = \frac{T - 1 + (q/S)(Y_{\rm O} - 1)}{T_{\rm B} - 1 - q/S}, \tag{2.18}$$

with transport equation

$$Ra\,\rho\frac{{\rm D}\xi}{{\rm D}t} = \boldsymbol{\nabla}\cdot(\rho D_{_T}\boldsymbol{\nabla}\xi)\,. \tag{2.19}$$

With the normalization employed in (2.18) the excess enthalpy ξ is zero in the air atmosphere and unity on the fuel surface.

The reaction term can also be eliminated by subtracting (2.6) from (2.5) times S. When the Lewis number $L_{\rm F}$ is different from unity, the resulting transport equation shows a coupling function $(SY_{\rm F} - Y_{\rm O})$ in the accumulation and convective terms that is different from the coupling function $(SY_{\rm F}/Le_{\rm F} - Y_{\rm O})$ appearing in the diffusion term. When these coupling functions are normalized we obtain a diffusion-weighted mixture fraction

$$\tilde{Z} = \frac{SY_{\rm F}/Le_{\rm F} - Y_{\rm O} + 1}{S/Le_{\rm F} + 1}, \tag{2.20}$$

arising from the diffusion term, in addition to the classical mixture fraction

$$Z = \frac{SY_{\rm F} - Y_{\rm O} + 1}{S + 1}, \tag{2.21}$$

with resulting conservation equation

$$Ra\,\rho\frac{{\rm D}Z}{{\rm D}t} = \frac{1}{Le}\boldsymbol{\nabla}\cdot(\rho D_{_T}\boldsymbol{\nabla}\tilde{Z}), \tag{2.22}$$

where $Le = (S + 1)/(S/Le_{\rm F} + 1)$.

To solve (2.19) and (2.22) coupled with (2.2) and (2.3) and supplemented with (2.8) and (2.9) we need to relate T, $Y_{\rm F}$, and Z with ξ and $\tilde{Z}$. These relations can be obtained using the fast-reaction condition

$$Y_{\rm F}Y_{\rm O} = 0 \tag{2.23}$$

of non-coexistence of $Y_{\rm O}$ and $Y_{\rm F}$, which are simultaneously zero at the flame, given by the iso-surface $Z = Z_{\rm S} = 1/(1+S)$, or $\tilde{Z} = \tilde{Z}_{\rm S} = 1/(1+S/Le_{\rm F})$, as follows from the definitions (2.20) and (2.21). For $\tilde{Z} \geq \tilde{Z}_{\rm S}$

$$Y_{\rm O} = 0, \tag{2.24}$$

$$Y_{\rm F} = \frac{Z - Z_{\rm S}}{1 - Z_{\rm S}} = \frac{\tilde{Z} - \tilde{Z}_{\rm S}}{1 - \tilde{Z}_{\rm S}}, \tag{2.25}$$

$$T - 1 = \left(T_{\rm B} - 1 - \frac{q}{S}\right)\xi + \frac{q}{S}, \tag{2.26}$$

whereas for $\tilde{Z} \leq \tilde{Z}_{\rm S}$

$$Y_{\rm F} = 0, \tag{2.27}$$

$$1 - Y_{\rm O} = \frac{Z}{Z_{\rm S}} = \frac{\tilde{Z}}{\tilde{Z}_{\rm S}}, \tag{2.28}$$

$$T - 1 = \left(T_{\rm B} - 1 - \frac{q}{S}\right)\xi + \frac{q}{S}\frac{\tilde{Z}}{\tilde{Z}_{\rm S}}. \tag{2.29}$$

Equations (2.24)–(2.29) provide piecewise linear relations for the evaluation of $Y_{\rm F}$, $Y_{\rm O}$, and Z in terms of $\tilde{Z}$. In addition, the last relation in the equations gives T in terms of $\tilde{Z}$ and ξ.

The boundary conditions (A.12)–(2.17) become

$$v_x = v_r = p = \xi = \tilde{Z} = 0 \text{ as } |\boldsymbol{x}| \to \infty \text{ for } x \neq 0, \tag{2.30}$$

together with

$$v_x = v_r = \frac{\partial \tilde{Z}}{\partial x} = 0, \text{ at } x = 0 \text{ for } r > 1, \tag{2.31}$$

and

$$\left.\begin{aligned} v_r &= \xi - 1 = 0, \\ -T_{\rm B}^{\sigma}\frac{\partial \xi}{\partial x} &= \alpha Ra\, \rho v_x \\ -T_{\rm B}^{\sigma}\frac{\partial \tilde{Z}}{\partial x} &= Le_{\rm F} Ra\, \rho v_x (1 - \tilde{Z}) \end{aligned}\right\} \text{ at } x = 0 \text{ for } r < 1, \tag{2.32}$$

where

$$\alpha = \frac{l_v + T_{\rm B}}{q/S + 1 - T_{\rm B}}. \tag{2.33}$$

The definition of the problem is completed by specifying the thermal boundary condition at the surrounding wall $x = 0$, $r > 1$, which, for the case of an adiabatic surface may be written as

$$\frac{\partial \xi}{\partial x} = 0 \tag{2.34}$$

whereas, for the case of an isothermal surrounding wall at ambient temperature,

$$\xi = \begin{cases} \dfrac{q/S}{q/S + 1 - T_{\rm B}} & \text{for } \tilde{Z} \geq \tilde{Z}_{\rm S}, \\ \dfrac{q/S}{q/S + 1 - T_{\rm B}}\dfrac{\tilde{Z}}{\tilde{Z}_{\rm S}} & \text{for } \tilde{Z} \leq \tilde{Z}_{\rm S}. \end{cases} \tag{2.35}$$

2.2.3 Numerical methods

Steady solutions of the governing equations (2.2), (2.3), (2.19) and (2.22), supplemented with relations (2.8), (2.9), (2.24)–(2.29), and subject to the boundary conditions (2.30)–(2.35), are computed with a Newton-Raphson root-finding technique. The discretization of the problem is carried out with use made of the software FreeFem++ using Taylor-Hood elements ($P2$ for velocity and passive scalars and $P1$ for the pressure field to satisfy the Ladyzhenskaja-Babuška-Brezzi condition). Details of the discretization method, used for instance by (Garnaud *et al.*, 2013*b*), can be found in (Hecht, 2012). The grid is adapted to the solution using a Delaunay triangulation of the computational domain $\boldsymbol{x} \in [0, x_{\max}] \times [0, r_{\max}]$. The size of the computational box and the grid refinement level are varied until convergence is achieved, being $(x_{\max}, r_{\max}) = (150, 50)$ typical values used in the results presented below. The finite size of the domain demands replacement of (2.30) by stress-free boundary conditions at the lateral $r = r_{\max}$, $x \geq 0$ and outflow $x = x_{\max}$, $r \geq 0$ computational boundaries for the flow field (see, for instance, (Moreno-Boza *et al.*, 2016) for details). The condition $\bar{\tilde{Z}} = \bar{\xi} = 0$ at the lateral boundary, and $\boldsymbol{n} \cdot \boldsymbol{\nabla} \bar{\tilde{Z}} = \boldsymbol{n} \cdot \boldsymbol{\nabla} \bar{\xi} = 0$ at the outflow boundary complete the numerical description of the steady problem.

On the other hand, unsteady solutions of the governing equations have been obtained with the numerical code presented in Carpio *et al.* (2016). The numerical code uses as space discretization a local anisotropic h-adaptive algorithm in a finite element framework. The finite element spaces are the same employed in the steady computations, described before (quadratic finite elements for coupling functions and velocity, and linear finite elements for pressure). As time discretization scheme the code uses a semi-Lagrange-Galerkin method in combination with second order BDF schemes. The semi-Lagrange-Galerkin method allows to treat the convective terms in a stable way, and to decouple the momentum and mass conservation equations from the conservation equations for the passive scalars Z, $\tilde{Z}$ and ξ. Moreover, this time discretization has the ability to transform the nonlinear momentum and mass conservation equations into a linear Stokes problem which is solved with a preconditioned conjugate gradient Uzawa algorithm. Equations for the passive scalars Z, $\tilde{Z}$ and ξ are solved with a fixed-point iteration to treat the weak nonlinearity induced by nonunity Lewis number and the dependence of the density and diffusion coefficients with Z, $\tilde{Z}$ and ξ.

2.2.4 Choice of parameters and sample results for a steady heptane flame

The formulation presented previously is generally valid for any fuel, given an adequate choice of the thermochemical parameters. In the present work, attention is focused on heptane; table 2.1 summarizes the numerical values for all the parameters that appear in the description. It

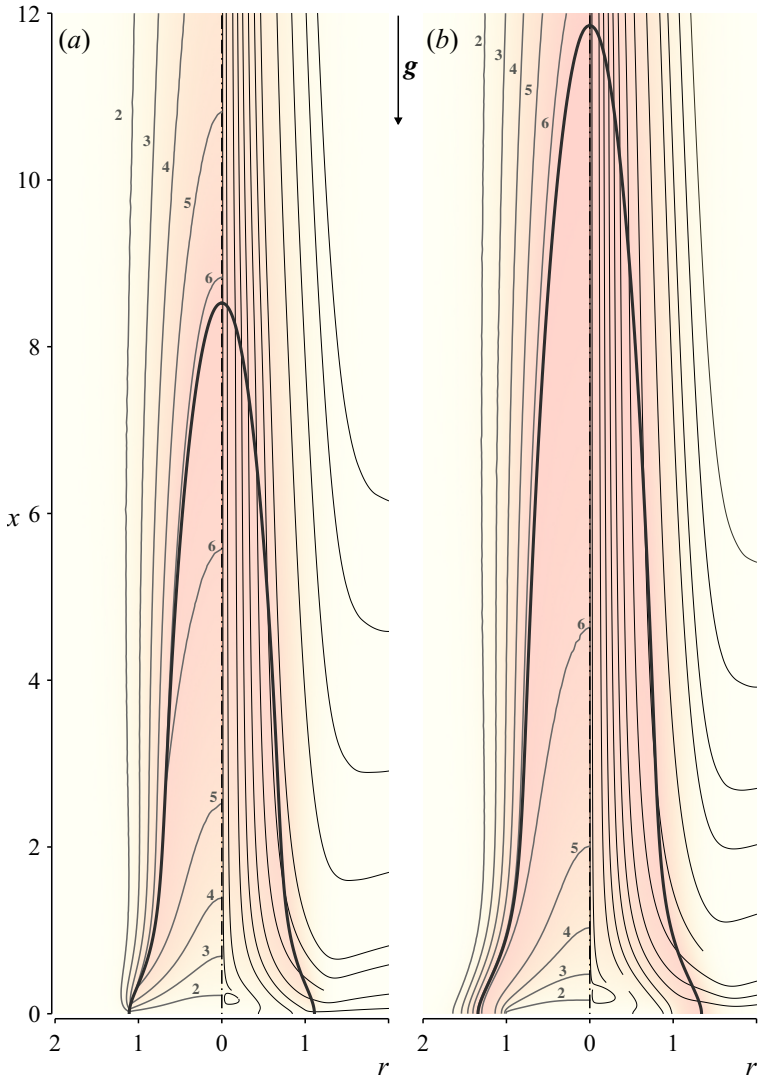

Figure 2.1: Steady solutions for $Ra = 10000$ with (a) isothermal, and (b) adiabatic boundary conditions on the surrounding surface. The left part of each plot shows equispaced isotherms along with their corresponding temperature values; sample streamlines are shown on the right hand sides. The solid line indicates the stoichiometric line $\tilde{Z} = \tilde{Z}_{\mathrm{S}}$.

must be noted that the Lewis number of the fuel varies considerably throughout the flame, with values ranging from 1.1 on the vaporizing fuel surface to 2.6 at the flame front. As our formulation assumes a constant Lewis number, an intermediate value of 1.8 is chosen.

Soot production causes heptane flames to be luminous, and consequently lose heat through radiation. As this effect is anticipated to be small for the flame size associated with the onset of puffing, it is here modeled in a simplistic manner by lowering the value of the heat release parameter q/S from 7 to $q_{\mathrm{eff}}/S = 6$, such that the resulting peak flame temperatures are on the order of 1900 K, in accordance with measurements of similar flames in the literature Reimann *et al.* (2010).

The governing equations (2.2), (2.3), (2.19) and (2.22), supplemented with relations (2.8),

Table 2.1: Values for heptane of the thermochemical parameters used in the description.

$W_{\mathrm{F}}^*/W_{\mathrm{A}}^*$	3.45	S	15.2
T_B	1.24	q/S	7
l_v	1.14	q_{eff}/S	6
Le_{F}	1.8		

(2.9), (2.24)–(2.29), and subject to the boundary conditions (2.30)–(2.35), are to be integrated numerically. Given an initial condition, they can be mar-ched in time as described in 2.2.3. Alternatively, steady solutions may be computed using a Newton–Raph-son algorithm the details of which also can be found in 2.2.3. Figure 2.1 shows the structure of a steady heptane flame at $Ra = 10000$ distinguishing between (a) an isothermal, and (b) an adiabatic surrounding surface. In each plot the left hand side shows equispaced isotherms along with their corresponding values, whereas on the right hand side sample streamlines are drawn. The heat loss to the isothermal wall at temperature $T = 1$ causes the flame to be considerably shorter than in the adiabatic case.

2.3 Puffing as a hydrodynamic global mode

It has recently been shown that the flickering of low-density jets Coenen *et al.* (2017) and jet diffusion flames Moreno-Boza *et al.* (2016) is the manifestation of a hydrodynamic global instability, the onset of which can be computed with a linear global stability analysis. In the present work, we employ said analysis to predict the onset of puffing of laminar pool fires. Let us recast the equations of motion (2.2), (2.3), (2.19) and (2.22), supplemented with relations (2.8), (2.9), (2.24)–(2.29), and subject to the boundary conditions (2.30)–(2.35), in the compact form

$$\frac{\partial \boldsymbol{q}}{\partial t} = \mathcal{F}(\boldsymbol{q}), \tag{2.36}$$

where $\boldsymbol{q} = (\boldsymbol{v}, p, \tilde{Z}, \xi)$ is the state vector and $\mathcal{F}$ is a nonlinear differential operator, representing the steady part of the continuity (2.2), Navier–Stokes (2.3) and passive scalars conservation equations (2.19) and (2.22).

As a base state for the stability analysis, a steady solution of (2.36) is employed, i.e. $\bar{\boldsymbol{q}} = (\bar{\boldsymbol{v}}, \bar{p}, \bar{\tilde{Z}}, \bar{\xi})$ such that $\mathcal{F}(\bar{\boldsymbol{q}}) = 0$, as described in section 2.2.4. Small unsteady axisymmetric perturbations are added to the steady base flow as $\boldsymbol{q} = \bar{\boldsymbol{q}} + \epsilon \boldsymbol{q}'$. The evolution of these perturbations (primed quantities) is then governed to leading order by (2.36), linearized around the base flow. Assuming temporal eigenmodes $\boldsymbol{q}' = \hat{\boldsymbol{q}} \mathrm{e}^{-\mathrm{i}\omega t}$, the linearized equations of motion with corresponding boundary conditions can be written in the form of a generalized eigenvalue problem

$$(\boldsymbol{A} - \mathrm{i}\omega \boldsymbol{B})\, \hat{\boldsymbol{q}} = 0. \tag{2.37}$$

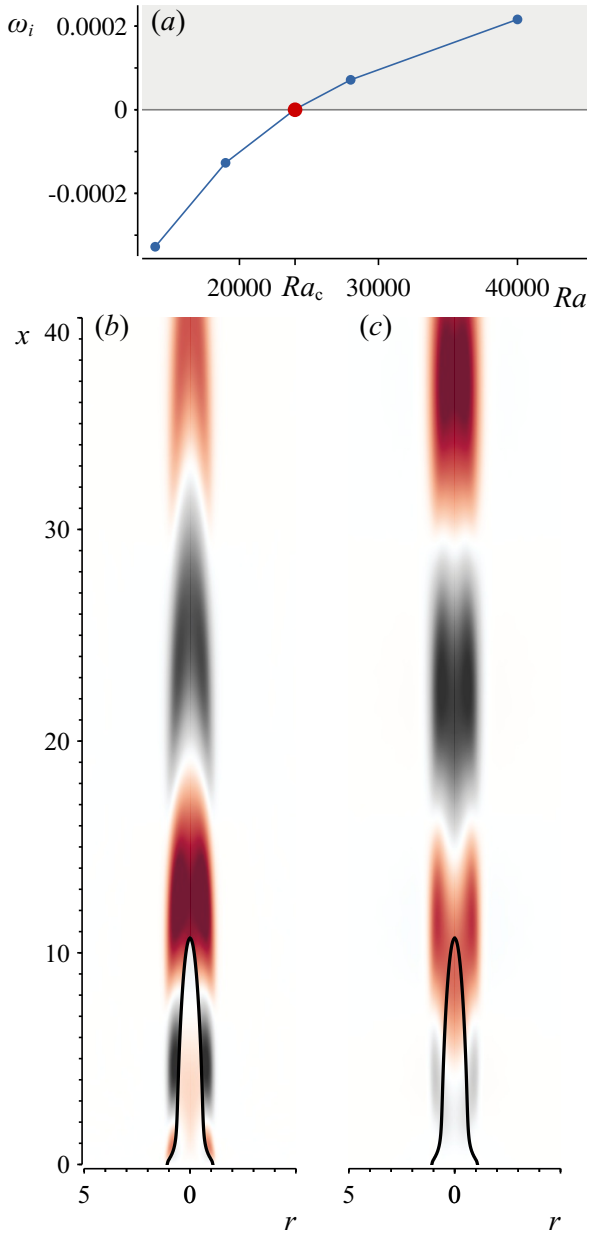

Figure 2.2: (a) Growth rate of the leading eigenvalue as a function of the Rayleigh number for a heptane pool fire surrounded by an isothermal surface. Associated (normalized) eigenfunctions for (b) the temperature $\hat{T}$ and (c) the axial velocity $\hat{v}_x$ at the onset of instability, $Ra = Ra_c = 24000$, highlighted in red in (a); the thick black line indicates the stoichiometric surface of the corresponding steady base flame.

Nontrivial solutions exist for a discrete set of complex values of $\omega = \omega_r + \mathrm{i}\,\omega_i$. The real part of ω determines the frequency of the perturbation, with corresponding Strouhal number $St = \omega_r/\pi$. The growth rate ω_i dictates whether the flow is globally unstable ($\omega_i > 0$) or globally stable ($\omega_i < 0$). The same finite-element formalism is employed to discretize the perturbed equations but in a split mesh with twice as much nodes than that used for the base flow. The shift-inverse power method

Table 2.2: Critical Rayleigh number Ra_c and corresponding Strouhal number St_c obtained from the global stability analysis.

Surrounding surface	Ra_c	St_c
Adiabatic	11600	0.0040
Isothermal at temperature $T = 1$	24000	0.0034

Lehoucq *et al.* (1997) is employed to solve the eigenvalue problem.

The global eigenvalue spectra for buoyant pool fires share the characteristics of those encountered in diffusion flames Moreno-Boza *et al.* (2016) and low-density jets Coenen *et al.* (2017): an isolated, physically significant, leading eigenvalue, and a stable arc-branch of eigenmodes with lower growth rates. Whereas the latter modes are heavily dependent on the numerical implementation such as the choice of domain size, the leading eigenvalue is robust. Figure 2.2(a) shows for the canonical case of a heptane pool fire surrounded by an isothermal surface how the growth rate of the physically significant leading eigenvalue increases with the Rayleigh number. The margin of instability, separating globally stable fires (negative growth rates) from globally unstable fires (positive growth rates) lies at $Ra = Ra_c = 24000$. At the onset, the dimensionless frequency of the global mode is $St = \omega_r/\pi = 0.0034$, and the spatial structures of its corresponding temperature and axial velocity eigenfunctions are given in figures 2.2(b) and (c), respectively.

When the surface surrounding the fuel pool is adiabatic instead of isothermal, the resulting flame is considerably larger (see figure 2.1). This causes the flame to be more unstable, and thus have a smaller critical Rayleigh number. Indeed, the global stability analysis predicts a value of $Ra_c = 11600$, with a corresponding frequency $St_c = 0.0040$. Table 2.2 summarizes the results for both canonical cases.

2.4 Comparison with an experiment

2.4.1 Setup

To determine the critical conditions for the onset of pool-fire puffing, controlled experiments were carried out, in which, for a fixed fuel (heptane) and under fixed ambient conditions, the flame dynamics were characterized for different fuel pool sizes. Note that the fuel pool radius a^* is related to the Rayleigh number as $Ra = g^* {a^*}^3/(\nu^*_{\mathrm{A}} D^*_{\mathrm{T,A}})$ with $g^* = 9.807\,\mathrm{m/s^2}$, $\nu^*_{\mathrm{A}} = 1.597 \times 10^{-5}\,\mathrm{m^2/s}$, and $D^*_{\mathrm{T,A}} = 2.256 \times 10^{-5}\mathrm{m^2/s}$.

The experimental setup is depicted in figure 2.3. It consists of a $90\,\mathrm{cm} \times 90\,\mathrm{cm} \times 12.7\,\mathrm{mm}$ PVC table that in its center holds a removable liquid fuel burner. This burner is composed of a $20\,\mathrm{cm} \times 20\,\mathrm{cm} \times 6.35\,\mathrm{mm}$ aluminum plate, a 6 cm-diameter conical polypropylene fuel holder

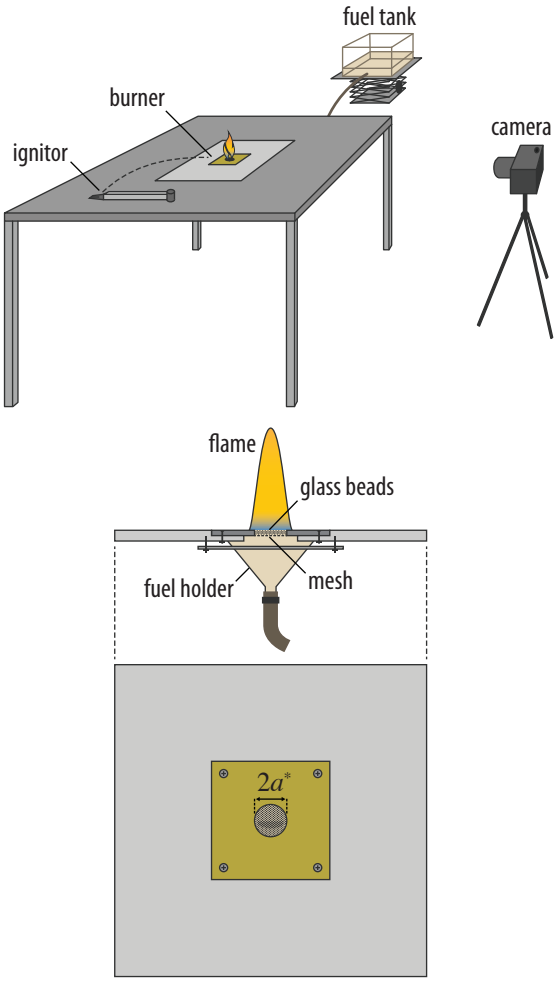

Figure 2.3: Schematics of the experimental setup. The upper diagram shows the general setup, whereas the lower part shows a more detailed side and top view of the liquid fuel burner.

mounted underneath, and a small interchangeable 7.5 cm × 7.5 cm × 3.175 mm brass plate placed within a recess in the upper side of the former. The interchangeable plate has a circular hole of a certain radius a^* in its center, filled up to a small distance of 0.75 ± 0.25 mm from the rim with a layer of glass beads (0.5 mm in diameter) that rests on a thin stainless steel mesh. This porous layer prevents convective currents in the fuel from affecting the observations. When assembled, all elements form a large flush surface around the circular hole. The fuel holder is connected to an external fuel tank with a cross-sectional area of approximately $350\,\mathrm{cm}^2 \gg \pi a^{*2}$. In this manner, once the height of the tank is adjusted so that the burner is filled up to the desired level with fuel, this level remains quasi-constant during the course of an experiment (typically about ten minutes).

To prevent external perturbations to the flame, the complete experiment is enclosed by a 3 m × 2 m × 2 m chamber. After closing the chamber, we waited approximately 10 minutes for all air currents to die out before starting the experiment. To ignite the fuel remotely, a surface ignitor

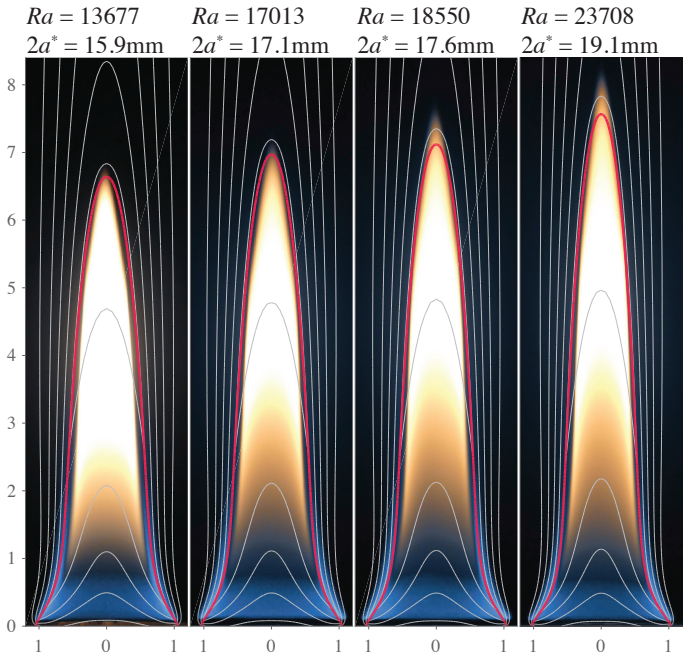

Figure 2.4: Steady subcritical heptane flames for different pool diameters. Superposed on the photographs are numerical computations following the simplified description given in section 2.2; the thick red line indicates the flame front, and the thin gray lines indicate equispaced isotherms $T = 2, 3, 4, 5, 6$. Note that, in order to mimic the experimental conditions, the axial location of the vaporizing fuel surface in the numerical computations is set to $x = -0.75\,\mathrm{mm}/a^*$.

mounted on a motorized arm was slowly brought close to the fuel and retracted afterwards. The flame dynamics were recorded with a Panasonic Lumix FZ300 camera at a frame rate of 120 fps. For unstable flames, the puffing frequency can be determined from the image sequence by selecting a region of the image near the flame tip and computing the power spectral density of the temporal evolution of the average intensity in that region. The length of the sequency was typically taken to be one minute, containing 600 puffing cycles at an expected puffing frequency of 10 Hz. In addition to visible light photographs, shadowgraph images were taken by placing a 3 W led light in the focal point of a convex lense, situated 150 cm in front of the flame, and projecting the image on a white paper screen 70 cm behind the flame.

2.4.2 Results and discussion

For sufficiently small pool diameters, steady flames were obtained. Figure 2.4 shows photographs of such steady flames for $2a^* = 15.6$, 17.1, 17.6, and 19.1 mm ($Ra = 13677$, 17013, 18550, and 23708). Dimensionless length scales are used in the axes, so that $r = 1$ corresponds to the border of the fuel pool. Superposed on the photographs are steady numerical computations following the simplified description given in section 2.2. The thick red line indicates the stoichiometric

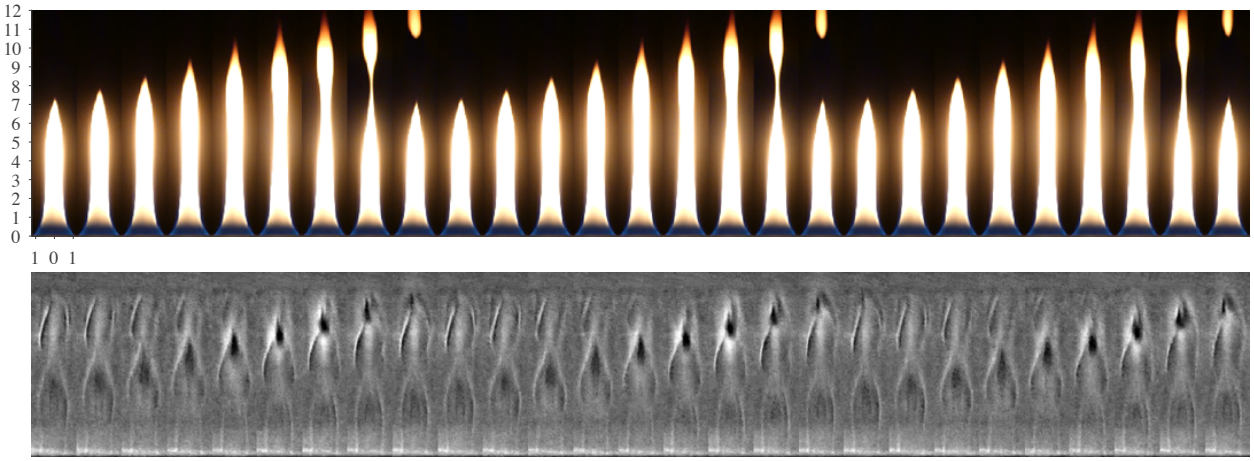

Figure 2.5: (top) Visible light, and (bottom) shadowgraph sequence of three puffing cycles for a supercritical heptane pool fire with diameter $2a = 20.1\,\mathrm{mm}$ ($Ra = 27631$). The time interval between the images is $1/120\,\mathrm{s}$. The measured puffing frequency for this case is $f^* = 12.8\,\mathrm{Hz}$ ($St = 0.0041$). Note that the top and bottom sequence do not correspond to the same puffing events, and that both have different length scales.

line, and the thin gray lines are equispaced isotherms. Two aspects must be considered in the comparison between experiments and theory. First, the conductive heat transfer inside the brass plate that surrounds the fuel pool in the experiments is very effective compared to the combined convective and conductive heat transfer in the adjacent gaseous fuel or air. Therefore, from the two canonical cases considered in the theoretical description, namely the pool fire surrounded by an adiabatic wall, and that surrounded by an isothermal wall, the latter is expected to be most similar to the experiments, and is hence used in the computations. Secondly, to avoid fuel spilling in an uncontrolled fashion, a very small offset of $0.75 \pm 0.25\,\mathrm{mm}$ is maintained between the fuel level and the rim in the experiments. In the numerical computations of figure 2.4, this is taken into account by setting the axial location of the fuel level to $x = -0.75\,\mathrm{mm}/a^*$, while keeping the surrounding isothermal surface at $x = 0$.

When the pool diameter is increased to $2a^* = 20.1\,\mathrm{mm}$ ($Ra = 27631$), the steady character of the flow is lost and the flame start puffing in a periodic manner. Figure 2.5 shows three oscillation cycles, the top panel in the form of visible light photographs, and the bottom panel in the form of shadowgraph images. The shadowgraph images show the large vortical structures that characterize the flame envelope. These are in qualitative agreement with the eigenmodes near criticality obtained from the global stability analysis (figures 2.2(b) and (c)). A quantitative comparison is not pertinent, as it is clear from the large oscillation amplitudes in figure 2.5 that at $Ra = 27631$ nonlinear effects already play a role in the flow dynamics. The shadowgraph images confirm that the perturbation wave length is comparable to the flame height, and emphasize the need for a global stability analysis

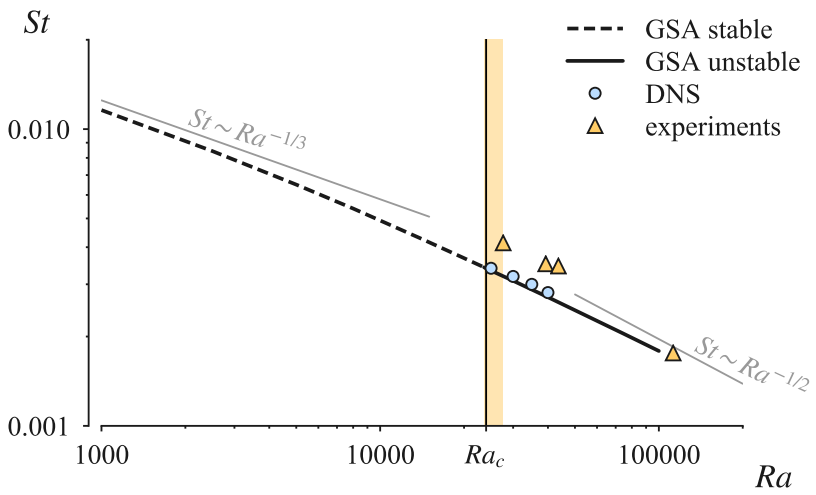

Figure 2.6: Dimensionless puffing frequency as a function of the Rayleigh number. Triangles correspond to experimental results; circles are computed from time-dependent direct numerical simulations of the governing equations. The frequency of the leading eigenvalue from the global stability analysis (GSA) is indicated with a solid line in the unstable regime, and a dashed line in the stable regime. The solid vertical line designates the onset $Ra = Ra_c = 24000$ predicted by the GSA, whereas the shaded interval corresponds to the experimentally obtained threshold of instability, $23708 < Ra_c < 27631$.

that takes into account this intrinsic nonparallelism of the flow field.

The critical Rayleigh number in the experiment lies between $Ra = 23708$ and $Ra = 27631$. This is in good quantitative agreement with the prediction $Ra_c = 24000$ of the global stability analysis for the canonical case in which the fuel level is flush with the surrounding surface, and the latter is assumed to be isothermal at the ambient temperature. If the experimental conditions are mimicked in the global stability computations by lowering the fuel level with respect to the rim a small distance of 3.25% of the pool diameter (0.75 mm/20.1 mm), the predicted critical Rayleigh number increases to $Ra_c = 28000$.

When interpreting the numerical value of the critical Rayleigh number, one must take into account that it was defined in 2.1 using the ambient values of the thermal diffusivity and the kinematic viscosity. Taking into account that both increase with the temperature as $T^{1+\sigma}$, and that the peak flame temperatures are approximately six times larger than that of the ambient, the numerical value of the corresponding Rayleigh number scaled with the peak properties at the flame would be approximately 440 times smaller.

The puffing frequency for the $2a^* = 20.1$ mm fuel pool ($Ra = 27631$) is $f^* = 12.8$ Hz, corresponding to a Strouhal number $St = f^* 2a^*/(g^* a^{*2}/\nu_A^*) = 0.0041$—based on the diameter to follow the convention in the literature. To explore the supercritical regime, three additional larger pool sizes were considered ($2a^* = 22.6$, 23.4, and 32.1 mm), yielding periodically puffing pool fires

with a frequency that decreases with the pool size (figure 2.6, triangles). The error in the frequency measurement was estimated to be less than 0.75 Hz, which was the largest observed variation in the measured puffing frequency over different one-minute sequences, yielding error bars in 2.6 that are smaller than the symbols. For comparison, the frequency of the leading eigenvalue obtained from the linear global stability analysis (GSA) is also included in figure 2.6 (solid and dashed line), as well as the oscillation frequency obtained from fully nonlinear direct numerical simulations of the governing equations (circles). The agreement between the GSA and the nonlinear computations is good in the vicinity of the bifurcation. Note that outside this region, the results from the global stability analysis are not to be expected to be in good quantitative agreement with the full nonlinear behavior of the flow. For example, for the well known flow around a cylinder, the vortex shedding frequency quickly differs from the frequency of the unstable leading eigenvalue as the bifurcation parameter—the Reynolds number in that case—is increased Barkley (2006). It is known that in such flows, a global stability analysis around the mean flow instead of the steady solution of the governing equations does give good agreement Beneddine *et al.* (2016).

The growth and frequency selection mechanisms governing the global instability of buoyant diffusion flames act primarily in the flame envelope characterized by large density and velocity gradients Moreno-Boza *et al.* (2016). Therefore, on theoretical grounds, a scaling law for the frequency associated with the instability can be derived from a balance between the unsteady and convective terms in the momentum equation, i.e. $f^* \sim V^*/X^*$, where $V^* \sim (g^* X^*)^{1/2}$ is the velocity induced by buoyant acceleration of the flow, and X^* is the characteristic size of this region. For sufficiently large fuel pools, X^* is typically on the order of the pool size a^*, and consequently $f^* \sim g^{*1/2} a^{*-1/2}$. For smaller fuel pools on the contrary, buoyancy starts entering the problem at a distance $X^* \sim \nu_{\mathrm{A}}^{*2/3} g^{*-1/3}$, larger than a^*, leading to $f^* \sim g^{*2/3} \nu_{\mathrm{A}}^{*-1/3}$. In dimensionless terms, using the scales introduced at the beginning of this section, both regimes can be written as $St \sim Ra^{1/2}$ and $St \sim Ra^{1/3}$, respectively, and are indicated in figure 2.6 by the dotted lines.

2.5 Conclusions

In this chapter, a simple mathematical description for the structure of liquid-fuel pool fires has been provided. The onset of puffing of heptane flames is described using global stability techniques, providing the critical Rayleigh number (critical pool diameter) and associated frequencies. The results are assessed by small-scale laboratory experiments and direct numerical computations. Good agreement is found between both steady computations of the flame shape for stable flames and the critical conditions for the onset of instability. It is worth mentioning that the description is sensitive to the choice of the numerical values of the relevant thermochemical parameters. For

instance, whilst most of them are well known physical parameters, there remains some arbitrariness in the choice of the apparent Lewis number of the fuel Le_{F} and of the effective nondimensional heat release parameter q_{eff}/S, necessary to model radiative heat losses.

Future prospects

In this section, a brief description of some unresolved research problems related to the work presented in Chapters 1 and 2 is given.

Perhaps the most immediate extension of the work pressented in Chapter 2 is the alternative choice of fuels and the consideration of planar flame configurations. The formulation proposed in section 2.2, accounting for the nonunity Lewis number of the fuel, provides a simple yet useful mathematical framework for the study of both the structure and the stability of pool fires. Predictions on the onset of instability and flame structure remain accurate as long as the thermochemical properties of the fuel are chosen properly. While heptane has been used through the analysis, it is worth clarifying the role of using a different fuel on the stability properties of the subsequent flow field.

Regarding its structure, pool fires are known to transition from the oscillating state of puffing to a more destructive regime, known as fire whirl. Fire whirls, often visualized as huge swirling columns of fire, are present, for instance, in the spread of wildfires and the combustion of oil spills. Their swirl properties and thus higher combustion efficiency has raised recent interest on clarifying the transition from the puffing regime to fire whirl. Experimental evidence has confirmed that a fire whirl may develop subsequently to the axisymmetric puffing regime, characterized by the triggering of an unstable axisymmetric mode, where symmetry is broken in favour of a helical motion induced by air entrainment from the surrounding ambient. Upon further increasing the swirling intensity, vortex breakdown may occur in the inner core of the flow, producing a transition to the recently discovered regime of blue whirl (Xiao *et al.*, 2016). Most of what is known about fire whirls comes from scale modeling experiments in the laboratory and therefore a full theoretical description of the underlying mechanisms responsible for these transitions remains yet unknown and poses a challenging problem. An borad overview of the structure and dynamics of fire whirls can be found, for instance, in (Tohidi *et al.*, 2017).

The global linearized approach opens up a range of possibilities for further studies. For instance, the computation of the adjoint modes—with the discretized Navier–Stokes operators at one's disposal, the discrete adjoint can be obtained in a straightforward manner by solving the conjugate-transposed eigenvalue problem—readily permits a structural sensitivity analysis in the sense of Giannetti & Luchini (2007). There, the sensitivity of the eigenvalue with respect to 'internal

feedback' mechanisms is obtained by measuring the local overlap between the direct and the adjoint eigenfunctions. It is argued that flow regions where this measure is large contribute strongly to the eigenvalue selection and thus represent the 'wavemaker' of the eigenmode. The analysis of the adjoint problem can be for instance based upon the strategy known as the *adjoint of the discrete system*, in which the discrete adjoint eigenvector $\tilde{\boldsymbol{q}}^+$ is the solution of the adjoint eigenvalue problem associated to (2.37). Following the formalism introduced in (Giannetti & Luchini, 2007), such an analysis requires first the definition of an inner product. Assuming $\hat{\boldsymbol{q}}_1$ and $\hat{\boldsymbol{q}}_2$ are two (not necessarily different) perturbed states, our definition of the inner product is as follows

$$\langle \hat{\boldsymbol{q}}_1, \hat{\boldsymbol{q}}_2 \rangle := \int_\Omega \left(\tilde{v}_{x_1}^* \tilde{v}_{x_2} + \tilde{v}_{r_1}^* \tilde{v}_{r_2} + \hat{\tilde{Z}}_1^* \hat{\tilde{Z}}_2 + \hat{\xi}_1^* \hat{\xi}_2 \right) \mathrm{d}\Omega \simeq \tilde{\boldsymbol{q}}_1^H \, \boldsymbol{Q} \, \tilde{\boldsymbol{q}}_2, \tag{2.38}$$

where Ω is the computational domain, * denotes complex conjugate and ^{H} denotes conjugate transpose. The diagonal, positive definite hermitian $N \times N$ matrix $\boldsymbol{Q}$ contains the metric coefficient associated to the spatial discretization, where N is the number of degrees of freedom. With the definition (2.38), the discrete adjoint eigenvalue problem is given by

$$\left(\boldsymbol{A}^+ - \mathrm{i}\omega^+ \boldsymbol{B}^+ \right) \tilde{\boldsymbol{q}}^+ = \left(\boldsymbol{Q}^{-1} \boldsymbol{A}^H \boldsymbol{Q} - \mathrm{i}\omega^+ \boldsymbol{Q}^{-1} \boldsymbol{B}^H \boldsymbol{Q} \right) \tilde{\boldsymbol{q}}^+ = 0, \tag{2.39}$$

which is solved employing the same iterative technique for the direct problem. As a result, one obtains the adjoint eigenvector $\hat{\boldsymbol{q}}^+$, normalized according to $\hat{\boldsymbol{q}}^{+H} \boldsymbol{Q} \boldsymbol{B} \hat{\boldsymbol{q}} = 1$, and its associated eigenvalue $\omega^+ = \omega^*$. The structural sensitivity, as defined by Giannetti & Luchini (2007),

$$\lambda(\boldsymbol{x}) = \|\boldsymbol{Q}\tilde{\boldsymbol{q}}^+\| \, \|\tilde{\boldsymbol{q}}\|, \tag{2.40}$$

where pressure is excluded from $\tilde{\boldsymbol{q}}$ and $\tilde{\boldsymbol{q}}^+$, gives a scalar measure of where introduction of a feedback-forcing proportional to the local direct global mode may affect the most on the eigenvalue drift. Indeed, the definition given in (2.40), stems from a sensitivity analysis in which changes on the eigenvalue are obtained as a function of changes—introduced as a feedback forcing proportional to $\tilde{\boldsymbol{q}}$—in the linearized operator $\boldsymbol{A}$, giving rise to the definition of the structural sensitivity tensor $\boldsymbol{S} = \boldsymbol{Q}\tilde{\boldsymbol{q}}^+ \otimes \tilde{\boldsymbol{q}}$. Therefore, the structural senstivity is also the Frobenius norm of the structural sensitivity tensor, $\lambda = \|\boldsymbol{S}\|_{\mathbb{F}}$. The region in which $\lambda(\boldsymbol{x})$ is maximum represents the so-called wavemaker and is referred to as the core (or origin) of the instability (Schmid & Brandt, 2014). A sample numerical result is provided for a methanol flame with $Ra = 10000$ in Fig. 2.7 (the thermochemical properties of this fuel are presented in the caption), where the structural senstitivity is shown for the adjoint mode associated to the most unstable global direct mode.

Another interesting concept that can be readily applied is the sensitivity to a steady body force or to modifications in the base flow (Marquet *et al.*, 2008). This is particularly relevant in the context of passive control techniques, such as the introduction of an adequately positioned control

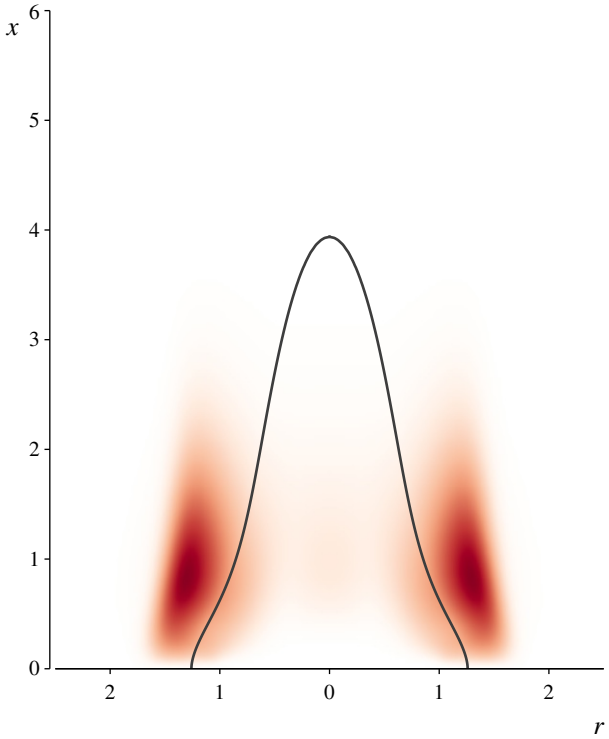

Figure 2.7: Colorplot of the structural sensitivity λ (white means $\lambda = 0$ and red indicates the maximum value of λ) for a methanol flame for $Ra = 10000$. The thermochemical parameters of this fuel are taken as $W_{\mathrm{F}}/W_{\mathrm{A}} = 1.1$, $L_v = 2.70$, $T_{\mathrm{B}} = 1.12$, $Le_{\mathrm{F}} = 1.20$, $q/S = 7.7$ and $S = 6.47$.

cylinder to stabilize the flame flicker (see, for instance Toong *et al.*, 1965). These sensitivity analyses have been recently applied to nonbuoyant lifted flames (Qadri *et al.*, 2015). On the other hand, linear nonmodal stability techniques may also be applied to investigate the discrepancy between the onset of instability predicted by the global stability analysis and that obtained by DNS. A similar difference has recently been encountered by Coenen *et al.* (2016) in low-density jets when comparing the results of a global stability analysis with the experimental observations of Hallberg & Strykowski (2006). In that regard, the computation of the pseudospectrum (Trefethen & Embree, 2005) of the linearized Navier–Stokes operator can show if non-normality plays a role. For the low-density jet, a very large gain in the frequency response (see also Garnaud *et al.*, 2013*a*) was found, even for Reynolds number substantially smaller than the critical value. These aspects should be investigated for buoyant jet diffusion flames in future work.

Bibliography

Akita, K. & Yumoto, T. 1965 Heat transfer in small pools and rates of burning of liquid methanol. *Proc. Symp. (Int.) Comb.* **10**, 943–948.

Barkley, D. 2006 Linear analysis of the cylinder wake mean flow. *Europhys. Lett.* **75** (5), 750–756.

Beneddine, S., Sipp, D., Arnault, A., Dandois, J. & Lesshafft, L. 2016 Conditions for validity of mean flow stability analysis. *J. Fluid Mech.* **798**, 485–504.

Blinov, V.I. & Khudyakov, G.N. 1961 Diffusion burning of liquids. *Tech. Rep.* T-1490a-c. Izdatel'stvo Akademii Nauk SSSR, Moscow.

Byram, G.M. & Nelson, R.M. 1970 The modeling of pulsating fires. *Fire Tech.* **6** (2), 102–110.

Carpio, J., Prieto, J.L. & M., Vera 2016 A local anisotropic adaptive algorithm for the solution of low-mach transient combustion problems. *J. Comput. Phys.* **306**, 19–42.

Cetegen, B.M. & Ahmed, T.A. 1993 Experiments on the periodic instability of buoyanty plumes and pool fires. *Combust. Flame* **93**, 157–184.

Chatterjee, P., Wang, Y., Meredith, K.V. & Dorofeev, S.B. 2015 Application of a subgrid soot-radiation model in the numerical simulation of a heptane pool fire. *Proc. Combust. Inst* **35** (3), 2573–2580.

Coenen, W., Lesshafft, L., Garnaud, X. & Sevilla, A. 2016 Global instability in low-density jets: physical eigenmodes and spurious feedback effects. *J. Fluid Mech.* p. submitted.

Coenen, W., Lesshafft, L., Garnaud, X. & Sevilla, A. 2017 Global instability of low-density jets. *J. Fluid Mech.* **820**, 187–207.

Delichatsios, M.A. 1996 Gravitational fluctuations in pool fires and pool buoyant flows. *Combust. Sci. Tech* **112**, 355–358.

Emmons, H.W. 1961 Some observations on pool burning. In *International Symposium on the Use of Models in Fire Research* (ed. W.G. Berl), pp. 50–67. National Academy of Sciences—National Research Counsel.

Emmons, H.W. 1980 Scientific progress on fire. *Annu. Rev. Fluid Mech.* **12**, 223–236.

Emori, R.I. & Saito, K. 1983 A study of scaling laws in pool and crib fires. *Combust. Sci. Tech.* **31** (5-6), 217–231.

Finney, M.A., Cohen, J.D., Forthofer, J.M., McAllister, S.S., Gollner, M.J., Gorham, D.J., Saito, K., Akafuah, N.K., Adam, B.A. & English, J.D. 2015 Role of buoyant flame dynamics in wildfire spread. *PNAS* **112** (32), 9833–9838.

Garnaud, X., Lesshafft, L., Schmid, P.J. & Huerre, P. 2013*a* The preferred mode of incompressible jets: linear frequency response analysis. *J. Fluid Mech.* **716**, 189–202.

Garnaud, X., Lesshafft, L., Schmid, P. J. & Huerre, P. 2013*b* Modal and transient dynamics of jet flows. *Phys. Fluids* **25**, 044103.

Ghoniem, A.F., Lakkis, I. & Soteriou, M. 1996 Numerical simulation of the dynamics of large fire plumes and the phenomenon of puffing. *Symp. (Int.) Combust.* **26**, 1531–1539.

Giannetti, F. & Luchini, P. 2007 Structural sensitivity of the first instability of the cylinder wake. *J. Fluid Mech.* **581**, 167–197.

Hallberg, M. P. & Strykowski, P. J. 2006 On the universality of global modes in low-density axisymmetric jets. *J. Fluid Mech.* **569**, 493–507.

Hamins, A., Yang, J.C. & Kashiwagi, T. 1992 An experimental investigation of the pulsation frequency of flames. *Symp. (Int.) Combust.* **24**, 1695–1702.

Hecht, F. 2012 New development in FreeFem++. *J. Numer. Math.* **20** (3-4).

Hertzberg, M., Cashdollar, K., Litton, C. & Burgess, D. 1978 The diffusion flame in free convection: buoyancy-induced flows, oscillations, radiative balance, and large-scale limiting rates. *Tech. Rep.* 8263. Dept. of the Interior, Bureau of Mines.

Heskestad, G. 1998 Dynamics of the fire plume. *Phil. Trans. R. Soc. A* **356** (1748), 2815–2833.

Joulain, P. 1998 The behavior of pool fires: state of the art and new insights. *Symp. (Int.) Combust.* **27**, 2691–2706.

Lehoucq, R.B., Sorensen, D.C. & Yang, C. 1997 Arpack users guide: Solution of large scale eigenvalue problems by implicitly restarted arnoldi methods.

Liñán, A., Martínez-Ruiz, D., Vera, M. & Sánchez, A.L. 2016 The large-activation-energy analysis of extinction of counterflow diffusion flames with non-unity lewis numbers of the fuel. *Combust. Flame* **175**, 91–106.

Liñán, A., Vera, M. & Sánchez, A. L. 2015 Ignition, liftoff, and extinction of gaseous diffusion flames. *Annu. Rev. Fluid Mech.* **47**, 293–314.

Ma, T.G. & Quintiere, J.G. 2003 Numerical simulation of axisymmetric fire plumes: accuracy and limitations. *Fire Safety J.* **38** (5), 467–492.

Malalasekera, W.M.G., Versteeg, H.K. & Gilchrist, K. 1996 A review of research and an experimental study on the pulsation of buoyant diffusion flames and pool fires. *Fire and materials* **20**, 261–271.

Marquet, O., Sipp, D. & Jacquin, L. 2008 Sensitivity analysis and passive control of cylinder flow. *J. Fluid Mech.* **615**, 221–252.

Mell, W.E., McGrattan, K.B. & Baum, H. 1996 Numerical simulation of combustion in fire plumes. *Symp. (Int.) Comb.* **26**, 1523–1530.

Moreno-Boza, D., Coenen, W., Sevilla, A., Carpio, J., Sánchez, A.L. & Liñan, A. 2016 Diffusion-flame flickering as a hydrodynamic global mode. *J. Fluid Mech.* **798**, 997–1014.

Most, J.M., Mandin, P., Chen, J., Joulain, P., Durox, D. & Fernández-Pello, A.C. 1996 Influence of gravity and pressure on pool fire-type diffusion flames. *Symp. (Int.) Combust.* **26**, 1311–1317.

Pagni, P.J. 1990 Pool fire vortex shedding frequencies. *Appl. Mech. Rev.* **43** (8), 153–170.

Prasad, K., Li, C., Kailasanath, K., Ndubizu, C., Ananth, R. & Tatem, P.A. 1999 Numerical modelling of methanol liquid pool fires. *Combust. Theor. Model.* **3**, 743–768.

Qadri, U.A., Chandler, G.J. & Juniper, M.P. 2015 Self-sustained hydrodynamic oscillations in lifted jet diffusion flames: origin and control. *J. Fluid Mech.* **775**, 201–222.

Reimann, J., Kuhlmann, S.-A. & Will, S. 2010 Investigations on soot formation in heptane jet diffusion flames by optical techniques. *Microgravity Sci. Technol.* **22** (4), 499–505.

Schmid, P.J. & Brandt, L. 2014 Analysis of fluid systems: Stability, receptivity, sensitivitylecture notes from the flow-nordita summer school on advanced instability methods for complex flows, stockholm, sweden, 2013. *Applied Mechanics Reviews* **66** (2), 024803.

Schönbucher, A., Brötz, W., Balluff, Ch., Riedel, G., Kettler, A. & Schiess, N. 1985 Visualization of organized structures in buoyant diffusion flames. *Ber. Bunsenges. Phys. Chem.* **89** (6), 595–603.

Sher, E. 1982 A theoretical study of the combustion of liquids at a free surface. *Combust. Flame.* **47**, 109–128.

Sibulkin, M. & Hansen, A.G. 1975 Experimental study of flame spreading over a horizontal fuel surface. *Combust. Sci. Tech.* **10**, 85–92.

Sinai, Y.L. 2000 Exploratory cfd modelling of pool fire instabilities without cross-wind. *Fire Safety J.* **35**, 51–61.

Smyth, K.C., Harrington, J.E., Johnsson, E.L. & Pitts, W.M. 1993 Greatly enhanced soot scattering in flickering ch_4/air diffusion flames. *Combust. Flame* **95**, 229–239.

Tieszen, S.R. 2001 On the fluid mechanics of fires. *Annu. Rev. Fluid Mech.* **33**, 67–92.

Tieszen, S.R., Nicolette, V.F., Gritzo, L.A., Holen, J.K., Murray, D. & Moya, J.L. 1996 Vortical structures in pool fires: observation, speculation, and simulation. *Tech. Rep.* SAND96-2607. Sandia National Laboratories.

Tohidi, A., Gollner, M.J. & Xiao, H. 2017 Fire whirls. *Annu. Rev. Fluid Mech.* (50), 187–213.

Toong, T.-Y., Salant, R. F., Stopford, J. M. & Anderson, G. Y. 1965 Mechanisms of combustion instability. *Proc. Combust. Inst.* **10**, 1301–1313.

Trefethen, L.N. & Embree, M. 2005 *Spectra and Pseudospectra: The Behavior of Nonnormal Matrices and Operators*. Princeton University Press.

Weckman, E.J. & Sobiesiak, A. 1988 The oscillatory behaviour of medium-scale pool fires. *Symp. (Int.) Combust.* **22**, 1299–1310.

Xiao, H., Gollner, M.J. & Oran, E.S. 2016 From fire whirls to blue whirls and combustion with reduced pollution. *Proc. Natl. Acad. Sci.* **113** (34), 9457–9462.

Yuan, T., Durox, D. & Villermaux, E. 1994 An analogue study for flame flickering. *Exp. Fluids* **17** (5), 337–349.

Zukoski, E., Cetegen, B. & Kubota, T. 1984 Visible structure of buoyant diffusion flames. *Symp. (Int.) Combust.* **20**, 361–366.

Part II

Effects of buoyancy on the slowly reacting mode of combustion of confined gaseous mixtures and its explosion limits

Brief overview

The seminal investigation of thermal explosions of confined reactive mixtures due to Frank-Kamenetskii is revisited in Chapter 3. He studied the "slowly reacting" mode of combustion and its thermal explosion limits of a reacting mixture undergoing an exothermic chemical reaction in a centrally symmetric closed vessel with constant wall temperature. In his analysis, an overall irreversible reaction with an Arrhenius rate having a large activation energy was employed, an appropriate model to represent the strong temperature dependence of the rate-controlling oxidation reactions in typical fuel-air mixtures. The analysis predicts a critical value Da_c of the controlling Damköhler number above which the slowly reacting mode of combustion no longer exists.

The extension of Frank-Kamenetskii's ideas to the case of buoyancy-dominated situations is presented in the subsequent chapters. The mathematical framework for the study of the slowly reacting mode of combustion accounting for buoyancy-induced motion, measured by a relevant Rayleigh number Ra, and the nonnegligible effect of the temporal pressure variations in enclosed environments is presented in Chapter 4. This is used in Chapter 5 to study the deviations in the thermal explosion limits in the limit $Ra \ll 1$ using asymptotic techniques. In Chapter 6, Frank-Kamenetskii explosion curves in the opposite limit $Ra \gg 1$ are determined over a wide range of Rayleigh numbers, wherein the flow remains laminar. Special attention is given to the boundary-layer structure of the flow, examined by means of an approximate integral method, providing an accurate prediction of the explosion limits.

The dissertation ends with the application of Frank-Kamenetskii's theory of thermal explosions to the reactive flow of a cold gaseous mixture in a pipe whose walls are kept at a greater constant temperature, where buoyancy effects are neglected. The evaluation of ignition distances for supercritical cases and downstream fuel consumption for subcritical cases is carried out by asymptotic methods and assessed by numerical computations.

Chapter 3

On Frank-Kamenetskii's analysis of thermal explosions

In this Chapter we revisit Frank-Kamenetskii's analysis of thermal explosions, using also a single-reaction model with an Arrhenius rate having a large activation energy, to describe the transient combustion of initially cold gaseous mixtures enclosed in a spherical vessel with a constant wall temperature. The analysis shows two modes of combustion, including a flameless slowly reacting mode for low wall temperatures or small vessel sizes, when the temperature rise due to the reaction is kept small by the heat-conduction losses to the wall, so as not to change significantly the order of magnitude of the reaction rate. In the second mode of combustion the slow reaction rates occur only in the first ignition stage, which ends abruptly when very large reaction rates cause a temperature runaway, or thermal explosion, at a well-defined ignition time and location, which triggers a flame that propagates across the vessel to consume rapidly the reactant. We define the explosion limits, in agreement with Frank-Kamenetskii's analysis, by the limiting conditions for existence of the slowly reacting mode of combustion. In this mode, a quasi-steady temperature distribution is established after a transient reaction stage with small reactant consumption. Most of the reactant is burnt, with nearly uniform mass fraction, in a second long stage, when the temperature follows a quasi-steady balance between the rates of heat conduction to the wall and of chemical heat release. The changes in the explosion limits due to the enhanced heat transfer rates by the buoyant motion are described in Chapters 5 and 6.

3.1 Introduction

Among many other important contributions to science, Frank-Kamenetskii is responsible for providing the basic understanding of the role of the strong temperature sensitivity of the

chemical heat release rate in the dynamics of combustion processes, and also for setting the foundations of the methods for the analysis of these processes taking advantage of the large value of the activation energy of the relevant controlling chemical reaction. Many of the key ideas were developed in connection with his "stationary theory of thermal explosions", published in 1939 (Frank-Kamenetskii, 1939), which deals with the explosion limits of reactive mixtures in vessels with constant wall temperature (Frank-Kamenetskii, 1955). These ideas were soon applied to other problems in combustion, notably by the Russian school led by Zel'dovich (Zel'dovich *et al.*, 1985). Especially noteworthy in this connection are Grisha Sivashinsky's contributions to flame dynamics and instability using in a masterful way large-activation-energy asymptotic techniques.

In this and in the following three chapters we revisit FK's analysis of the explosion limits, accounting for the effects of the initial conditions and the fuel consumption, when a reacting mixture is introduced in a rigid vessel and allowed to settle before the wall temperature is rapidly increased to a prescribed constant value. In Chapters 5 and 6, account is taken of the effects of buoyancy on the explosion limits.

As FK did in his seminal work (Frank-Kamenetskii, 1939), we model the chemical reaction as an irreversible global reaction with an Arrhenius rate, having a large activation energy to mimic the strong temperature dependence of the chemical heat release rate. Two different modes of combustion are encountered when the activation energy is moderately larger than the thermal energy at the wall temperature. For a fixed wall temperature, when the vessel size is smaller than a critical value the heat losses to the wall can limit the rise of the gas temperature in such a way that the reaction rate does not exceed in order of magnitude its near-wall value. This corresponds to a flameless slowly reacting mode of combustion that persists until the reactant is depleted. However, for vessel sizes larger than the critical value, we find a localized temperature runaway, at a well-defined thermal-explosion time, after an ignition stage with negligible changes of the reactant concentration; the location of the thermal explosion serves as origin for a thin premixed flame that propagates across the vessel consuming the reactant, with a significant temperature rise, at a rate considerably higher than that corresponding to the wall temperature.

Frank-Kamenetskii neglected the change in reactant concentration in his analysis of the thermal-explosion limits (Frank-Kamenetskii, 1939), defined as the critical conditions for existence of a steady mode of combustion. With the constant-density approximation used in the early work, heat transfer to the wall occurred only by conduction and, correspondingly, the temperature distribution was only dependent on the value of a Damköhler number Da, defined as the ratio of the time of heat conduction to the wall to the homogeneous thermal-explosion time. The curve giving the variation of the peak temperature with Da was found to exhibit a first turning point at a critical order-unity value Da_c of the Damköhler number, which identifies the explosion limit.

Centrally symmetric vessels were considered in the early analyses, including spheres, infinite cylinders, and infinite slab regions between two infinite flat walls (Frank-Kamenetskii, 1955; Zel'dovich *et al.*, 1985). The predictions of limiting vessel radii, or wall temperatures, based on the critical Damköhler number were found to be in close agreement with experimental observations; a truly notable achievement of the early theory, given the many different simplifying assumptions involved in its derivation (Frank-Kamenetskii, 1955).

Our focus will be on the slowly reacting mode of combustion, found for the subcritical cases $Da < Da_c$, to describe the initial heat-conduction and ignition-transient stage after the wall-temperature rise, which is followed by a long stage of slow reactant consumption, with a quasi-steady balance of conduction and heat release by the reaction. The transient analysis will also be carried out for the ignition stage of the supercritical cases $Da > Da_c$, which ends abruptly with a thermal runaway. We shall emphasize the role played in these transient stages by the time variations of the pressure in the confined environment of the vessel.

After this introduction § 3.1, we begin in § 3.2 by identifying the two chemical times that control the slowly reacting mode of combustion. Transient heating and reaction following the wall-temperature rise are investigated in § 3.4, where the case of chemically frozen heating is treated separately in section § 3.3. The quasi-steady FK temperature distribution is investigated in detail in § 3.5 and the results are used in § 3.6 to describe reactant consumption in the flameless combustion mode. Finally, concluding remarks are given in § 3.7. Effects of buoyancy on the slow-reaction mode, not yet considered here, are to be treated in the following chapters.

3.2 Relevant heat-release and fuel-consumption rates

As in the work of Frank-Kamenetskii (1939), we employ an overall Arrhenius reaction, of first order for simplicity in the presentation, with a rate given by

$$\dot{m}/\rho = YB\exp[-E/(RT)], \tag{3.1}$$

where $\dot{m}$ is the mass of reactant consumed per unit volume per unit time, which, when divided by the density ρ, is a function of the temperature T and of the reactant mass fraction Y. Here B is a frequency factor, E is the activation energy, and R is the universal gas constant. In this overall-reaction model the heat release rate of the reaction per unit volume is given by $q\dot{m}$, where q denotes the amount of heat released per unit mass of reactant consumed

An important realistic consideration of the FK analysis is that the activation energy E of the overall reaction is large compared with the thermal energy RT_o based on the wall temperature T_o; so that the nondimensional activation energy $\beta = E/(RT_o)$, a kinetic parameter, is large

compared with unity. Small temperature increments $T - T_o$, of the order of the Frank-Kamenetskii temperature $RT_o^2/E = T_o/\beta$, suffice to increase the reaction rate (3.1) by a factor of order unity, as can be seen by writing this factor in the form

$$\frac{B\exp[-E/(RT)]}{B\exp[-E/(RT_o)]} = \exp\left[\left(\frac{E}{RT_o}\right)\frac{(T-T_o)}{T}\right] = \exp\left(\frac{\phi}{1+\phi/\beta}\right) \tag{3.2}$$

in terms of the nondimensional temperature increase $\phi = \beta(T - T_o)/T_o$. This variable will be used below in the description of the slowly reacting mode of combustion, when ϕ maintains a value not large compared with unity. Then, for $\beta \gg 1$, the dependence on ϕ of the Arrhenius rate follows the FK approximation, $\exp[\phi/(1 + \phi/\beta)] \simeq \exp(\phi)$.

If the fuel consumption rate (3.1), evaluated at T_o with the initial fuel mass fraction Y_o, is maintained during most of the fuel-consumption time t_o, this would be given by

$$1/t_o = B\exp[-E/(RT_o)]. \tag{3.3}$$

However, a much smaller time t_e would be needed for the heat release rate of the reaction, given by $qY_oB\exp[-E/(RT_o)]$, to increase the enthalpy by an amount c_pT_o/β, proportional to the Frank-Kamenetskii temperature RT_o^2/E. Then t_e is given by

$$\frac{1}{t_e} = \frac{qY_o}{c_pT_o}\frac{E}{RT_o}B\exp[-E/(RT_o)], \tag{3.4}$$

where c_p is the specific heat at constant pressure, which for simplicity will be taken as constant. The ratio of both times is $t_o/t_e = \alpha\beta$, where the exothermicity parameter $\alpha = (qY_o)/(c_pT_o)$, of order or larger than unity, is the dimensionless temperature rise, based on T_o, for constant-pressure combustion.

For spatially uniform combustion at constant pressure, the self-acceleration of the chemical reaction results in a precipitous temperature rise—or thermal runaway—occurring at a finite explosion time. When, as shown in Zel'dovich *et al.* (1985), this time is calculated by equating the rates of enthalpy accumulation and heat release, after linearization for large β, of the Arrhenius exponent, we obtain, exactly, the estimated value t_e given in (3.4) [1]. Reactant consumption, measured by the parameter $\alpha\beta \gg 1$, has been neglected in the first approximation in this calculation because only a small fraction, of order $(Y_o - Y)/Y_o \sim t_e/t_o \sim 1/(\alpha\beta) \ll 1$, is consumed during the ignition stage.

[1] The explosion time for combustion at constant volume is also exactly equal to $t_e = t_o/(\alpha\beta)$ but with the specific heat at constant volume c_v replacing c_p when evaluating α

3.3 Heating of a cold gas mixture in a spherical vessel with suddenly increased wall temperature

We consider in this section the heating of a gas with initial temperature T_I, pressure p_I, and density ρ_I contained in a spherical vessel of radius a after the rapid increase of the vessel wall temperature to a value T_o, such that $T_o - T_I \sim T_o$, in a time small compared with the characteristic heat-conduction time across the vessel, $t_c = a^2/D_T$, where the thermal diffusivity D_T is evaluated with the density ρ_I and temperature T_o. Transient heating by heat conduction from the wall is accompanied by gas expansion, inducing a radial flow with characteristic velocities $v'_c = a/t_c = D_T/a$ dictated by the continuity equation

$$\frac{\partial \tilde{\rho}}{\partial t} + \frac{1}{r^2}\frac{\partial}{\partial r}(r^2 \tilde{\rho}\tilde{v}) = 0, \tag{3.5}$$

written in nondimensional form using t_c, a, v'_c, and ρ_I as scales for the time t, radial coordinate r, velocity $\tilde{v}$, and density $\tilde{\rho}$. Since the total mass contained in the vessel is constant, the mean density also remains constant, equal to its initial value according to

$$3\int_0^1 \tilde{\rho} r^2 \mathrm{d}r = 1, \tag{3.6}$$

obtained by radial integration of (3.5), after multiplication by r^2, subject to the condition of vanishing velocity at $r = 0$ and at $r = 1$, followed by integration in time of the resulting equation with initial condition $\tilde{\rho} = 1$ at $t = 0$.

The Peclet number $v'_c a/D_T$ associated with the characteristic gas-expansion velocity $v'_c = a/t_c = D_T/a$ is, as the Reynolds number, of order unity during the heating time, so that the convective transport and the molecular transport must be accounted for. The spatial pressure variations involved in the flow are of order $\Delta_s p \sim \rho_I v'^2_c$, as can be seen from the momentum balance equation, yielding $\Delta_s p/p_I \sim (a/t_c)^2/(p_I/\rho_I) \sim (\lambda_m/a)^2$, where $\lambda_m \sim D_T/(p_I/\rho_I)^{1/2}$ is the mean free path. Since in all cases of practical interest $\lambda_m \ll a$, the pressure remains nearly uniform during the heating process, although it increases with time as the gas is heated as dictated by the equation of state $(p/p_I) = (\rho/\rho_I)(T/T_I)$, to reach its asymptotic value $p_o = (T_o/T_I)p_I$ when the gas temperature grows to T_o and the density recovers its initial value ρ_I for large times.

The values of T_o and p_o can be used to define the dimensionless variables $\tilde{T}(r,t) = T/T_o$ and $\tilde{p}(t) = p/p_o$, reducing the energy equation to

$$\tilde{\rho}\left(\frac{\partial \tilde{T}}{\partial t} + \tilde{v}\frac{\partial \tilde{T}}{\partial r}\right) - \frac{\gamma - 1}{\gamma}\frac{\mathrm{d}\tilde{p}}{\mathrm{d}t} = \frac{1}{r^2}\frac{\partial}{\partial r}\left(r^2 \tilde{T}^{\sigma}\frac{\partial \tilde{T}}{\partial r}\right), \tag{3.7}$$

where $\gamma = c_p/c_v$ is the specific heat ratio and σ is the exponent for the presumed temperature dependence of the thermal conductivity. The term involving the pressure gradient has been omitted

in (3.7), as justified by the previous estimates. Since the viscous dissipation term can be estimated to be a factor $(\lambda_m/a)^2$ smaller than the enthalpy accumulation term, its contribution has also also been discarded when writing (3.7). The problem therefore reduces to that of integrating (3.5) and (3.7), supplemented with the equation of state

$$\tilde{p} = \tilde{\rho}\tilde{T}, \tag{3.8}$$

subject to the initial conditions $\tilde{\rho} - 1 = \tilde{T} - \tilde{T}_I = 0$ at $t = 0$ and the boundary conditions $\tilde{v} = \tilde{T} - 1 = 0$ at the constant-temperature wall surface $r = 1$ and $\tilde{v} = \partial\tilde{T}/\partial r = 0$ at the center $r = 0$, the latter needed for analyticity. As can be seen, for given values of γ and σ the solution depends only on $\tilde{T}_I = T_I/T_o$. For this centrally symmetric case, the momentum equation, not written here, is not needed to determine the evolution of $\tilde{T}$, $\tilde{p}$, $\tilde{\rho}$, and $\tilde{v}$; it could be used, a posteriori, to compute the small spatial variations of the pressure associated with the gas expansion.

The solution can be simplified by using (3.5) to write (3.7) in the conservative form

$$\frac{\partial}{\partial t}(\tilde{\rho}\tilde{T}) - \frac{\gamma - 1}{\gamma}\frac{\mathrm{d}\tilde{p}}{\mathrm{d}t} + \frac{1}{r^2}\frac{\partial}{\partial r}\left[r^2\left(\tilde{\rho}\tilde{v}\tilde{T} - \tilde{T}^\sigma\frac{\partial\tilde{T}}{\partial r}\right)\right] = 0. \tag{3.9}$$

Using the equation of state (3.8) to eliminate $\tilde{\rho}$ and integrating radially from the center yields

$$\tilde{p}\tilde{v} = \tilde{T}^\sigma\frac{\partial\tilde{T}}{\partial r} - \frac{r}{3\gamma}\frac{\mathrm{d}\tilde{p}}{\mathrm{d}t} \tag{3.10}$$

as an expression for the induced velocity $\tilde{v}$ in terms of $\tilde{T}$ and $\tilde{p}$. This last equation can be substituted into (3.5) to give

$$\tilde{p}\frac{\partial\tilde{T}}{\partial t} - \left[\frac{\gamma - 1}{\gamma}\tilde{T} + \frac{r}{3\gamma}\frac{\partial\tilde{T}}{\partial r}\right]\frac{\mathrm{d}\tilde{p}}{\mathrm{d}t} = \frac{\tilde{T}^2}{r^2}\frac{\partial}{\partial r}\left(r^2\tilde{T}^{\sigma-1}\frac{\partial\tilde{T}}{\partial r}\right) \tag{3.11}$$

for the evolution of the temperature, with the pressure evaluated from

$$\tilde{p} = \left(3\int_0^1 \frac{r^2}{\tilde{T}}\mathrm{d}r\right)^{-1} \tag{3.12}$$

obtained by using (3.8) in (3.6). Integrating (3.11) supplemented with (3.12) in $0 \le r < 1$ for $t > 0$ with initial condition $\tilde{T} = \tilde{T}_I$ at $t = 0$ and boundary conditions $\partial\tilde{T}/\partial r = 0$ at $r = 0$ and $\tilde{T} = 1$ at $r = 1$ determines the evolution of the temperature in the vessel.

Of interest for the ignition analysis given in § 3.4 are the small perturbations from the final equilibrium solution $\tilde{T} - 1 = \tilde{\rho} - 1 = \tilde{p} - 1 = \tilde{v} = 0$ encountered for large times, when the enthalpy equation (3.7), with negligible convective transport as a result of the small velocity, reduces to

$$\frac{\partial\Theta}{\partial t} - \frac{\gamma - 1}{\gamma}\frac{\mathrm{d}\bar{\Theta}}{\mathrm{d}t} = \frac{1}{r^2}\frac{\partial}{\partial r}\left(r^2\frac{\partial\Theta}{\partial r}\right), \tag{3.13}$$

involving the temperature perturbation $\Theta = \tilde{T} - 1 = (T - T_o)/T_o$. The temporal pressure variation has been written in (3.13) in terms of the average temperature $\bar{\Theta}$ by using

$$\tilde{p} - 1 = \bar{\Theta}(t) = 3 \int_0^1 (\tilde{T} - 1) r^2 \mathrm{d}r, \tag{3.14}$$

a result that follows from substitution of the linearized equation of state $\tilde{\rho} - 1 = (\tilde{p} - 1) - \Theta$ in (3.6).

Separation of variables in (3.13) yields solutions of the form $\Theta \propto [\sin(\lambda_n r)/(r \sin \lambda_n) - 1] \exp(-\lambda_n^2 t)$, where the eigenvalues λ_n are determined as the roots of the nonlinear equation

$$\frac{\tan \lambda_n}{\lambda_n} \left[\frac{\lambda_n^2}{3(\gamma - 1)} + 1 \right] = 1. \tag{3.15}$$

giving for instance $\lambda_n = (3.4478, 6.4618, 9.5482, \dots)$ for $\gamma = 1.4$. The term associated with the first eigenvalue $\lambda_1 = 3.4478$ becomes dominant for sufficiently large times, for which the solution to (3.7) simplifies to

$$\frac{T - T_o}{T_o} = -C \left[1 - \frac{\sin(\lambda_1 r)}{r \sin \lambda_1} \right] \exp(-\lambda_1^2 t), \tag{3.16}$$

where minus sign is added to emphasize that the temperature increases towards the wall value. The value of the positive constant $C(\tilde{T}_I)$, a function of $\tilde{T}_I$, must be determined from the numerical integration of (3.11) supplemented with (3.12).

3.4 Transient heating and reaction in rigid spherical vessels

The ignition stage ending with a thermal runaway is modified in non-homogeneous cases. For example, in the ideal realistic experiment analyzed below, the gas is introduced into a rigid spherical vessel, of radius a and wall temperature T_I, and allowed to settle to this temperature and a uniform density ρ_I. We shall consider that at this initial temperature the fuel-consumption time, given by (3.3) with T_o replaced by T_I, is too long, so that, in order to decrease it conveniently, we raise the wall temperature by an amount $T_o - T_I \sim T_I$ to a constant value T_o in a time short compared with the heat-conduction time across the vessel, which is of the order of $t_c = a^2/D_T$ in terms of the thermal diffusivity D_T evaluated with the density ρ_I and temperature T_o.

We shall analyze below the time evolution of the temperature and fuel concentration profiles, taking advantage of the simplifications associated with the realistic, moderately large values of the nondimensional activation energy β and its product $\alpha\beta$ with the exothermicity parameter α. Hence we can use an asymptotic analysis for large values of β and $\alpha\beta$, i.e. for

$$\frac{E}{RT_o} = \beta \gg 1 \quad \text{and} \quad \frac{qY_o}{c_p T_o} \frac{E}{RT_o} = \alpha\beta \gg 1, \tag{3.17}$$

and order-unity values of the Damköhler number Da, defined as the ratio t_c/t_e of the heat-conduction time to the explosion time, which we expect to be of order unity in the distinguished

regime

$$Da = \frac{t_c}{t_e} = \frac{a^2}{D_T}\frac{qY_o}{c_pT_o}\frac{E}{RT_o}\,B\exp[-E/(RT_o)] \sim 1 \tag{3.18}$$

of transition, at a well-defined value Da_c of Da, from the slowly reacting (subcritical) mode of combustion to the explosive mode for larger values of Da. In this distinguished regime we can expect to encounter variations in temperature from T_o of order T_o/β—or values of ϕ of order unity—everywhere across the vessel at the end of the transient stage, also scaled with the heat-conduction time, of heating of the gas from T_I to T_o.

3.4.1 Asymptotic analysis for the distinguished regime $\beta \gg 1$, $\alpha \sim 1$, and $Da \sim 1$.

Before formulating the problem, it is important to take into account that when combustion of a gas occurs in an unconfined environment, with velocities small compared with the sound velocity, even with variations of temperature of the order of the temperature itself, we can neglect the spatial changes in pressure in the equation of state, so that the changes in density are related to the changes in temperature and mean molecular mass. On the other hand, when combustion occurs in a rigid confined vessel, the changes of density are restricted to ensure that the mean spatial value of the density must keep its initial value, so that to ensure this important time variations of the pressure must be taken into account, additional to the much smaller spatial variations associated with the gas motion.

As indicated earlier, the critical vessel radius that defines, for a given wall temperature, the transition between the two different combustion modes described above can be determined, for large values of β, in the distinguished regime when α and Da are both of order unity. As a consequence of the exponential dependence with ϕ of the reaction rate, in this limiting case the heating of the mixture by heat conduction from the wall occurs in this first stage, scaled with t_c, without significant effects of the chemical reaction. This is so because in the reacting gas, outside a thin near-wall layer of characteristic thickness a/β, we find that the gas temperature is lower than the wall value by an amount $T_o - T \gg T_o/\beta$, so that the chemical reaction is effectively frozen. This is so even though nonnegligible reaction heat release occurs from the beginning in the thin near-wall layer where $T_o - T \sim T_o/\beta$. This heat does not affect significantly, for $Da \sim 1$, the rate of heat transfer from the wall to the cold gas. As a result, the reaction can be entirely neglected, as long as $-\phi \gg 1$ in most of the vessel, when studying the heating of the gas mixture for times of order t_c.

The description of the chemically frozen heating of the gas after the sudden rise of the wall temperature is given in section 3.3, where account is taken of the effects of the gas motion induced

by the local thermal expansion and of the temporal pressure variation in the enthalpy equation. Since the total mass contained in the vessel is constant, the mean density also remains constant, equal to its initial value ρ_I. At the end of the chemically frozen stage the gas thermodynamic variables approach the uniform values T_o and ρ_I (and $p_o = (T_o/T_I)p_I$, as related to the initial pressure p_I by the equation of state) with small variations that decrease exponentially with time with a scale $\lambda_1^2 t_c \sim t_c/12$.

This rapid exponential decay of the relative changes of T, ρ, and p from T_o, ρ_I, and p_o, is slowed down when $\phi = \beta(T - T_o)/T_o$ ceases to be negative and large, and the effects of the reaction then shape the reactive stage. The equation of state shows that the relative changes in T, of order β^{-1}, are accompanied by relative pressure and density changes from p_o and ρ_I, also of order β^{-1}. As a result, in the transient reactive stage, corresponding to the distinguished regime $Da \sim 1$ with $\beta \gg 1$, defining the transition between the slow reaction and the explosive mode of combustion, the appropriate nondimensional thermodynamic variables are given by

$$\phi = \beta(T - T_o)/T_o, \quad \hat{\rho} = \beta(\rho - \rho_I)/\rho_I, \quad \text{and} \quad \hat{p} = \beta(p - p_o)/p_o, \tag{3.19}$$

which, with errors of order β^{-1}, satisfy the linearized form

$$\phi + \hat{\rho} = \hat{p} \tag{3.20}$$

of the equation of state. These variables are to be determined in terms of the nondimensional time t, scaled with t_c, and the nondimensional radial coordinate r, scaled with the radius a.

As indicated above, the time variations in density from ρ_I, of order ρ_I/β during the time t_c, induce characteristic radial gas expansion velocities v_c, which, according to the continuity equation, are given by $v_c = \beta^{-1} a/t_c = \beta^{-1} D_T/a$. This results in a Peclet number for the induced motion $v_c a/D_T$ of order $\beta^{-1} \ll 1$, also the order of magnitude of the Reynolds number in this stage, while in the previous heating stage these numbers were of order unity, as explained in section 3.3. Therefore, the effects of the convective terms in the conservation equations can be neglected, in the first approximation for large β, during the slowly reacting stages.

The balance between the local flow acceleration and the pressure gradient in the momentum equation indicates that the spatial pressure variations needed to accelerate the flow are of order $\Delta_s p \sim \rho_I a v_c/t_c$. These spatial variations can be compared with the temporal pressure changes, of order p_o/β, to give $\Delta_s p/(p_o/\beta) \sim (a/t_c)^2/(p_o/\rho_I) \sim (\lambda_m/a)^2$, where $\lambda_m \sim D_T/(p_o/\rho_I)^{1/2}$ is the mean free path. The viscous dissipation term when compared with the enthalpy accumulation term is smaller than this ratio $(\lambda_m/a)^2$ by a factor $1/\beta$. The small value of the ratio $(\lambda_m/a)^2 \ll 1$ (required also to guarantee the validity of the continuum description), which is encountered in all cases of practical interest, allows us to neglect, with very small errors, the viscous-dissipation term

in the enthalpy equation, along with the spatial pressure variations, so as to consider $\hat{p}$ a function only of the time. Then we can integrate the linearized equation of state (3.20) from $r = 0$ to $r = 1$, after multiplication by $3r^2\mathrm{d}r$, and use the condition of constant total mass $3\int_0^1 r^2\hat{\rho}\mathrm{d}r = 0$ to give

$$\hat{p} = \bar{\phi} = 3\int_0^1 \phi r^2 \mathrm{d}r \tag{3.21}$$

for the evolution of the uniform pressure in the vessel, equal to the mean spatial average $\bar{\phi}(t)$ of the temperature increase $\phi(r,t)$.

The temperature and reactant mass fraction are then determined by the energy and reactant conservation equations, which in the distinguished regime $Da \sim 1$, $\beta \gg 1$, simplify to the form

$$\frac{\partial\phi}{\partial t} - \frac{\gamma-1}{\gamma}\frac{\mathrm{d}\bar{\phi}}{\mathrm{d}t} = \frac{1}{r^2}\frac{\partial}{\partial r}\left(r^2\frac{\partial\phi}{\partial r}\right) + Da\,\hat{Y}\mathrm{e}^{\phi} \tag{3.22}$$

$$\frac{\partial\hat{Y}}{\partial t} = \frac{1}{Le}\frac{1}{r^2}\frac{\partial}{\partial r}\left(r^2\frac{\partial\hat{Y}}{\partial r}\right) - \frac{1}{\beta\alpha}Da\,\hat{Y}\mathrm{e}^{\phi}, \tag{3.23}$$

if we are willing to accept errors of order $\beta^{-1} \ll 1$ when describing the evolution of $\hat{Y}$ and ϕ, as long as the latter remains of order unity. Here Da is the Damköhler number defined in (3.18), $\hat{Y} = Y/Y_o$ is reactant concentration normalized by its initial value, and $Le = D_T/D$ is the reactant Lewis number, the ratio of the thermal and molecular diffusivities, evaluated for the density ρ_I and temperature T_o. The temporal pressure variation has been written in (3.22) in terms of the average temperature (3.21), with the ratio of specific heats $\gamma = c_p/c_v$ appearing in the multiplying factor. The Frank-Kamenetskii linearization of the Arrhenius exponential $\exp[-E/(RT)] \simeq \mathrm{e}^{-\beta}\mathrm{e}^{\phi}$, following from (3.2) when $\beta \gg 1$ and $\phi \sim 1$, appears in the temperature dependence of the reaction rate, which is the only non-linear term in (3.22) and (3.23).

The description of the combustion process in the distinguished regime $Da \sim 1$, $\beta \gg 1$, is obtained—when we neglect terms, and thereby accept small errors, of order β^{-1}—by integrating (3.22) and (3.23) in the domain $0 \leq r < 1$, supplemented by (3.21), with boundary conditions for $t > 0$ given by $\phi = \partial\hat{Y}/\partial r = 0$ at $r = 1$, as corresponds to a non-reacting wall with constant temperature, and $\partial\phi/\partial r = \partial\hat{Y}/\partial r = 0$ at $r = 0$, needed to guarantee the analyticity of the solution.

The initial conditions to be considered in the integration depend on the magnitude of $(T_o - T_I)/T_o$. Thus when the initial gas temperature T_I is close to the wall temperature, i.e. for $T_o - T_I \ll T_o$, the simplifications leading to (3.22) and (3.23) hold also during the heating stage, so that one may start the integration, right after the wall temperature is raised, with the initial conditions

$$\phi = \phi_I \quad \text{and} \quad \hat{Y} = 1 \qquad \text{at} \quad t = 0, \tag{3.24}$$

involving the initial temperature $\phi_I = \beta(T_I - T_o)/T_o$. Notice that in this simplified formulation of the slowly reacting mode of combustion the parameters α and β appear only combined in a fuel-consumption parameter $1/(\alpha\beta) \ll 1$ as a factor of the reaction rate in (3.23).

Specific consideration of the initial heating stage is required for configurations with $T_o - T_I \sim T_o$. The initial conditions for integration of (3.22) and (3.23) are then obtained by matching with the solution found at the end of the chemically frozen heating stage, before significant chemical reaction has occurred. The initial value of the reactant mass fraction is simply $\hat{Y} = 1$, while the corresponding temperature distribution, determined in section 3.3, is given by

$$\frac{T - T_o}{T_o} = -C\left[1 - \frac{\sin(\lambda_1 r)}{r\sin\lambda_1}\right]\exp(-\lambda_1^2 t), \tag{3.25}$$

where $\lambda_1 \simeq 3.4478$ and C is a positive constant of order unity that depends on T_I/T_o. To facilitate the matching, it is convenient to write (3.22) and (3.23) in terms of the translated time $\hat{t} = t - t_{\rm R}$, where $t_{\rm R} \sim \ln(\beta)/\lambda_1^2$, defined from

$$C\exp(-\lambda_1^2 t_{\rm R}) = \beta^{-1}, \tag{3.26}$$

is the characteristic time at which the temperature drop $T_o - T$ shown in (3.25) decays to values of the order of the FK value T_o/β, small enough to enable the chemical reaction to proceed at a significant rate. Substituting (3.26) into (3.25) and expressing the result in terms of ϕ finally yields

$$\phi = -\left[1 - \frac{\sin(\lambda_1 r)}{r\sin\lambda_1}\right]\exp(-\lambda_1^2\hat{t}) \quad \text{and} \quad \hat{Y} = 1 \qquad \text{as} \quad \hat{t} \to -\infty, \tag{3.27}$$

as the initial conditions corresponding to values of $T_o - T_I \sim T_o$.

The problem of describing the combustion of the gaseous reactive mixture in the near-critical regime $Da \sim 1$, $\beta \gg 1$, has been reduced to the integration of (3.22) and (3.23)—in which the time has thus been scaled with the heat-conduction time t_c—with the initial and boundary conditions indicated above. A large parameter $\alpha\beta \gg 1$ is present in second of these equations, as a small factor $1/(\alpha\beta)$ in the fuel-consumption rate. Then, this equation allows us to conclude that for $t \sim 1$ the changes in $\hat{Y}$ from its initial value $\hat{Y} = 1$ are small, of order $1/(\alpha\beta)$, and can be neglected in this stage when solving (3.22). The factor $1/(\alpha\beta)$ plays an essential role in the fuel-consumption stage for both subcritical and supercritical combustion.

3.4.2 The first reaction stage

The chemical reaction begins to modify the temperature distribution after the non-reacting heating substage, changing the heat transfer from the wall from positive to negative. As indicated above, in the distinguished regime $Da \sim 1$, $\beta \gg 1$, the temperature evolution in this first reaction

stage can be determined, with small errors of order $1/(\alpha\beta)$, by integrating

$$\frac{\partial \phi}{\partial t} - \frac{\gamma - 1}{\gamma}\frac{\mathrm{d}\bar{\phi}}{\mathrm{d}t} = \frac{1}{r^2}\frac{\partial}{\partial r}\left(r^2 \frac{\partial \phi}{\partial r}\right) + Da\, \mathrm{e}^{\phi}, \tag{3.28}$$

involving the average value $\bar{\phi}$ given in (3.21), with boundary conditions $\phi = 0$ at $r = 1$ and $\partial\phi/\partial r = 0$ at $r = 0$ and initial conditions given either in (3.24) (when $\phi_I = (T_I - T_o) \sim T_o/\beta$) or in (3.27) (when $T_o - T_I \sim T_o$), with the translated time $\hat{t} = t - t_{\mathrm{R}}$ replacing t in the latter case. Results corresponding to both initial conditions are shown in Figs. 3.1 and 3.2 for several values of Da.

Figure 3.1 shows results corresponding to values of $T_o - T_I \sim T_o$. In the integrations, the initial temperature distribution (3.27) must be evaluated at a given negative value of $\hat{t}$. It was seen that, because of the strong exponential dependence present in (3.27) (note that $\lambda_1^2 \simeq 11.89$), for all values of Da tested in the integrations the results were independent of the selection of initial time provided that $\hat{t} \leq -0.05$, with the value $\hat{t} = -0.1$ employed in the computations of Fig. 3.1.

The figure shows, in particular, the variation with $\hat{t} = t - t_{\mathrm{R}}$ of the temperature at the vessel center $\phi_o = \phi(0, t)$ for selected values of Da. Since (3.27) is an exact solution of (3.28) for $Da = 0$, the evolution of ϕ_o for $Da \ll 1$ shows only small departures from the chemically frozen solution $\phi_o = -[1 - \lambda_1/\sin(\lambda_1)]\exp(-\lambda_1^2\hat{t}) \simeq -12.44\exp(-11.89\hat{t})$ obtained by evaluating (3.27) at $r \ll 1$.

The computations show that if Da is smaller than the critical value $Da_c \simeq 3.322$ the temperature evolves for moderately large values of $\hat{t}$ to approach the asymptotic steady distribution, given by the solution of the FK problem, representing the steady conduction-reaction balance,

$$\frac{1}{r^2}\frac{\partial}{\partial r}\left(r^2 \frac{\partial \phi}{\partial r}\right) + Da\, \mathrm{e}^{\phi} = 0, \tag{3.29}$$

subject to the boundary conditions $\partial\phi/\partial r = 0$ at $r = 0$ and $\phi = 0$ at $r = 1$. The resulting peak value ϕ_o, at $r = 0$, increases for increasing $Da < Da_c$ to approach the critical value $\phi_o \simeq 1.607$ for $Da = Da_c$.

No steady solution if found for $Da > Da_c$. Instead, the transient stage ends with a thermal runaway at a finite ignition time $\hat{t}_i(Da)$, as corresponds to a thermal explosion, with $\hat{t}_i$ decreasing for increasing Da and $\hat{t}_i \to \infty$ for $Da \to Da_c$, as can be seen in the inset of Fig. 3.1.

The location of the thermal runaway depends on Da, as illustrated in the left-hand side plots of this figure. The numerical results show that for values of Da in the range $3.322 < Da \lesssim 13.42$ the thermal runaway occurs, with a rapidly shrinking core, at the center, as seen in the temperature profiles for $Da = 10$, whereas for $Da \gtrsim 13.42$ the thermal runaway occurs in an increasingly thinner reacting layer at an intermediate radius, not far from the wall, while the gas in the center is still cold, as shown for $Da = 40$. In both cases, the rapid increase of the temperature

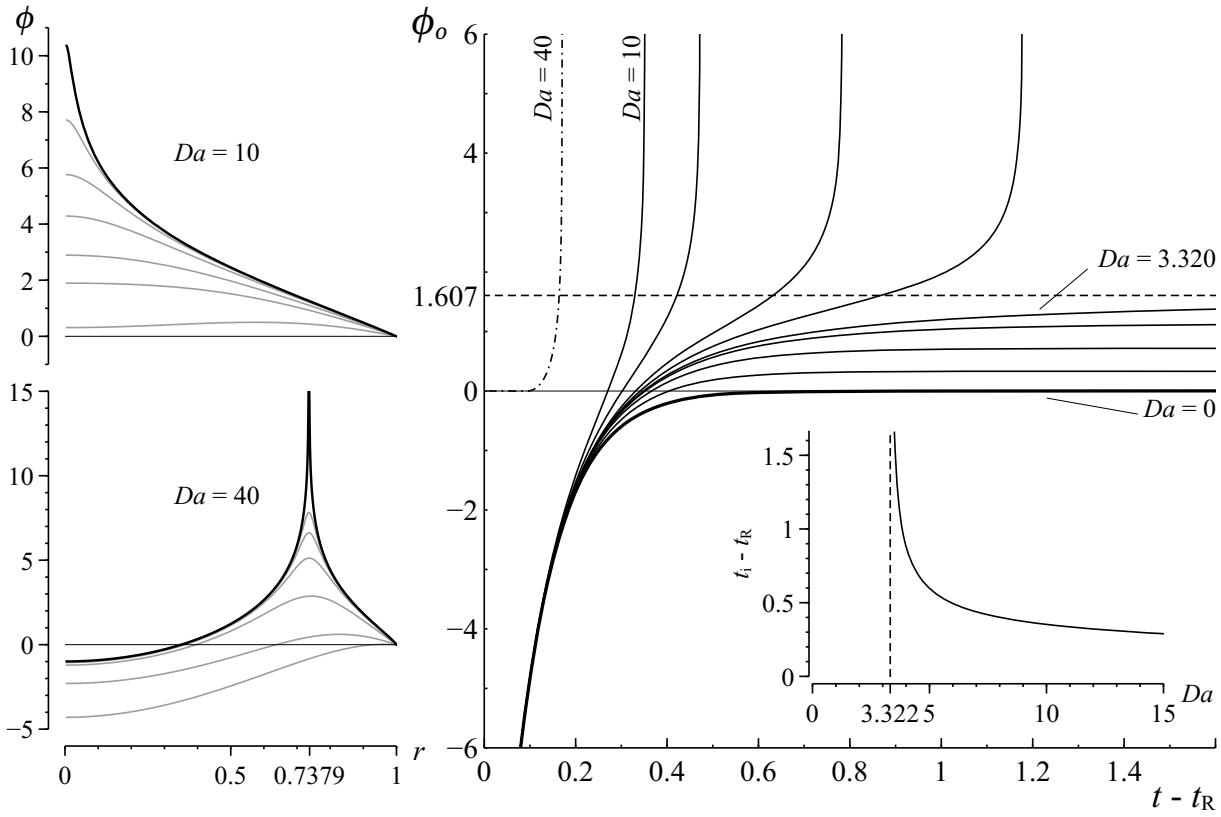

Figure 3.1: The growth with time of the temperature at the center of the vessel $\phi_o = \phi(0,t)$ for $Da = (1.58, 2.63, 3.15, 3.32, 3.68, 4.21, 6.32, 10)$ as obtained from integration of (3.28) with the initial temperature distribution given in (3.27). The thick curve $Da = 0$ represents the chemically frozen solution $\phi_o = -[1 - \lambda_1/\sin(\lambda_1)]\exp(-\lambda_1^2\hat{t})$ while the dot-dashed curve represents the evolution of the maximum temperature for $Da = 40$. The inset shows the variation of the explosion time $\hat{t}_i = t_i - t_{\rm R}$ with $Da > Da_c$. The left-hand side plots show radial temperature profiles for $Da = 10$ and $\hat{t} = (0.2857, 0.3343, 0.3348, 0.3495, 0.3508, 0.351068, 0.351114)$ and for $Da = 40$ and $\hat{t} = (0.1067, 0.1488, 0.1690, 0.1705, 0.170661, 0.170686, 0.170697)$.

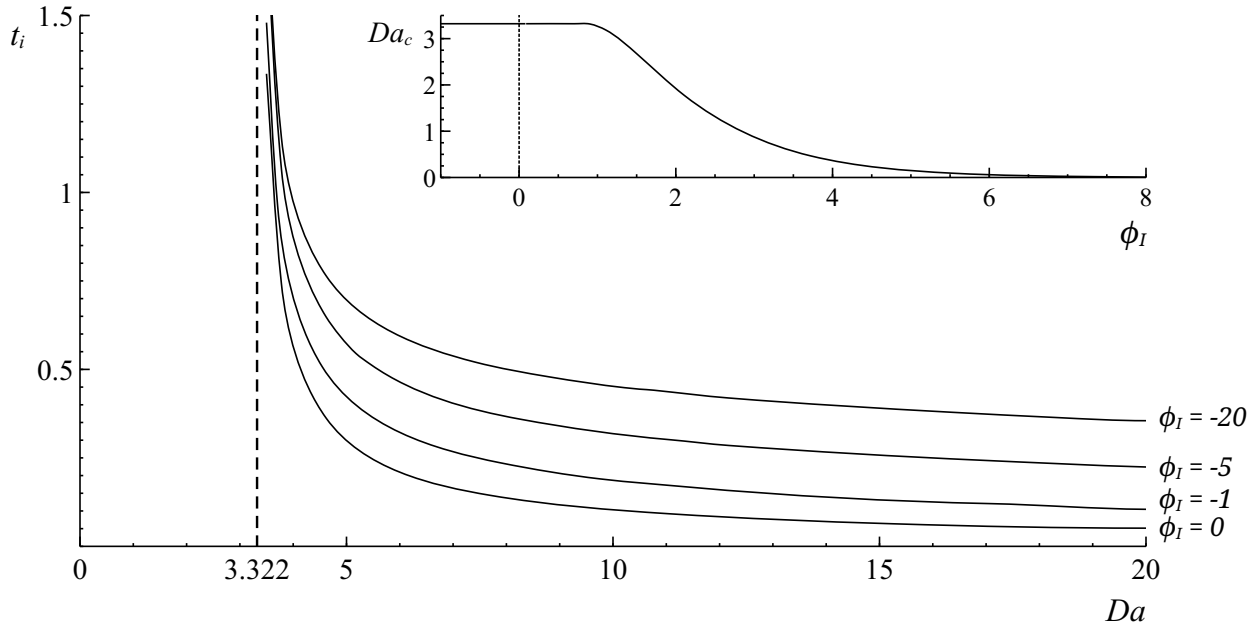

Figure 3.2: The variation of the ignition time t_i with Da for different values of $\phi_I \leq 0$ obtained from integrations of the ignition equation (3.28) with initial conditions (3.24); the inset shows the resulting variation of Da_c with ϕ_I.

occurs in a localized region, while the temperature profile outside remains approximately constant during the final development of the singularity when ϕ is growing to infinity. The ignition transient in Fig. 3.1 is represented by the evolution of the temperature at the center ϕ_o for $Da \leq 10$, while for $Da = 40$ it is represented by the time evolution of the maximum temperature with a dot-dashed curve.

Results corresponding to the effect of the initial temperature $\phi_I = (T_I - T_o)/(T_o/\beta) \sim 1$ are shown in Fig. 3.2. The plots show the variation of the ignition (or explosion) time t_i with $Da > Da_c$ for different values of ϕ_I, and exhibit the divergence as $Da \to Da_c$ identified before in Fig. 3.1. The value $Da_c \simeq 3.322$ for the critical Damköhler number found earlier is also encountered in these computations for all values of $\phi_I \leq 0$. The location of the thermal runaway depends on the Damköhler number. Thus for a given ϕ_I there exists a value of $Da(\phi_I) > Da_c$ below which the thermal runaway occurs at the center, whereas for larger value of Da the thermal runaway occurs at an intermediate radial location not far from the wall, giving corresponding temperature evolutions similar to those shown on the left-hand-side plots of Fig. 3.1.

The domain of attraction of the steady solution (3.29) was tested by considering in the computations also cases with $\phi_I > 0$. As can be seen in the inset of Fig. 3.2, even cases with moderately positive values $\phi_I \lesssim 1$ result in the same critical value $Da_c \simeq 3.322$, thereby further validating the applicability of the prediction $Da_c \simeq 3.322$.

When analyzing the ignition stage the changes in fuel mass fraction can be neglected before the thermal runaway leads to values of ϕ large compared with unity. The subsequent evolution of the hot kernel was analyzed by Dold (1985, 1989) to describe the generation of the premixed flame, with temperatures close to $\alpha\beta$, when scaled with the FK temperature. The analysis of Dold is applicable to the case $Da \lesssim 13.42$ when the hot-spot appears in the center, but not for larger Damköhler numbers, when the thermal runaway occurs with an increasingly thinner—and hotter—reaction layer, shrinking towards a surface, similar to that encountered by Liñán & Crespo (1976) in their ignition analysis in a mixing layer; who guessed that, after local depletion of the limiting component of the reactant mixture, two premixed flames were generated at the thermal-runaway surface to propagate across the mixture to burn the reactant.

3.4.3 Preliminary conclusions

The results presented above provide the explosion time as a function of T_I/T_o and Da. Heating from the wall and chemical reaction occur simultaneously when $(T_I - T_o) \sim T_o/\beta$, giving the ignition times shown in Fig. 3.2 as a function of the initial rescaled temperature $\phi_I = (T_I - T_o)/(T_o/\beta) \sim 1$ and Da. In contrast, when $T_o - T_I \sim T_o$, ignition is seen to proceed in two stages with associated durations that can be computed separately to give

$$t_i = t_{\mathrm{R}}(T_I/T_o) + \hat{t}_i(Da) \tag{3.30}$$

where t_{R} is a function of T_I/T_o, determined from (3.26) with use of the values of C obtained as indicated in section 3.3 from analysis of the heating stage, and $\hat{t}_i$ is a function of Da, given in the inset of Fig. 3.1. Since $t_{\mathrm{R}} \sim \ln(\beta)/\lambda_1^2$, with $\lambda_1^2 = 11.89$, while $\hat{t}_i \sim 1$, both terms in (3.30) can be expected to be comparable for realistic values of β, except for near-critical cases with $Da - Da_c \ll 1$, when $\hat{t}_i \gg 1$ becomes the dominant term.

Our computations also show that the critical value of the Damköhler number defining the explosion limit is $Da_c \simeq 3.322$, independent of the initial temperature for all values of $T_I \leq T_o$. The value of Da_c can be determined from integrations of the transient equation (3.28) or, alternatively, from investigation of the existence of solutions to the weakly reactive steady equation (3.29), which neglects effects of reactant consumption during the preceding transient stage.

Our ignition study therefore demonstrates that the quantitative approach proposed by Frank-Kamenetskii in his seminal paper (Frank-Kamenetskii, 1939), based on the analysis of solutions to (3.29), provides the leading-order description for the explosion limits for large activation energies. The asymptotic analysis also reveals that the modifications to the critical Damköhler number resulting from effects of reactant consumption, not computed here, would be of order $(\beta\alpha)^{-1} \ll 1$, as the relative amount of reactant consumed $(Y_o - Y)/Y_o \sim 1/(\alpha\beta) \ll 1$ during the

transient stage, with characteristic time t_c. In this stage the heat transfer from the wall to the gas changes from positive to negative, thus making possible the quasi-steady Frank-Kamenetskii balance (3.29). For values of $Da \leq Da_c$, reactant consumption occurs in the flameless slow-reaction mode of combustion with a characteristic time of order $t_o \sim \alpha\beta t_e$. This second stage is to be considered in § 3.6, following the detailed analysis of the Frank-Kamenetskii temperature distribution given in § 3.5. Modifications to the quasi-steady temperature distribution resulting from buoyancy and their effect on the explosion limits are to be investigated in Chapters 5 and 6.

3.5 The Frank-Kamenetskii temperature distribution

As shown above, consideration of the steady reaction-conduction balance (3.29) determines the critical value Da_c that defines the explosion limits of combustible mixtures in spherical vessels. The associated FK problem, which determines the FK temperature distribution $\phi_{\rm FK}(r)$ for $Da \leq Da_c$, is repeated here for convenience

$$\frac{1}{r^2}(r^2\phi'_{\rm FK})' = -Da\,\mathrm{e}^{\phi_{\rm FK}}, \quad \phi'_{\rm FK}(0) = \phi_{\rm FK}(1) = 0, \tag{3.31}$$

where the prime denotes differentiation with respect to r, and the boundary conditions correspond to constant-zero-value of the FK temperature at the vessel surface and the analyticity condition, imposing $\phi'_{\rm FK} = 0$ at $r = 0$. Of particular interest is the peak temperature $\phi_o = \phi_{\rm FK}(0)$, a function $\phi_o(Da)$ of the Damköhler number.

Unlike the centrally symmetric planar and cylindrical cases, whose solutions can be written in explicit analytic form (Frank-Kamenetskii, 1955), the computation of the temperature distribution in spherical vessels requires numerical integration. The FK problem (3.31) has no solution for Da larger than a critical value $Da_c = 3.322$, because of a bending bifurcation leading to multiple solutions for $Da < Da_c$. Of these, it is known that only the solution corresponding to the lower branch of $\phi_o(Da)$ is stable. The value Da_c is thus associated with the explosion limit, because for larger values of Da a thermal runaway, with rapid local reactant consumption, occurs at $r = 0$ after an ignition time $t_i(Da)$, as previously mentioned.

As shown by Chambre (1952), the two-point boundary-value problem (3.31) can be reduced by an appropriate change of variables[2] to a problem arising in Astrophysics in the early description of the hydrostatic equilibrium of isothermal gas stars, under their own gravitation

[2]Introduction of the temperature drop $\lambda = \phi_o - \phi_{\rm FK}(r)$, defined in (3.36), along with the stretched coordinate ξ, defined by the relation $\xi^2 = r^2 Da\mathrm{e}^{\phi_o}$, reduces the energy equation (3.31) to $\xi^{-2}(\xi^2\lambda_\xi)_\xi = \mathrm{e}^{-\lambda}$, to be integrated with initial conditions $\lambda = \lambda_\xi = 0$, as required by the analyticity of the temperature distribution at $\xi = 0$. The problem, arising in Astrophysics (Chandrasekhar, 1939), was solved numerically (Chandrasekhar & Wares, 1949) to determine the so-called isothermal function $\lambda = \lambda(\xi)$. Note that $\xi = Da\mathrm{e}^{\phi_o}$ when ξ is evaluated at $r = 1$, where $\lambda = \phi_o$ because $\phi_{\rm FK} = 0$ there. Thus, the universal function $\lambda = \lambda(\xi)$ allows us to calculate directly $Da\mathrm{e}^{\phi_o} = \xi(\phi_o)$; the resulting function $Da(\phi_o)$ has a maximum $Da \simeq 3.322$ at $\phi_o \simeq 1.607$ (Chambre, 1952).

(Chandrasekhar, 1939); see also the discussion on pp. 158–161 of (Zel'dovich *et al.*, 1985). We shall show below how to use the invariance properties of the equation to provide directly $Da(\phi_o)$, which is the inverse of the curve $\phi_o(Da)$, suggesting a more convenient way to handle the multiplicity or non-existence of solutions to the FK problem. As seen later in Part 2 (Sánchez *et al.*, 2016), an advantage of this method is that it can be readily extended to describe in a systematic way the incipient effects of buoyancy for low Rayleigh numbers.

3.5.1 A phase-plane analysis of the FK problem

Equation (3.31) is invariant under the transformation group

$$\phi_{\rm FK} \to \phi_{\rm FK} + C_1 \qquad \text{and} \qquad r \to C_2 r, \tag{3.32}$$

when the constants C_1 and C_2 satisfy the relation $C_2^2 \mathrm{e}^{C_1} = 1$. Taking advantage of this invariance, we introduce as dependent variables

$$u = Da\, r^2 \mathrm{e}^{\phi_{\rm FK}} \qquad \text{and} \qquad w = -r\frac{\mathrm{d}\phi_{\rm FK}}{\mathrm{d}r}, \tag{3.33}$$

also invariant under the transformation group (3.32). Our choice is dictated by the consideration that at $r = 1$, where $\phi_{\rm FK} = 0$, $u = Da$ and $w = -\phi'_{\rm FK}(1) = -\phi'_w$ (the dimensionless heat loss rate from the gas to the wall, which will play an important role when describing the fuel-consumption stage), to be calculated in terms of Da. Using these alternative variables, the second-order equation (3.31) reduces to the autonomous system of equations

$$r\frac{\mathrm{d}u}{\mathrm{d}r} = (2-w)u \quad \text{and} \quad r\frac{\mathrm{d}w}{\mathrm{d}r} = u - w \tag{3.34}$$

to be integrated with the initial conditions

$$u = w = 0 \quad \text{at} \quad r = 0 \tag{3.35}$$

and the condition $\phi_{\rm FK}(1) = 0$. However, in order to handle the problem of non-existence or multiplicity of solutions of the FK problem it is more convenient to pose the problem as that of determining the Damköhler number, and also the temperature distribution, leading to a given, peak value ϕ_o of the temperature $\phi_{\rm FK}$ at $r = 0$. Therefore, we shall use as independent variable the temperature drop from its peak value at the center of the vessel

$$\lambda = \phi_o - \phi_{\rm FK}(r). \tag{3.36}$$

The relation $\mathrm{d}r/r = \mathrm{d}\lambda/w$ derived from (3.33), can be used to rewrite (3.34) and (3.35) in the alternative form

$$\frac{\mathrm{d}u}{\mathrm{d}\lambda} = \frac{(2-w)u}{w} \quad \text{and} \quad \frac{\mathrm{d}w}{\mathrm{d}\lambda} = \frac{u-w}{w}, \quad u = w = 0 \quad \text{at} \quad \lambda = 0, \tag{3.37}$$

more convenient to handle the singularity of (3.34) at $r = 0$.

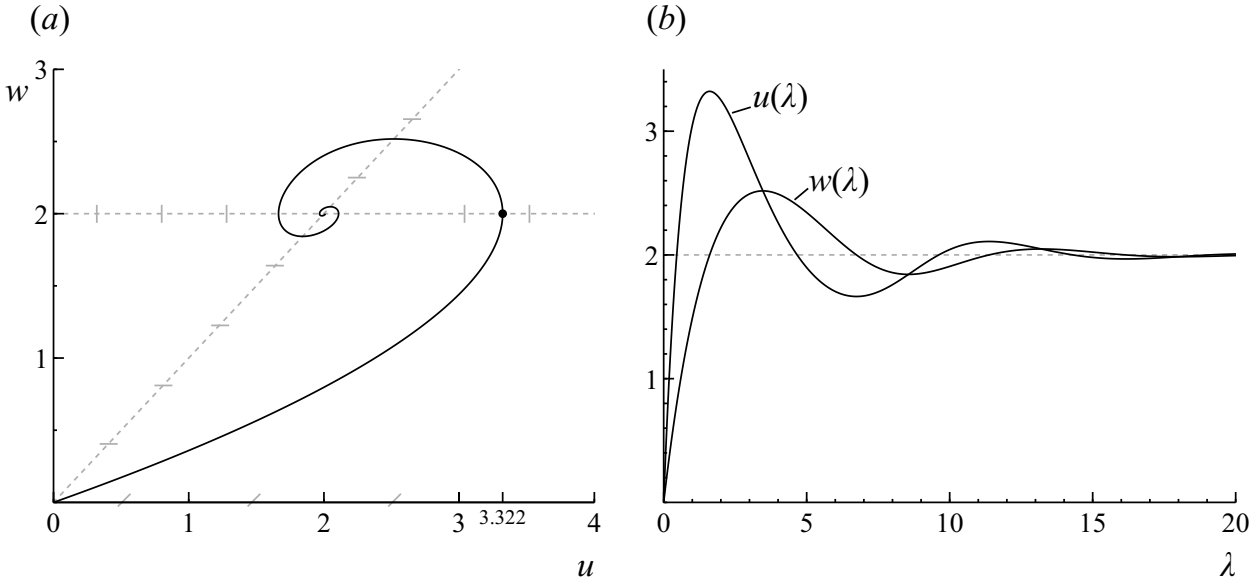

Figure 3.3: The universal FK functions $u(\lambda)$ and $w(\lambda)$ obtained by integration of (3.37).

3.5.2 The universal description of the temperature field

The system of equations (3.37) has the phase plane shown in Fig. 3.3(a), where we show some of the straight lines crossed by the trajectories with a constant slope, as given by the equations. There are two critical points on the phase plane, namely, the origin $u = w = 0$, a saddle point, and $u = w = 2$, a spiral point. The solution to (3.37) is the integral curve leaving the origin with $u = 3w$ as a separatrix that ends at the spiral point. The numerical integration of (3.37) starting with $u = 3w = 6\lambda$ for $\lambda \ll 1$ yields the universal functions $u(\lambda)$ and $w(\lambda)$ represented in Fig. 3.3(b).

These functions provide the solution to the original FK problem (3.31). This is so because they take the initial values $u = w = 0$ at $r = 0$, where $\lambda = 0$, and when λ grows to the value $\lambda = \phi_o$, when $r = 1$, u and w take the values $u = Da$ and $w = -\phi'_{\rm FK}(1) = -\phi'_w$. Therefore, the function $u(\lambda)$ provides directly $Da = u(\phi_o)$, whereas the function $w(\lambda)$ gives the variation of the reduced heat-loss rate to the wall $-\phi'_w = w(\phi_o)$.

The curves $u(\lambda)$ and $w(\lambda)$ display a non-monotonic behavior for increasing values of λ, with both curves oscillating about the spiral point $u = w = 2$ for $\lambda \gg 1$, and the asymptotic values $Da = 2$ and $-\phi'_w = 2$ for $\phi_o \gg 1$. This oscillating behavior, found by Steggerda (1965), is related to the existence of multiple branches of solutions to the FK problem (Frank-Kamenetskii, 1955; Zel'dovich *et al.*, 1985), with the first maximum of the curve $u(\lambda)$ corresponding to the first turning point of the classical explosion curve, associated with the well-known critical ignition conditions $Da = Da_c \simeq 3.322$ at $\phi_o \simeq 1.607$ indicated in Fig. 3.3. Only the solutions corresponding to the lower branch are stable and reached in the transient analysis given before in § 3.4.2. The solutions

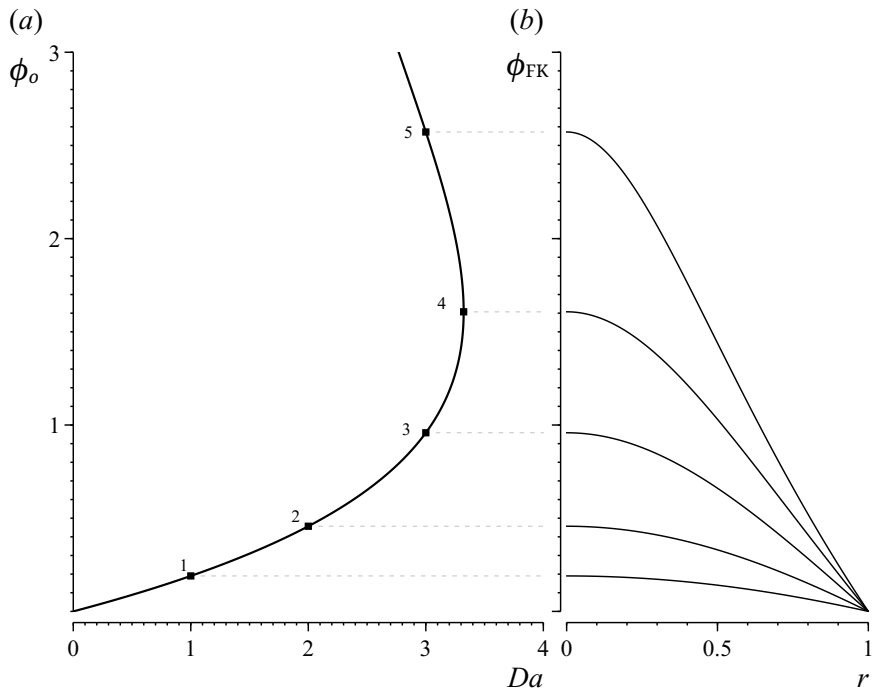

Figure 3.4: The radial temperature distribution $\phi_{\rm FK}(r)$ evaluated from (3.38) for the conditions corresponding to the five points indicated along the explosion curve $\phi_o(Da)$.

after the first turning point, for $\phi_o > 1.607$, are known to be unstable (Zel'dovich *et al.*, 1985). Once the value of ϕ_o associated with a given Da is identified as indicated above, the corresponding radial temperature distribution $\phi_{\rm FK}(r)$ can be obtained for $0 \le \lambda \le \phi_o$ with the parametric representation

$$\phi_{\rm FK} = \phi_o - \lambda \quad \text{and} \quad r^2 = \frac{u(\lambda)\mathrm{e}^{\lambda}}{Da\mathrm{e}^{\phi_o}}, \tag{3.38}$$

corresponding to the definitions of u and λ given in (3.33) and (3.36).

Figure 3.4 displays the resulting radial temperature distributions for five different points along the classical $Da(\phi_o)$ curve shown at the left, derived from the $u(\lambda)$ curve of Fig. 3.3. Besides the critical turning point of that curve, these points are for $Da = 1$ and for $Da = 2$ along the lower branch, as well as for the two indicated points at $Da = 3$, both below and above the turning point. The expected monotonic variations of these temperature profiles are evident. This figure serves to demonstrate explicitly the efficiency and utility of the approach to the analysis that has been developed here for the steady-state problem.

3.6 Flameless combustion

For subcritical values of the Damköhler number $Da \le Da_c$ the temperature in the vessel evolves towards the quasi-steady balance (3.29) in a transient stage with characteristic time t_e. Most

of the reactant consumption, small during the transient stage, occurs at times large compared with t_c, of order $t_o \sim \alpha\beta t_e$, such that the rescaled time $\tau = t/(\beta\alpha)$ is of order unity, when (3.22) and (3.23) become

$$\frac{1}{\beta\alpha}\left(\frac{\partial\phi}{\partial\tau} - \frac{\gamma-1}{\gamma}\frac{\mathrm{d}\bar{\phi}}{\mathrm{d}\tau}\right) = \frac{1}{r^2}\frac{\partial}{\partial r}\left(r^2\frac{\partial\phi}{\partial r}\right) + Da\,\hat{Y}\mathrm{e}^{\phi} \tag{3.39}$$

$$\frac{\partial\hat{Y}}{\partial\tau} = \frac{\beta\alpha}{Le}\frac{1}{r^2}\frac{\partial}{\partial r}\left(r^2\frac{\partial\hat{Y}}{\partial r}\right) - Da\,\hat{Y}\mathrm{e}^{\phi} \tag{3.40}$$

to be solved with the boundary conditions given earlier. Equation (3.40) indicates that during this second stage diffusion of the reactant is so fast that its mass fraction remains spatially uniform at leading order, so that $\hat{Y} \simeq \bar{Y}(\tau)$ with errors of order $1/(\alpha\beta)$, while the temperature evolves in a quasi-steady manner as dictated by

$$\frac{1}{r^2}\frac{\partial}{\partial r}\left(r^2\frac{\partial\phi}{\partial r}\right) + Da\,\bar{Y}\mathrm{e}^{\phi} = 0, \tag{3.41}$$

the limiting form of (3.39) for $\beta\alpha \gg 1$.

Clearly, the results given in § 3.5 for the Frank-Kamenetskii problem (3.31) can be employed to evaluate the solution to (3.41) by simply replacing Da with the instantaneous Damköhler number $Da\,\bar{Y}$. In particular, the curve $u(\lambda)$ given in Fig. 3.3 provides the peak temperature $\phi_o(\tau)$ as a function of the normalized reactant mass fraction $\bar{Y}(\tau)$ according to $Da\,\bar{Y} = u(\phi_o)$.

The evolution of $\hat{Y}(\tau)$ is given by

$$\frac{\mathrm{d}\bar{Y}}{\mathrm{d}\tau} = -3\int_0^1 Da\,\bar{Y}\mathrm{e}^{\phi}r^2\mathrm{d}r, \qquad \bar{Y}(0) = 1, \tag{3.42}$$

obtained by integrating (3.40) multiplied by r^2, with use made of the non-permeability condition $\partial\hat{Y}/\partial r = 0$ at $r = 1$. Since the energy balance is quasi-steady, the volume integral in (3.42), representing the overall rate of reactant consumption in the vessel, is proportional to the rate of heat transfer to the wall, as can be seen by using (3.41) to write (3.42) in the alternative form

$$\frac{1}{3}\frac{\mathrm{d}\bar{Y}}{\mathrm{d}\tau} = \int_0^1 \frac{\partial}{\partial r}\left(r^2\frac{\partial\phi}{\partial r}\right)\mathrm{d}r = \left(\frac{\partial\phi}{\partial r}\right)_{r=1}, \qquad \bar{Y}(0) = 1, \tag{3.43}$$

involving the reduced heat-loss rate to the wall $-(\partial\phi/\partial r)_{r=1} = -\phi'_w$, The value of $-\phi'_w$ can be evaluated in terms of $Da\,\bar{Y}$ by using $w = -\phi'_w$ and $Da\,\bar{Y} = u$ together with the curve $w(u)$ of Fig. 3.3, which can be used in (3.43) to yield

$$Da\,\tau = \frac{t}{\alpha\beta t_e} = \frac{1}{3}\int_{Da\,\bar{Y}}^{Da}\frac{\mathrm{d}u}{w(u)} \tag{3.44}$$

as an implicit representation for $\bar{Y}(\tau)$.

3.7 Concluding remarks

We have tried to show in this work how the asymptotic techniques based on the strong sensitivity with temperature of the combustion reactions, as reflected in the large activation energy of some of the controlling elementary reactions, are a useful tool to gain a good scientific understanding of combustion phenomena. We have considered a simple idealized experiment of the reaction of a gaseous mixture introduced in a spherical vessel whose wall temperature is raised to a final constant value T_o in order to initiate the Arrhenius reaction with large activation energy. We have tried to show how to identify the main parameters and the orders of magnitude of the variables that describe the main stages of the combustion process. For example, in this ideal experiment the initial temperature T_I and the wall temperature T_o are important parameters, along with the FK temperature RT_o^2/E and the flame temperature, the latter larger than the former by a factor $\alpha\beta$, where $\alpha = (qY_o)/(c_pT_o)$ is of order unity (or moderately larger than unity) and $\beta = E/(RT_o) \gg 1$. An important role is played by the frequency factor B of the Arrhenius reaction which defines a fuel-consumption time t_o, to be compared with the heat-conduction time t_c and the explosion time t_e, shorter than t_o by a factor $\alpha\beta$.

We have shown the important role played by the Damköhler number $Da = t_c/t_e$ in the evolution of the reactive mixture. In the distinguished regime $Da \sim 1$, $\beta \gg 1$, the reaction is chemically frozen in an initial stage of heating of the gas to temperatures that differ from T_o by an amount of the order of the FK temperature T_o/β. Then the reaction begins and the temperature and reactant concentration evolve with time as described by the simplified equations (3.22) and (3.23), when we accept small errors of order $1/\beta$, not significant in this evolution. As shown in § 3.2, during the first reaction stage, characterized by the heat-conduction time, there is no significant change in the reactant concentration from its initial value. For $Da \leq Da_c$ this stage ends for times moderately larger than t_c with a steady distribution of temperature given by the FK conduction-reaction balance. FK defined the thermal explosion limits as the limiting condition for existence of solutions to his problem. For $Da > Da_c$ the slowly reacting first stage ends with a local thermal runaway, which triggers a flame that propagates across the vessel, not analyzed here.

It is important to add that, although for simplicity our analysis was restricted to spherical vessels, the treatment can be generalized to non-symmetrical vessels, using (3.22) and (3.23) along with the linearized form of the continuity and momentum equations, with the latter including a term associated with the spatial variations of the pressure, which although small compared with p_o/β, play an important role in establishing the gas motion. It is also worth mentioning that the analysis presented here can be readily extended to determine explosion lengths and critical explosion radii of pipes carrying combustible gaseous mixtures, a problem analyzed later in Appendix A.

This chapter, in part, has been published in *Combustion Theory and Modelling*, "The slowly reacting mode of combustion of gaseous mixtures in spherical vessels. Part 1: Transient analysis and explosion limits", by A. Liñán, D. Moreno-Boza, I. Iglesias, A. L. Sánchez and F. A. Williams (2016) **20**(6), 1010-1028. The dissertation author is the primary investigator in this publication.

Bibliography

Chambre, PL 1952 On the solution of the poisson-boltzmann equation with application to the theory of thermal explosions. *The Journal of Chemical Physics* **20** (11), 1795–1797.

Chandrasekhar, S. 1939 *An introduction to the study of stellar structure*, , vol. 1. University of Chicago Press.

Chandrasekhar, S. & Wares, G. W. 1949 The isothermal function. *The Astrophysical Journal* **109**, 551–554.

Dold, J.W. 1985 Analysis of the early stage of thermal runaway. *Quart. J. Mech. Appl. Math.* **38** (3), 361–387.

Dold, J.W. 1989 Analysis of thermal runaway in the ignition process. *SIAM Journal on Applied Mathematics* **49** (2), 459–480.

Frank-Kamenetskii, D.A. 1939 The temperature distribution in a reaction vessel and the time-independent theory of thermal explosions. *Zh. Fiz. Khim.* **13**, 738–755.

Frank-Kamenetskii, D.A. 1955 *Diffusion and heat exchange in chemical kinetics*. Princeton University Press.

Liñán, A. & Crespo, A. 1976 An asymptotic analysis of unsteady diffusion flames for large activation energies. *Combust. Sci. Technol.* **14**, 95–117.

Sánchez, A.L., Iglesias, I., Moreno-Boza, D., Liñán, A. & Williams, F.A. 2016 The slowly reacting mode of combustion of gaseous mixtures in spherical vessels. part 2: Buoyancy-induced motion and its effect on the explosion limits. *Combust. Theory Modelling* **20** (6), 1029–1045.

Steggerda, JJ 1965 Thermal stability: An extension of frank-kamenetsky's theory. *The Journal of Chemical Physics* **43** (12), 4446–4448.

Zel'dovich, I.A., Barenblatt, G.I., Librovich, V.B. & Makhviladze, G.M. 1985 Mathematical theory of combustion and explosions. *Consultants Bureau, New York, NY* .

Chapter 4

The slowly reacting mode of combustion in spherical vessels: formulation accounting for buoyancy-induced motion

This Chapter serves as a presentation of the complete set of equations for the slowly reacting mode of combustion with natural convection, with account taken of the nonnegligible effect of the temporal pressure variations in the energy equation. As in Frank-Kamenetskii's seminal analysis, the strong temperature dependence of the effective overall reaction is modeled with a single irreversible reaction with an Arrhenius rate having a large activation energy. Besides the classical Damköhler number Da, measuring the ratio of the heat-release rate by chemical reaction evaluated at the wall temperature to the rate of heat removal by heat conduction to the wall, the solution is seen to depend on the Rayleigh number Ra, measuring the effect of buoyancy-induced motion on the heat-transport rate. For values of Da below a critical value Da_c the system evolves in a slowly reacting mode where the heat losses to the wall limit the temperature increase associated with the chemical reaction, whereas for $Da > Da_c$ the initial stage of slow reaction ends abruptly at a well-defined ignition time, at which a thermal runaway occurs.

Transient numerical integrations of the initial stage of slow reaction, formulated in the distinguished limit $Da \sim 1$ and $Ra \sim 1$ with account taken of the effects of the temporal pressure variation, will be used to investigate influences of natural convection on thermal-explosion development, including changes in ignition times for $Da > Da_c$ and modified explosion curves. Our analysis reveals that Frank-Kamenetskii's criterion for the determination of critical explosion

conditions, based on the investigation of existence of steady solutions, provides values of $Da_c(Ra)$ that are identical to those extracted from the transient computations.

4.1 Introduction

In developing the excellent stationary theory of thermal explosions, Frank-Kamenetskii (FK) investigated the role of the strong temperature sensitivity of the reaction rate in the combustion of enclosed reactive mixtures (Frank-Kamenetskii, 1939). Explosion limits were defined as the critical conditions for existence of a steady, slowly reacting mode of combustion in which the heat-conduction losses to the wall limit the temperature rise in such a way that the reaction rate does not exceed in order of magnitude its near-wall value. With the constant-density approximation used in the early work, heat transfer to the wall occurred only by conduction, its effect being measured by a Damköhler number Da, defined below in (4.2) as the ratio of the time of heat conduction to the wall to the homogeneous thermal-explosion time. The curve giving the variation of the peak temperature with Da exhibits a first turning point at a critical value $Da = Da_c$ of order unity (e.g., $Da_c = 3.32$ for spherical containers), which identifies the explosion limit in FK theory. Using the value of Da_c together with the definition of the Damkhöhler number leads to explicit expressions for critical explosion sizes, giving results in close agreement with experimental observations, a remarkable achievement of the early theory, given the many different simplifying assumptions involved in its derivation (Frank-Kamenetskii, 1955). This success has motivated recent extensions of the early theory incorporating realistic chemistry in descriptions of hydrogen-oxygen systems that have been shown to predict explosion conditions in spherical vessels in excellent agreement with experiments (Sánchez & Williams, 2014), including critical pressures along the so-called third-explosion limit (Sánchez *et al.*, 2014). The FK problem was recently revisited in (Liñán *et al.*, 2016) to investigate influences on ignition times of initial conditions and of temporal pressure variations in spherical vessels with fixed walls.

For gaseous mixtures under normal gravity the small temperature differences characterizing the slowly reacting mode of combustion are known to generate a convective motion that promotes heat transfer to the wall, measured by a relevant Rayleigh number Ra, defined below in (4.3). Influences of buoyancy on the resulting critical Damköhler numbers, discussed in early references (Frank-Kamenetskii, 1955), have been investigated numerically for simplified vessel geometries, as referenced below, including the infinite slab, the infinite horizontal cylinder, and the sphere, the last one being the configuration considered here.

The problem for a slab configuration, with a reactive gas bounded by two isothermal infinite horizontal walls, has been addressed in numerous theoretical analyses (Jones, 1973; Kolesnikov,

1992; Joulin *et al.*, 1996; Kagan *et al.*, 1997; Shtessel' *et al.*, 1971). As in the closely related case of the Rayleigh-Bénard problem of convection produced by wall-temperature differences, a motionless quasi-steady combustion mode may exist for values of the Rayleigh number below a critical value, at which a bifurcation occurs to a convective state, as described by linear stability analyses (Jones, 1973; Kolesnikov, 1992). A noteworthy feature of the slab geometry is that, contrary to widespread expectations, convection does not always hinder the development of the thermal explosion (Joulin *et al.*, 1996). While sufficiently small eddies with widths on the order of or smaller than the slab height raise the explosion threshold by enhancing heat removal from the reaction region, long-wave convection rolls favor explosions by promoting the formation of hot spots (Joulin *et al.*, 1996), an aspect of the problem further investigated in (Kagan *et al.*, 1997) with use made of a prescribed velocity field. The closely related problem of a horizontal cylindrical container of square section with adiabatic vertical walls has been also considered by different researchers (Merzhanov & Shtessel', 1973; Massot *et al.*, 2002; Belk & Volpert, 2004). For this geometry, the critical Damkhöhler number Da_c was found to increase in the presence of buoyancy-induced motion (Merzhanov & Shtessel', 1973). The rich nonlinear dynamics of weakly reactive solutions for subcritical values of the Damkhöhler number $Da < Da_c$ has now been investigated in more recent bifurcation analyses (Massot *et al.*, 2002; Belk & Volpert, 2004).

Unlike the horizontal infinite slab, for reactive gases in cylindrical and spherical vessels any gravity force at all establishes buoyant motion because the horizontal variations of the density that are present in these configurations generate forces that cannot be counteracted by a vertical pressure gradient. The case of a horizontal circular cylinder has been investigated both experimentally (Merzhanov & Shtessel', 1973) and numerically (Jones, 1974). This last work includes transient computations for Rayleigh numbers up to 10^4, for different initial temperatures both above and below the wall value. Influences of buoyancy on thermal explosions in spherical vessels have also been considered in the past. In connection with the present work, the most closely related investigations are the numerical computations of Hayhurst and coworkers (Campbell *et al.*, 2007; Liu *et al.*, 2008, 2010). To enable comparisons with previous experimental results (Archer, 1977) to be made, the thermal decomposition of azomethane vapor was considered in (Campbell *et al.*, 2007) when selecting the specific chemical-rate parameters, for values of the Rayleigh numbers up to 21900. Resulting values of Da_c were found to differ by only a few percent from those of the buoyancy-free predictions for values of Ra as large as a few hundred, in agreement with earlier results (Shtessel' *et al.*, 1971; Merzhanov & Shtessel', 1973; Jones, 1974). Larger values of the Rayleigh numbers were considered in subsequent direct numerical simulations (Liu *et al.*, 2008, 2010) addressing transient problems with the initial gas temperature equal to the vessel wall temperature. The flow was found to remain laminar for values of $Ra < 10^6$. More recent numerical

work by this same research group includes investigation of combined natural and forced convection on thermal explosions (Liu & Cardoso, 2013) as well as consideration of non-isothermal walls by use of a Robin condition including a heat-transfer coefficient (Campbell, 2015).

4.2 Conservation equations for the slowly reacting mode of combustion accounting for buoyancy-induced motion

4.2.1 Formulation for the transient near-explosion regime

Following (Liñán *et al.*, 2016), the reaction-rate expression selected is

$$\dot{m}/\rho = YB\exp[-E/(RT)], \tag{4.1}$$

where $\dot{m}$ is the mass of reactant consumed per unit volume per unit time, which, when divided by the density ρ, is a function of the temperature T and of the reactant mass fraction Y (variations of which were shown in (Liñán *et al.*, 2016) to be negligible), with B the frequency factor, E the activation energy, and R the universal gas constant; correspondingly, the heat-release rate per unit volume is $q\dot{m}$, where q denotes the amount of heat released per unit mass of reactant consumed. In terms of the wall temperature T_o, the nondimensional activation energy $\beta = E/(RT_o)$ again is the large parameter of expansion, with variations of the temperature from the wall value and of the density from its mean value ρ_{I} small, of order T_o/β and ρ_{I}/β, respectively, so that the non-dimensional temperature increase $\phi = \beta(T - T_o)/T_o$ is of order unity in this distinguished limit. Leaving out terms of order $1/\beta$ as before, departures of transport coefficients from their values evaluated for $T = T_o$ and $\rho = \rho_{\mathrm{I}}$ can be neglected. The principal non-dimensional parameters of the problem are the Damköhler number of order unity,

$$Da = \frac{a^2}{D_T}\frac{qY}{c_pT_o}\frac{E}{RT_o}B\exp[-E/(RT_o)], \tag{4.2}$$

where a is the radius of the sphere and D_T the thermal diffusivity, and the Rayleigh number (based on the ordering of the temperature difference),

$$Ra = \frac{\beta^{-1}ga^3}{\nu D_T}, \tag{4.3}$$

where g is the acceleration of gravity and ν the kinematic viscosity. This Rayleigh number measures the convective transport in the energy equation, while the Grashof number, Ra/Pr, involving the Prandtl number $Pr = \nu/D_T$, similarly measures convective transport in the momentum equation. The formultion is entirely non-dimensional, lengths being scaled with a and time with a^2/D_T.

Irrespective of the shape of the vessel, the equations describing the distributions of temperature and velocity of the reacting gas at the beginning of the transient reaction stage in the

distinguished near-explosion regime corresponding to the limit of large activation energies with fixed values of Da and Ra of order unity are the continuity, momentum, and energy conservation equations for the slowly reacting mode of combustion, which take the form

$$\nabla \cdot \boldsymbol{v} = 0, \tag{4.4}$$

$$\frac{1}{Pr}\left(\frac{\partial \boldsymbol{v}}{\partial t} + Ra\,\boldsymbol{v}\cdot\nabla\boldsymbol{v}\right) = \nabla^2\boldsymbol{v} - \nabla p' + \phi\,\boldsymbol{e}_z, \tag{4.5}$$

$$\frac{\partial \phi}{\partial t} - \frac{\gamma-1}{\gamma}\frac{\mathrm{d}\hat{p}}{\mathrm{d}t} + Ra\,\boldsymbol{v}\cdot\nabla\phi = \nabla^2\phi + Da\,\mathrm{e}^{\phi}, \tag{4.6}$$

in the non-dimensional variables. In the momentum equation (4.5), $\mathbf{e}_z$ is the unit vector pointing upwards (against gravity), and p' represents the pressure differences from the hydrostatic value scaled with $\rho_I g a/\beta$. The velocity vector $\mathbf{v}$ is scaled with the characteristic velocity $v_g = \beta^{-1} g a^2/\nu$, resulting from a balance between the viscous and buoyancy forces, associated with density variations of order ρ_I/β. Introduction of this characteristic velocity into the definition of Ra shows that this Rayleigh number also can be interpreted as a Peclet number, $v_g a/D_T$. In this near-explosion regime, associated with small density differences of order ρ_I/β, the contribution of the temporal density variation in mass conservation gives a higher-order correction, of order $(\beta Ra)^{-1}$, and therefore it does not appear in (4.4). In the equation for energy conservation, γ, denoting the specific-heat ratio, is present in the term arising from the time derivative of the pressure.

The spatial variations of the pressure p' appearing in (4.5) are small compared with the uniform temporal variation of the pressure from p_o, of order p_o/β, as given by $\hat{p} = \beta(p - p_o)/p_o$ of order unity, required by the equation of state, with $\hat{\rho} = \beta(\rho - \rho_o)/\rho_o$, to ensure, in its linearized form

$$\hat{\rho} + \phi = \hat{p}(t) \tag{4.7}$$

that the spatially mean density is ρ_I, thus leading to the relation

$$\hat{p} = \bar{\phi} \tag{4.8}$$

between $\hat{p}$ and the non-zero mean value $\bar{\phi}$ of the temperature.

The slowly reacting mode of combustion accounting for buoyancy-induced motion is expected to have analytical solutions of (4.4)–(4.6) inside the vessel with boundary conditions

$$\boldsymbol{v} = \phi = 0 \tag{4.9}$$

at the vessel walls. Computation of the transient evolution requires specification of the initial conditions. For instance, for a stagnant gas mixture at temperature T_I, with $T_o - T_I \sim T_o/\beta$, the conditions at the initial instant, when the wall temperature is raised to T_o, are simply given by

$$\boldsymbol{v} = \phi - \phi_I = 0 \quad \text{at} \quad t = 0, \tag{4.10}$$

where $\phi_I = \beta(T_I - T_o)/T_o < 0$. The analysis is somewhat more complicated when the wall-temperature rise is larger, such that $T_o - T_I \sim T_o$, in which case the heating of the gas by heat conduction from the wall, which proceeds initially with negligible chemical reaction, involves relative variations of the density, temperature, and pressure of order unity. The initial conditions for (4.4)–(4.6) then must be obtained by matching with the distributions of temperature and velocity found at the end of this chemically frozen heating period, similar to the discussion in (Liñán *et al.*, 2016).

As discussed in (Liñán *et al.*, 2016) for the buoyancy-free case $Ra = 0$, the transient evolution depends fundamentally on the Damköhler number. Thus if Da is smaller than a critical value $Da_c(Ra)$ the temperature and velocity evolve to approach a steady distribution for moderately large values of t, whereas for $Da > Da_c(Ra)$ the transient stage ends with a thermal runaway at a finite ignition time. The explosion limits can be obtained either by computing the transient problem or, as proposed by Frank-Kamenetskii, by investigating the existence of steady solutions, the latter being the quantitative approach pursued below for the specific case of a spherical vessel.

It may be worth mentioning here that, for subcritical values of $Da \leq Da_c(Ra)$, the above system of equations (4.4)–(4.6) can be used to describe the quasi-steady evolution of the temperature and velocity during the second much longer reactant-consumption stage occurring for $t \sim \alpha\beta \gg 1$, where $\alpha = (qY_o)/(c_pT_o)$. As explained in (Liñán *et al.*, 2016), the reactant mass fraction in this stage is nearly uniform and appears only as a factor of Da, equal to its spatially mean value, which evolves on the time scale $t/(\alpha\beta)$ through the mean consumption rate.

4.2.2 Steady conservation equations in spherical vessels

For spherical vessels with axisymmetric flow, introduction of spherical coordinates with origin at the vessel center reduces the continuity equation (4.4) to

$$\frac{\partial}{\partial r}(r^2 \sin\theta\, v_r) + \frac{\partial}{\partial \theta}(r \sin\theta\, v_\theta) = 0, \tag{4.11}$$

where r is the radial distance and θ is the angle measured with respect to the vertical direction $\mathbf{e}_z$. Introducing the stream function ψ, such that

$$\frac{\partial \psi}{\partial \theta} = r^2 \sin\theta\, v_r \qquad \text{and} \qquad \frac{\partial \psi}{\partial r} = -r \sin\theta\, v_\theta, \tag{4.12}$$

reduces energy conservation (4.6) to

$$\frac{Ra}{r^2 \sin\theta}\left(\frac{\partial \psi}{\partial \theta}\frac{\partial \phi}{\partial r} - \frac{\partial \psi}{\partial r}\frac{\partial \phi}{\partial \theta}\right) = \frac{1}{r^2}\frac{\partial}{\partial r}\left(r^2 \frac{\partial \phi}{\partial r}\right) + \frac{1}{r^2 \sin\theta}\frac{\partial}{\partial \theta}\left(\sin\theta \frac{\partial \phi}{\partial \theta}\right) + Da\, \mathrm{e}^{\phi}. \tag{4.13}$$

The momentum equation can be written conveniently in terms of the vorticity, which is azimuthal, of magnitude ω, given in terms of the stream function by

$$-r \sin\theta\, \omega = \frac{\partial^2 \psi}{\partial r^2} + \frac{\sin\theta}{r^2}\frac{\partial}{\partial \theta}\left(\frac{1}{\sin\theta}\frac{\partial \psi}{\partial \theta}\right). \tag{4.14}$$

The vorticity distribution then is described by the equation

$$\frac{Ra/Pr}{r^2\sin\theta}\left(\frac{\partial\psi}{\partial\theta}\frac{\partial}{\partial r}-\frac{\partial\psi}{\partial r}\frac{\partial}{\partial\theta}+2\frac{\cos\theta}{\sin\theta}\frac{\partial\psi}{\partial r}-\frac{2}{r}\frac{\partial\psi}{\partial\theta}\right)(r\sin\theta\,\omega)=$$
$$\left[\frac{\partial^2}{\partial r^2}+\frac{\sin\theta}{r^2}\frac{\partial}{\partial\theta}\left(\frac{1}{\sin\theta}\frac{\partial}{\partial\theta}\right)\right](r\sin\theta\,\omega)-r\sin^2\theta\frac{\partial\phi}{\partial r}-\sin\theta\,\cos\theta\,\frac{\partial\phi}{\partial\theta}, \tag{4.15}$$

obtained by taking the curl of (4.5), where the temperature gradient serves as the source term. The boundary conditions for (4.13)–(4.15),

$$\psi=\frac{\partial\psi}{\partial r}=\phi=0\quad\text{at}\quad r=1\quad\text{for}\quad 0\le\theta\le\pi, \tag{4.16}$$

correspond to a vessel with an isothermal wall with non-slip flow. The solutions, bounded and symmetric with respect to the vertical axis of the sphere, must be analytical, so that additional boundary conditions are

$$\psi=\frac{\partial}{\partial\theta}\left(\frac{1}{\sin\theta}\frac{\partial\psi}{\partial\theta}\right)=\frac{\partial\phi}{\partial\theta}=0\quad\text{at}\quad\theta=0,\pi\quad\text{for}\quad 0\le r\le 1. \tag{4.17}$$

The integration of this set of partial differential equations will be seen to provide the thermal explosion limits of the slowly reacting mode of combustion with natural convection. The two separte limits of small $Ra\ll 1$ and strong $Ra\gg 1$ buoyancy effects will be addressed in Chapters 5 and 6, respectively, using asymptotic and numerical techniques.

This chapter, in part, has been published in *Combustion Theory and Modelling*, "The slowly reacting mode of combustion of gaseous mixtures in spherical vessels. Part 2: Buoyancy-induced motion and its effect on the explosion limits", by A. L. Sánchez, I. Iglesias, D. Moreno-Boza, A. Liñán and F. A. Williams (2016) **20**(6), 1029-1045. The dissertation author is the primary investigator in this publication.

Bibliography

Archer, W.H. 1977 Heat transfer mechanisms in exothermic reactions. PhD thesis, The University of Manchester.

Belk, M. & Volpert, V. 2004 Modeling of heat explosion with convection. *Chaos: An Interdisciplinary Journal of Nonlinear Science* **14** (2), 263–273.

Campbell, A.N. 2015 The effect of external heat transfer on thermal explosion in a spherical vessel with natural convection. *Phys. Chem. Chem. Phys.* **17** (26), 16894–16906.

Campbell, A.N., Cardoso, S.S.S. & Hayhurst, A.N. 2007 A comparison of measured temperatures with those calculated numerically and analytically for an exothermic chemical reaction inside a spherical batch reactor with natural convection. *Chem. Eng. Sci.* **62** (11), 3068–3082.

Frank-Kamenetskii, D.A. 1939 The temperature distribution in a reaction vessel and the time-independent theory of thermal explosions. *Zh. Fiz. Khim.* **13**, 738–755.

Frank-Kamenetskii, D.A. 1955 *Diffusion and heat exchange in chemical kinetics*. Princeton University Press.

Jones, D.R. 1973 The dynamic stability of confined, exothermically reacting fluids. *Int. J. Heat Mass Transfer* **16** (1), 157–167.

Jones, D.R. 1974 Convective effects in enclosed, exothermically reacting gases. *Int. J. Heat Mass Transfer* **17** (1), 11–21.

Joulin, G., Mikishev, A.B. & Sivashinsky, G.I. 1996 A Semenov–Rayleigh–Benard problem. Unpublished.

Kagan, L., Berestycki, H., Joulin, G. & Sivashinsky, G. 1997 The effect of stirring on the limits of thermal explosion. *Combust. Theory Modelling* **1** (1), 97–111.

Kolesnikov, A.K. 1992 Convective stability of the horizontal reacting liquid layer in the presence of various complicating factors. *Int. J. Heat Mass Transfer* **35** (5), 1091–1102.

Liñán, A., Moreno-Boza, D., Iglesias, I., Sánchez, A.L. & Williams, F.A. 2016 The slowly reacting mode of combustion of gaseous mixtures in spherical vessels. part 1: Transient analysis and explosion limits. *Combust. Theory Modelling* **20** (6), 1010–1028.

Liu, T.-Y., Campbell, A.N., Cardoso, S.S.S. & Hayhurst, A.N. 2008 Effects of natural convection on thermal explosion in a closed vessel. *Phys. Chem. Chem. Phys.* **10** (36), 5521–5530.

Liu, T.-Y., Campbell, A.N., Hayhurst, A.N. & Cardoso, S.S.S. 2010 On the occurrence of thermal explosion in a reacting gas: The effects of natural convection and consumption of reactant. *Combust. Flame* **157** (2), 230–239.

Liu, T.-Y. & Cardoso, S.S.S. 2013 Effects of combined natural and forced convection on thermal explosion in a spherical reactor. *Combust. Flame* **160** (1), 191–203.

Massot, M., Génieys, S., Dumont, T. & Volpert, V.A. 2002 Interaction of thermal explosion and natural convection: critical conditions and new oscillating regimes. *SIAM J. Appl. Math.* **63** (1), 351–372.

Merzhanov, A.G. & Shtessel', E.A. 1973 Free convection and thermal explosion in reactive systems. *Acta Astronaut.* **18**, 191–199.

Sánchez, A.L. & Williams, F. A. 2014 Recent advances in understanding of flammability characteristics of hydrogen. *Prog. Energy Combust. Sci.* **41**, 1–55.

Sánchez, A. L, Fernández-Tarrazo, E. & Williams, F. A 2014 The chemistry involved in the third explosion limit of h 2–o 2 mixtures. *Combust. Flame* **161** (1), 111–117.

Shtessel', E.A., Pribytkova, K.V. & Merzhanov, A.G. 1971 Numerical solution of the problem of a thermal explosion taking account of free convection. *Combust. Explos. Shock Waves* **7** (2), 137–146.

Chapter 5

The slowly reacting mode of combustion in spherical vessels: solution for small Rayleigh numbers

The influence of buoyancy on the critical ignition Damkhöhler number Da_c for small and moderate values of Ra is examined in this chapter by asymptotic methods. At leading order in the limit $Ra \ll 1$, the analysis reveals that the spherically symmetrical temperature field corresponding to the buoyancy-free FK solution is accompanied by a toroidal vortex, which may be called the Frank-Kamenetskii vortex, resulting from the balance between buoyancy and viscous forces. The modifications to the explosion curve, determined by extending the perturbation analysis to a higher order, are found to scale with Ra^2, but the numerical factors in the expansion for Da_c are extremely small, so that the corrections associated with buoyancy remain smaller than 10% even at $Ra = 300$.

5.1 The Frank-Kamenetskii vortex

The temperature distribution $\phi = \phi_{\rm FK}(r)$ obtained from the Frank-Kamenetskii problem

$$\frac{1}{r^2}(r^2\phi'_{\rm FK})' = -Da\,{\rm e}^{\phi_{\rm FK}}, \quad \phi'_{\rm FK}(0) = \phi_{\rm FK}(1) = 0, \tag{5.1}$$

corresponds to the leading term in the perturbation analysis for small Rayleigh numbers. As shown in the previous chapter, the solution can be determined most conveniently in terms of $u = Da\,r^2{\rm e}^{\phi_{\rm FK}}$ and $w = -r({\rm d}\phi_{\rm FK})/({\rm d}r)$ with the temperature drop from its peak value at the center of the vessel $\lambda = \phi_o - \phi_{\rm FK}(r)$ used as a new independent variable, such that

$$r^2 = \frac{u(\lambda){\rm e}^{\lambda}}{Da{\rm e}^{\phi_o}}. \tag{5.2}$$

The spherically symmetric temperature field $\phi = \phi_{\rm FK}(r)$ generates a convective flow with toroidal vorticity. This FK vortex, determined at leading order by the balance $\nabla^2\mathbf{v} - \nabla p' + \phi\mathbf{e}_z = 0$ between buoyancy and viscous forces, has a simple dependence on θ, given by

$$\omega_{\rm FK} = -\sin\theta\,\Gamma_{\rm FK}/r \quad \text{and} \quad \psi_{\rm FK} = \sin^2\theta\,F_{\rm FK}, \tag{5.3}$$

the latter implying

$$v_r = 2\cos\theta F_{\rm FK}/r^2 \quad \text{and} \quad v_\theta = -\sin\theta F'_{\rm FK}/r, \tag{5.4}$$

with the radial variations $\Gamma_{\rm FK}(r)$ and $F_{\rm FK}(r)$, to be determined below. Thus, (4.14) and (4.15), for $Ra = 0$, reduce to the ordinary differential equations

$$\Gamma''_{\rm FK} - \frac{2}{r^2}\Gamma_{\rm FK} = w \tag{5.5}$$

and

$$F''_{\rm FK} - \frac{2}{r^2}F_{\rm FK} = \Gamma_{\rm FK}, \tag{5.6}$$

to be integrated with the boundary conditions

$$|F_{\rm FK}(0)/r^2| \neq \infty \qquad \text{and} \qquad F_{\rm FK}(1) = F'_{\rm FK}(1) = 0, \tag{5.7}$$

resulting from the boundedness of the velocity at the center of the vessel and from the no-slip condition at the wall.

Similar to the approach taken in (Liñán *et al.*, 2016) when solving (5.1), it is convenient to employ as variables $\tilde\Gamma_{\rm FK} = \Gamma_{\rm FK}/r^2$ and $\tilde F_{\rm FK} = F_{\rm FK}/r^4$, invariant under the radial dilatation used when defining w, yielding the equations

$$r^2\tilde\Gamma''_{\rm FK} + 4r\tilde\Gamma'_{\rm FK} = w, \tag{5.8}$$

$$r^2\tilde F''_{\rm FK} + 8r\tilde F'_{\rm FK} + 10\tilde F_{\rm FK} = \tilde\Gamma_{\rm FK} \tag{5.9}$$

with boundary conditions

$$|r^2\tilde F_{\rm FK}(0)| \neq \infty \qquad \text{and} \qquad \tilde F_{\rm FK}(1) = \tilde F'_{\rm FK}(1) = 0. \tag{5.10}$$

The homogeneous equation associated with (5.8) has solutions proportional to $1/r^3$, which must be disregarded as incompatible with the boundedness condition stated in (5.10), because they would lead to solutions $\tilde F_{\rm FK} \propto 1/r^3$. Therefore, the general solution to (5.8) is of the form

$$\tilde\Gamma_{\rm FK} = \tilde\Gamma_o + \hat\Gamma_{\rm FK}(r), \tag{5.11}$$

where the constant $\tilde\Gamma_o$, to be determined later using the condition $\tilde F_{\rm FK}(1) = 0$, represents the value of $\tilde\Gamma_{\rm FK}$ at the center, and $\hat\Gamma_{\rm FK}$ is a particular solution satisfying $\hat\Gamma_{\rm FK}(0) = 0$. The latter can be

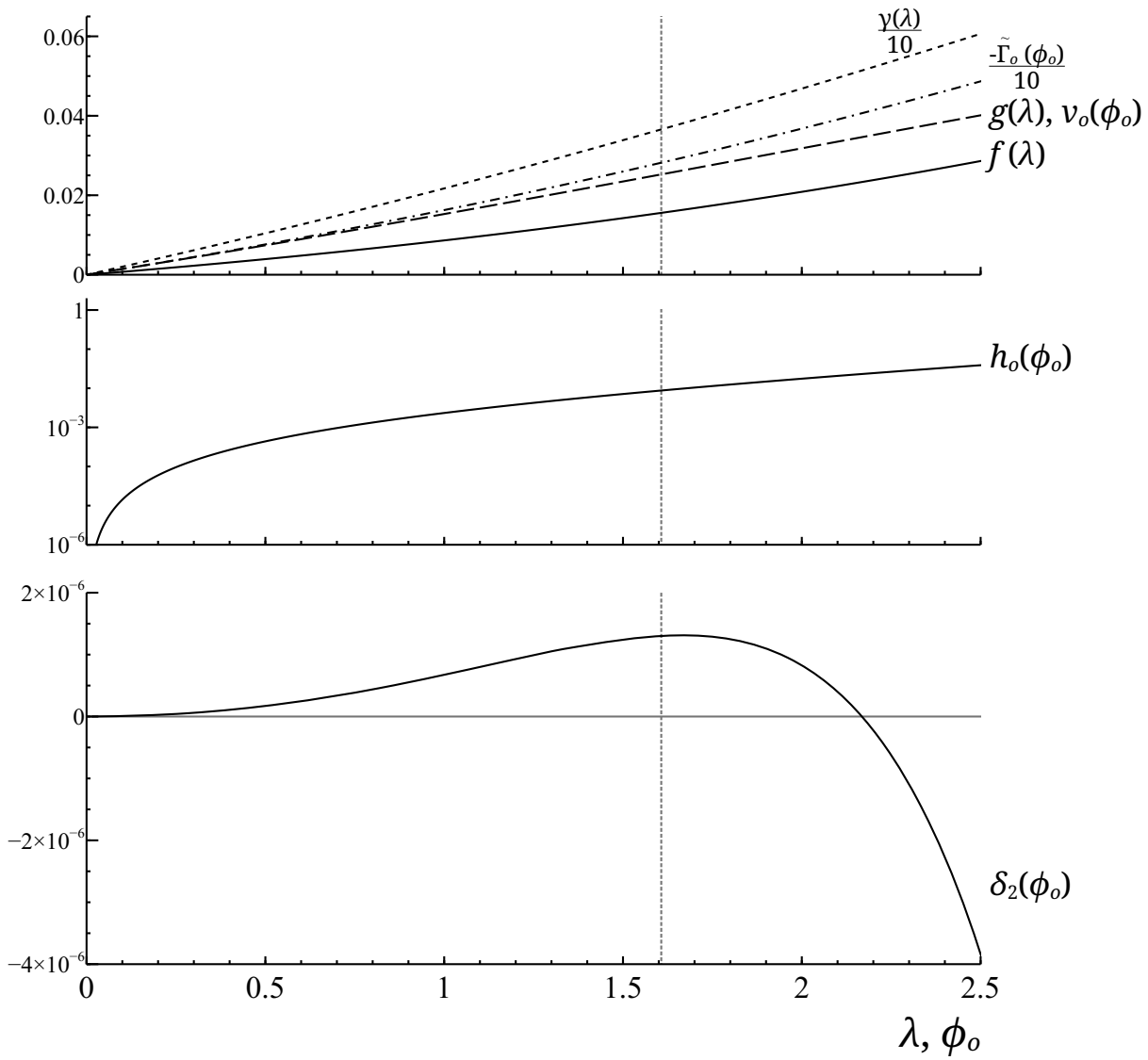

Figure 5.1: The upper plot shows the variation with λ of the functions γ and f obtained by integration of (5.12) and (5.14), respectively, and the accompanying constants $v_o(\phi_o)$ and $\tilde{\Gamma}_o(\phi_o)$ evaluated from (5.15). The lower plots show the variation of the temperature-perturbation gradient $h_o(\phi_o)$ evaluated from (5.29) along with the Damköhler-number correction $\delta_2(\phi_o)$ obtained from (5.35).

obtained by defining $\gamma(\lambda) = \hat{\Gamma}_{\text{FK}}(r)$ and $\sigma(\lambda) = r\hat{\Gamma}'_{\text{FK}}(r)$, with λ and r related by (5.2), and then writing (5.8) in the alternative form

$$\frac{\mathrm{d}\gamma}{\mathrm{d}\lambda} = \frac{\sigma}{w} \quad \text{and} \quad \frac{\mathrm{d}\sigma}{\mathrm{d}\lambda} = \frac{w - 3\sigma}{w}, \qquad \gamma(0) = \sigma(0) = 0. \tag{5.12}$$

The numerical integration with the behaviors $\gamma = \sigma/2 = \lambda/5$ and $w = 2\lambda$ for $\lambda \ll 1$ give results shown in Fig. 5.1, with other curves exhibited there to be derived and discussed later.

The analysis continues by discarding singular solutions of the form $\tilde{F}_{\text{FK}} \propto 1/r^5$ when solving the homogeneous problem associated with (5.9), so that the general solution for the stream

function reduces to

$$\tilde{F}_{\text{FK}} = \frac{v_o}{2r^2} + \frac{\tilde{\Gamma}_o}{10} + \hat{F}_{\text{FK}}, \tag{5.13}$$

where $\tilde{\Gamma}_o/10$ and $\hat{F}_{\text{FK}}(r)$ are the particular solutions associated with $\tilde{\Gamma}_o$ and $\hat{\Gamma}_{\text{FK}}$, respectively. The first term in (5.13), arising from the solution to the homogeneous problem, represents a uniform vertical velocity, as can be seen by using $F_{\text{FK}} = r^4\tilde{F}_{\text{FK}} = r^2 v_o/2$ to yield $v_r = v_o\cos\theta$ and $v_\theta = -v_o\sin\theta$. Since the other two terms in (5.13) give a vanishing velocity at $r = 0$, the constant v_o, to be determined below from the no-slip condition at the wall, turns out to be the velocity induced at the center, which is the peak velocity in the vessel.

The function $\hat{F}_{\text{FK}}$ can be determined by introducing $f(\lambda) = \hat{F}_{\text{FK}}(r)$ and $g(\lambda) = r\hat{F}'_{\text{FK}}(r)$ and integrating the autonomous problem

$$\frac{\mathrm{d}f}{\mathrm{d}\lambda} = \frac{g}{w} \quad \text{and} \quad \frac{\mathrm{d}g}{\mathrm{d}\lambda} = \frac{\gamma - 7g - 10f}{w}, \qquad f(0) = g(0) = 0, \tag{5.14}$$

obtained by rewriting (5.9) with λ replacing the radial coordinate. Since $\lambda = 0$ is a singular point, the numerical integration must be initiated using the approximations $2f = g = \lambda/70$ for $\lambda \ll 1$.

The functions $f(\lambda)$ and $g(\lambda)$, shown in Fig. 5.1, increase with λ and with the radial distance from the center, as dictated by (5.2). Their higher values at $\lambda = \phi_o$, corresponding to $r = 1$, are given by $f(\phi_o) = -(v_o/2 + \tilde{\Gamma}_o/10)$ and $g(\phi_o) = v_o$, as resulting from the boundary conditions $\tilde{F}_{\text{FK}}(1) = \tilde{F}'_{\text{FK}}(1) = 0$ and (5.13). Therefore, the functions $f(\lambda)$ and $g(\lambda)$ can be used to compute the variation with ϕ_o of

$$v_o = g(\phi_o) \quad \text{and} \quad -\frac{\tilde{\Gamma}_o}{10} = f(\phi_o) + \frac{1}{2}g(\phi_o), \tag{5.15}$$

given in Fig. 5.1. The range of values of λ, or ϕ_o, considered extends beyond the first turning point of the explosion diagram, associated with the value $\lambda = 1.607$, marked in Fig. 5.1 with a vertical dotted line.

Once the values of $\tilde{\Gamma}_o$ and v_o corresponding to a given Da are identified from Fig. 5.1 (complemented with the curve $Da(\phi_o)$ shown in Fig. 3.4), the functions $\gamma(\lambda)$ and $f(\lambda)$ can be used to obtain the functions

$$\Gamma_{\text{FK}}/r = r(\tilde{\Gamma}_o + \hat{\Gamma}_{\text{FK}}) \quad \text{and} \quad F_{\text{FK}} = r^4\left(\frac{v_o}{2r^2} + \frac{\tilde{\Gamma}_o}{10} + \hat{F}_{\text{FK}}\right), \tag{5.16}$$

with (5.2) employed to relate λ and r. The resulting profiles are shown in Fig. 5.2(b) for five different values of ϕ_o along the explosion curve of Fig. 5.2(a), including the critical turning point $\phi_o = 1.607$ (with $Da = 3.322$), the points $Da = 1$ and $Da = 2$ along the lower branch, and the points corresponding to $Da = 3$ both below and above the turning point. The curves in Fig. 5.2(a) for the three non-zero Rayleigh numbers are to be discussed later.

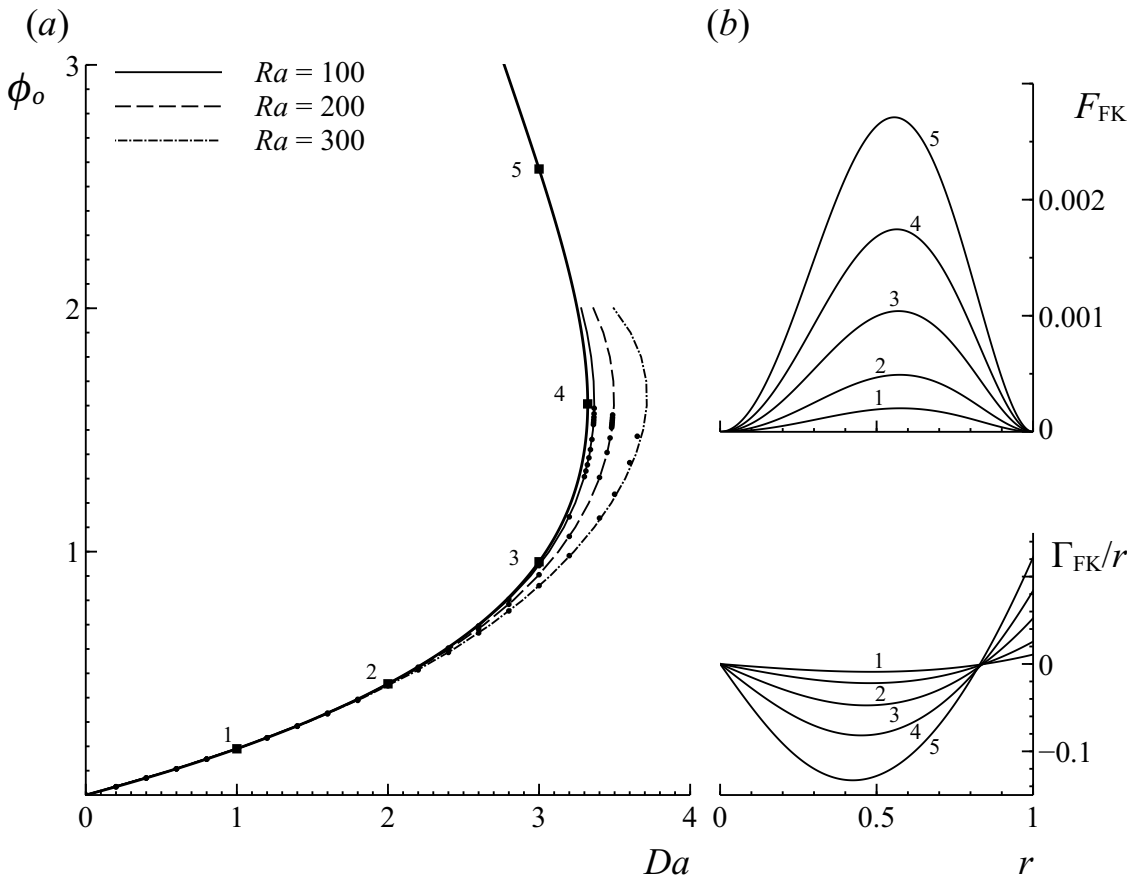

Figure 5.2: The functions $\Gamma_{\rm FK}/r$ and $F_{\rm FK}$ obtained from (5.16) for the conditions corresponding to the five points indicated along the FK explosion curve on the left-hand side, where the thin curves represent the Damköhler-number prediction obtained from (5.36) for $Ra = (100, 200, 300)$ and the small dots represent the variation of the temperature at the vessel center obtained by integration of (4.13)–(4.16) for different values of Da.

The results can be used to evaluate the vorticity and stream function given in (5.3), with sample streamlines and isovorticity lines given in Fig. 5.3 for the critical case $Da = Da_c = 3.322$. A distinctive quantitative feature of the solution is that, as a result of geometrical effects of the spherical vessel, the resulting nondimensional values of the peak velocity v_o, which are scaled with our original estimate $v_g = \beta^{-1} g a^2/\nu$ (resulting from the balance between viscous forces and buoyancy forces), are very small, of the order of 10^{-2}, as shown in Fig. 5.1. This unexpectedly slow motion has a weak effect on the temperature field through the convective transport of heat, leading to modifications of the explosion limits that remain small even for moderately large values of Ra of order 10^2, as found in numerical integrations of the original equations (Shtessel' *et al.*, 1971; Merzhanov & Shtessel', 1973; Jones, 1974).

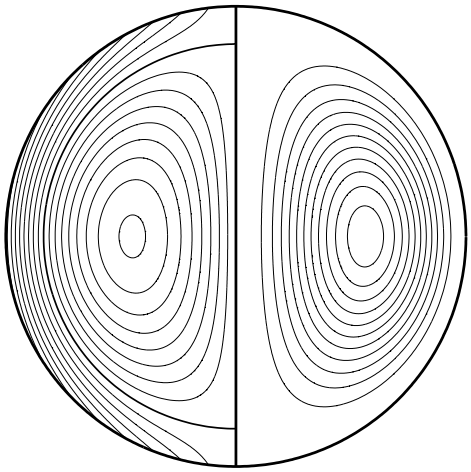

Figure 5.3: Streamlines and isocontours of vorticity for $Da = 3.322$ evaluated from (5.3) and (5.16). Increments of the streamfunction $\Delta\psi = 1.5\times10^{-4}$ are considered in plotting the streamlines, with a peak value $\psi = 0.001744$ at $r = 0.5648$ on the equatorial plane $\theta = \pi/2$. The vorticity isocontours are plotted in increments $\Delta\omega = 0.01$ from the zero value $\omega = 0$ found at the spherical surface $r = 0.8358$, vorticity being positive (negative) inside (outside).

5.2 Effect of convection on the critical ignition conditions

5.2.1 Perturbation scheme

The small deviations from the FK solution resulting from the presence of slow fluid motion for $Ra \ll 1$ can be addressed formally by expanding the different fluid variables in powers of Ra. The slow motion found at leading order, as represented by the small value $v_o \simeq 1/30$ for $\phi_o = 1.607$, is due to geometrical effects, not taken into account in the rough estimate $v_g = (g/\beta)(a^2/\nu)$ of the buoyant velocity. The resulting corrections to the explosion limits, although formally applicable only for small values of Ra, in fact become significant only for moderately large values of $Ra \sim 10^2$, and they remain accurate even for these large values, as occurs occasionally in perturbation expansions, although seldom ever to so great an extent.

Since the Rayleigh-number correction modifies the value of the critical Damköhler number above which FK solutions no longer exist, from its value at zero Rayleigh number, in the vicinity of the critical point, it is inconvenient to seek solutions for $\phi(r)$ by specifying Da. Instead, it is better to prescribe the temperature at the center of the vessel ϕ_o as known and then pose the problem as that of finding the perturbed Damköhler number Da that, for a given value of Ra, results in a temperature at the center of the vessel equal to ϕ_o. The monotonic variation of Da with ϕ_o, plotted in figure 4 of (Liñán *et al.*, 2016), shows that the leading-order solution exists for all values of ϕ_o, so that the problem is well-posed when formulated in this manner.

In order to calculate the dependence $Da(\phi_o, Ra)$ for fixed ϕ_o and small Ra, the expansions

$$Da = Da_{\rm FK}[1 + Ra\delta_1 + Ra^2\delta_2 + O(Ra^3)] \tag{5.17}$$

and

$$\begin{aligned} \phi - \phi_{\rm FK} &= Ra\phi_1 + Ra^2\phi_2 + O(Ra^3) \\ \omega - \omega_{\rm FK} &= Ra\omega_1 + Ra^2\omega_2 + O(Ra^3) \\ \psi - \psi_{\rm FK} &= Ra\psi_1 + Ra^2\psi_2 + O(Ra^3) \end{aligned} \tag{5.18}$$

are introduced. The terms in these expansions are determined by solving sequentially the different problems that arise at different orders in powers of Ra when (5.17) and (5.18) are introduced into (4.13)–(4.15), as indicated below, with the condition $\phi_j = 0$ applied at all orders $j = 1, 2, \ldots$ for the temperature perturbations from ϕ_o at the center $r = 0$. Although a term proportional to Ra is included in (5.17) for consistency with (5.18), it will be found that $\delta_1 = 0$, so that the corrections to the explosion curve $Da(\phi_o)$ are of order Ra^2; they will be seen to be important only for $Ra \sim 10^3$ because of the result that $\delta_2 \simeq 10^{-6}$.

5.2.2 First-order temperature perturbation

When the expansions (5.17) and (5.18) are used in (4.13), the terms of order Ra yield a linear equation for ϕ_1, to be integrated with boundary conditions $\phi_1 = 0$ at $r = 0$ and at $r = 1$. The resulting equation includes perturbations proportional to $\cos\theta$, arising from the convection term, along with perturbations independent of θ, that are proportional to the Damköhler-number perturbation δ_1, consistent with a perturbed temperature of the form $\phi_1 = \cos\theta H_1(r) + \mathcal{H}_1(r)$. The function $\mathcal{H}_1$, however, and its accompanying Damköhler-number perturbation δ_1, which are determined from the problem

$$r^2\mathcal{H}_1'' + 2r\mathcal{H}_1' + u(\mathcal{H}_1 + \delta_1) = 0, \quad \mathcal{H}_1(0) = \mathcal{H}_1(1) = 0, \tag{5.19}$$

derived from (4.13) and (4.16), must be identically zero. This can be seen readily by comparing the above equation with

$$r^2w'' + 2rw' + u(w - 2) = 0, \tag{5.20}$$

equivalent to the autonomous system giving u and w in terms of r in (22) of (Liñán *et al.*, 2016). Specifically, since $\mathcal{H}_1 + \delta_1$ and $w - 2$ satisfy the same second-order linear equation, the solution to (5.19) can be expressed in general as

$$\mathcal{H}_1 + \delta_1 = C_A\mathcal{Y}_A + C_B\mathcal{Y}_B, \tag{5.21}$$

involving two integration constants C_A and C_B and the two independent solutions

$$\mathcal{Y}_A = w - 2 \quad \text{and} \quad \mathcal{Y}_B = (w-2)\left(\int_0^r \frac{w(4-w)}{\hat{r}^2(w-2)^2}\mathrm{d}\hat{r} - \frac{1}{r}\right) \tag{5.22}$$

of (5.20). Because of the term $1/r$, the function $\mathcal{Y}_B$ is singular at the origin, so that the condition $\mathcal{H}_1(0) = 0$ requires that $C_B = 0$, and also determines the value $C_A = -\delta_1/2$, as follows from (5.21) with $\mathcal{H}_1(0) = 0$ and $\mathcal{Y}_A(0) = w(0) - 2 = -2$. The solution therefore reduces to $\mathcal{H}_1 = -\delta_1 w/2$. Since, however, w is positive for $r > 0$ (see Fig. 2 of (Liñán *et al.*, 2016)), the boundary condition $\mathcal{H}_1 = 0$ at $r = 1$ can be satisfied only if $\delta_1 = \mathcal{H}_1 = 0$. This completes the proof. With $\delta_1 = 0$, the perturbations to the Damköhler number emerge only at the following order in the expansion (5.17).

The resulting form of the temperature perturbation, $\phi_1 = \cos\theta H_1(r)$ indicates that at this order the presence of convection does not modify the mean temperature in the vessel, nor does it perturb the total heat-loss rate to the wall. Instead, the main effect of buoyancy is that of breaking the spherical symmetry of the problem, which was observed to be broken in previous numerical studies (Campbell *et al.*, 2007), causing the appearance of regions of hotter fluid in the upper half of the vessel and, correspondingly, regions of colder fluid in the lower half. The associated function H_1 is determined from the problem

$$\frac{H_1''}{r} + 2\frac{H_1'}{r^2} + (u-2)\frac{H_1}{r^3} = -2w\left(\frac{v_o/2}{r^2} + \frac{\tilde{\Gamma}_o}{10} + \hat{F}_{\mathrm{FK}}\right), \quad H_1(0) = H_1(1) = 0, \tag{5.23}$$

the solution to which is given in general by the sum of a linear combination of the solutions to the homogeneous problem and three particular solutions, associated with the three terms on the left-hand side of (5.23). As can be seen by inspection, in view of (5.20), the particular solution associated with v_o is given simply by $H_1 = -(2 - w/2)v_o r$. The other two particular solutions, associated with the terms involving $\tilde{\Gamma}_o$ and $\hat{F}_{\mathrm{FK}}$, can be expressed more conveniently in terms of alternative variables $\hat{H}_\Gamma$ and $\hat{H}_F$, defined from $H_1 = -(\tilde{\Gamma}_o/10)r^3\hat{H}_\Gamma$ and $H_1 = -r^3\hat{H}_F$, which are introduced to preserve the invariance of (5.23) under a radial dilatation. The general procedure followed above then leads in this case to the problems

$$\frac{\mathrm{d}h_\Gamma}{\mathrm{d}\lambda} = \frac{k_\Gamma}{w} \quad \text{and} \quad \frac{\mathrm{d}k_\Gamma}{\mathrm{d}\lambda} = -\frac{7k_\Gamma + (u+10)h_\Gamma - 2w}{w}, \qquad h_\Gamma(0) = k_\Gamma(0) = 0 \tag{5.24}$$

and

$$\frac{\mathrm{d}h_F}{\mathrm{d}\lambda} = \frac{k_F}{w} \quad \text{and} \quad \frac{\mathrm{d}k_F}{\mathrm{d}\lambda} = -\frac{7k_\Gamma + (u+10)h_\Gamma - 2wf}{w}, \qquad h_F(0) = k_F(0) = 0, \tag{5.25}$$

where $h_\Gamma(\lambda) = \hat{H}_\Gamma(r)$, $k_\Gamma(\lambda) = r\hat{H}_\Gamma'(r)$, $h_F(\lambda) = \hat{H}_F(r)$, and $k_F(\lambda) = r\hat{H}_F'(r)$, respectively. Near the origin, which is a singular point, the asymptotic behaviors $2h_\Gamma = k_\Gamma = 2\lambda/7$ and $4h_F = k_F = 2\lambda^2/945$ arise, which must be accommodated by the numerical solutions of (5.24) and (5.25).

The homogeneous equation associated with (5.23) admits diverging solutions $H_1 \propto r^{-2}$ near the origin, incompatible with the boundary condition $H_1(0) = 0$, along with linearly increasing solutions $H_1 \propto r$, which can be described more conveniently in terms of $H_1 = r\hat{H}_1$, where $\hat{H}_1(r)$ satisfies $r^2\hat{H}_1'' + 4r\hat{H}_1' + u\hat{H}_1 = 0$. The problem reduces to that of integrating, for $h(\lambda) = \hat{H}_1(r)$ and $k(\lambda) = r\hat{H}_1'(r)$, the equations

$$\frac{\mathrm{d}h}{\mathrm{d}\lambda} = \frac{k}{w} \quad \text{and} \quad \frac{\mathrm{d}k}{\mathrm{d}\lambda} = -\frac{3k + uh}{w} \tag{5.26}$$

with the boundary values near the origin evaluated from

$$h = 1 - \frac{3}{5}\lambda + \cdots \quad \text{and} \quad k = -\frac{6}{5}\lambda + \cdots \quad \text{at} \quad \lambda \ll 1, \tag{5.27}$$

the convenient normalization of h having been selected to be unity at $r = 0$.

The solution to (5.23), constructed by collecting the different contributions listed above, reads

$$H_1 = r\left[(h_o + 2v_o)\hat{H}_1 - \left(2 - \frac{w}{2}\right)v_o\right] - r^3\left(\frac{\tilde{\Gamma}_o}{10}\hat{H}_\Gamma + \hat{H}_F\right), \tag{5.28}$$

where the integration constant appearing as a factor of the homogeneous solution has been written in terms of $h_o = H_1'(0)$, the magnitude of the temperature gradient at the center. Its value can be evaluated for a given ϕ_o from

$$h_o = -2g(\phi_o) + \left(2 - \frac{w(\phi_o)}{2}\right)\frac{g(\phi_o)}{h(\phi_o)} - \left(f(\phi_o) + \frac{g(\phi_o)}{2}\right)\frac{h_\Gamma(\phi_o)}{h(\phi_o)} + \frac{h_F(\phi_o)}{h(\phi_o)}, \tag{5.29}$$

obtained by using the boundary condition $H_1 = 0$ at $r = 1$ in (5.28). As expected, the resulting value, plotted in Fig. 5.1, is found to be quantitatively small in the range of values of ϕ_o corresponding to the first turning point of the explosion curve.

5.2.3 Modified explosion curve

As discussed above, corrections to the Damköhler number emerge only at order Ra^2. The factor δ_2 in the expansion (5.17) is obtained from consideration of higher-order terms in the expansions (5.18). The vorticity and stream-function perturbations take the form

$$\omega_1 = -\sin\theta\cos\theta\,\Gamma_1/r \quad \text{and} \quad \psi_1 = \sin^2\theta\cos\theta\,F_1, \tag{5.30}$$

in terms of functions $\Gamma_1(r)$ and $F_1(r)$, as follows when collecting terms of order Ra in (4.14) and (4.15). Similarly, the temperature perturbation ϕ_2 can be seen from inspection of (4.13) to involve two different terms, according to $\phi_2 = \cos^2\theta\,H_2 + \mathcal{H}_2$. The functions $H_2(r)$ and $\mathcal{H}_2(r)$ satisfy

$$r^2H_2'' + 2rH_2' + (u-6)H_2 = 2F_{\mathrm{FK}}H_1' - F_{\mathrm{FK}}'H_1 - 3F_1w/r - \frac{1}{2}uH_1^2 \tag{5.31}$$

and

$$r^2\mathcal{H}_2'' + 2r\mathcal{H}_2' + u\mathcal{H}_2 = -\delta_2 u - 2H_2 + F_{\rm FK}'H_1 + F_1 w/r, \tag{5.32}$$

subject to $H_2(0) = H_2(1) = \mathcal{H}_2(0) = \mathcal{H}_2(1) = 0$.

The above homogeneous problem determines δ_2 as an eigenvalue. Although F_1 appears in both equations, the resulting value of δ_2 is independent of the corrections to the fluid motion (and, therefore, independent of the Prandtl number). This can be seen by considering

$$r^2(\mathcal{H}_2 + \tfrac{1}{3}H_2)'' + 2r(\mathcal{H}_2 + \tfrac{1}{3}H_2)' + u(\mathcal{H}_2 + \tfrac{1}{3}H_2 + \delta_2) = \mathcal{F}, \tag{5.33}$$

obtained from a linear combination of (5.31) and (5.32), with $\mathcal{F} = \frac{2}{3}(F_{\rm FK}H_1)' - \frac{1}{6}uH_1^2$. As can be inferred from (5.20), the general solution to (5.33) can be expressed in the form

$$\mathcal{H}_2 + \frac{1}{3}H_2 + \delta_2 = B_A\mathcal{Y}_A + B_B\mathcal{Y}_B + \tfrac{1}{4}\mathcal{Y}_B\int_0^r \mathcal{Y}_A\mathcal{F}\mathrm{d}r - \tfrac{1}{4}\mathcal{Y}_A\int_0^r \mathcal{Y}_B\mathcal{F}\mathrm{d}r, \tag{5.34}$$

involving the integration constants B_A and B_B and the independent solutions $\mathcal{Y}_A$ and $\mathcal{Y}_B$ of the homogenous equation, given in (5.22). Since the boundary conditions $\mathcal{H}_2(0) = H_2(0) = 0$ suffice to determine the value of the two integration constants $B_A = -\delta_2/2$ and $B_B = 0$, the additional boundary conditions $\mathcal{H}_2(1) = H_2(1) = 0$ require that

$$\begin{aligned}\delta_2 = \frac{(w-2)}{2w}\Bigg[\left(\int_0^1 \frac{w(4-w)}{r^2(w-2)^2}\mathrm{d}r - 1\right)\int_0^1 (w-2)\left[\tfrac{2}{3}(F_{\rm FK}H_1)' - \tfrac{1}{6}uH_1^2\right]\mathrm{d}r \\ - \int_0^1 (w-2)\left[\tfrac{2}{3}(F_{\rm FK}H_1)' - \tfrac{1}{6}uH_1^2\right]\left(\int_0^r \frac{w(4-w)}{\hat{r}^2(w-2)^2}\mathrm{d}\hat{r} - \frac{1}{r}\right)\mathrm{d}r\Bigg],\end{aligned} \tag{5.35}$$

obtained by evaluating (5.34) at $r = 1$. The resulting value of δ_2 is a function of ϕ_o, shown in Fig. 5.1.

The function $\delta_2(\phi_o)$ can be used to evaluate the modified explosion curve

$$Da = Da_{\rm FK}(1 + Ra^2\delta_2), \tag{5.36}$$

where $Da_{\rm FK}(\phi_o) = u(\phi_o)$, given by $u(\lambda)$ for $\lambda = \phi_o$. Because of the very small value $\delta_2 \sim 10^{-6}$ encountered in the perturbation analysis in powers of Ra, important perturbations in the critical Damköhler number occur only for values of the Rayleigh number of order 10^3. Considerations of (5.14), (5.24), and (5.25) suggest that the smallness of the factor $\delta_2 \sim 10^{-6}$ is a cumulative result of the sequence of ordinary differential equations, each with numerical coefficients of order 10, involved in its computation.

The accuracy of the prediction (5.36) is illustrated in Fig. 5.2(a), which includes comparisons with results of numerical integrations of the initial problem (4.13)–(4.16) for $Ra = 100$, 200, and 300, shown as points along the curves. The numerical procedure employed a pseudo-transient

method in seeking convergence to a steady solution, which prevented the branch of unstable solutions found beyond the first turning point from being accessible in the numerical integrations, so that the numerical results are limited to the lower branch of solutions extending from $Da = 0$ to $Da = Da_c$. Over the range that these numerical results are obtained, they differ negligibly from the results of the expansion, as may be seen by comparing the points with the thin curves in the figure. The corrections at the first non-vanishing order to the FK result for Da_c are seen to amount to less than ten percent even at $Ra = 300$. The range of the Rayleigh number over which the expansion remains valid thus is very large.

An unexpected peculiarity of the curve of δ_2 as a function of ϕ_o, shown in Fig. 5.1, is the attainment of a maximum, followed by a progression to negative values, beyond the turning-point value marked by the vertical line. These negative values imply that the motion of the fluid inside the sphere under those conditions, instead of decreasing the peak temperature by increasing the rate of heat loss to the boundary, tends on the average to insulate the central fluid from conductive heat loss, decreasing temperature gradients to the sides and bottom there, thereby increasing the peak temperature. Although reminiscent of the related effect in planar geometry mentioned earlier, the fluid-dynamic cause of this is quite different. Because the flow computed here in the region beyond the vertical line in the figure is unstable, however, this peculiarity would not be observed experimentally.

5.3 Concluding remarks

The present analysis has described effects of buoyancy on the slowly reacting mode of combustion in spherical vessels. The motion induced for small values of the Rayleigh number is an axisymmetric vortex—termed here the Frank-Kamenetskii vortex—that also exhibits symmetry about the equatorial plane, with positive vorticity generated in the central region by the finite-rate chemical heating but also with a region of negative vorticity near the wall, where the viscous retardation of the motion by the wall reverses the sign of the vorticity. At the leading order in the Rayleigh number, developed here, the zero-vorticity surface is perfectly spherical. At much higher Rayleigh numbers, this downward gas motion in the vicinity of the walls will generate a boundary layer there, growing with distance from the top, distorting the zero-vorticity sphere, so that the vortex tends to produce temperature stratification in the core, with hotter fluid in the upper portion of the sphere, as has been seen in numerical computations. The resulting modifications of the FK vortex may be expected to affect the criticality conditions for ignition, which motivates pursuit of associated boundary-layer analyses in the future.

Especially noteworthy of the present results is how remarkably small the fluid-flow influ-

ences associated with the Frank-Kamenertskii vortex are on the critical ignition Damköhler number (the value beyond which the slow-reaction types of solutions derived here no longer exist) . Despite the gas motion, the spatial variations average out in such a way that the overall effects remain small. This is not an asymptotic phenomenon; rather, it is a purely numerical influence of the small numerical coefficients arising in the expansions. For example, as may be seen in Fig. 5.1, even though the nondimensional flow velocities are roughly of order 10^{-2}, the nondimensional modification of the temperature gradient is only on the order of 10^{-3}, resulting in the change in the critical ignition Damköhler number, a second-order quantity, being only of order 10^{-6}, seen in the figure. Furthermore, while the leading-order corrections to the flow field of the Frank-Kamenertskii vortex do depend on the Prandtl number, even at the second order calculated here, the corrections to the critical ignition Damköhler number do not. This underscores the fact that the Rayleigh number, not the Grashof number, is the appropriate parameter of expansion.

This chapter, in part, has been published in *Combustion Theory and Modelling*, "The slowly reacting mode of combustion of gaseous mixtures in spherical vessels. Part 2: Buoyancy-induced motion and its effect on the explosion limits", by A. L. Sánchez, I. Iglesias, D. Moreno-Boza, A. Liñán and F. A. Williams (2016) **20**(6), 1029-1045. The dissertation author is the primary investigator in this publication.

Bibliography

Campbell, A.N., Cardoso, S.S.S. & Hayhurst, A.N. 2007 A comparison of measured temperatures with those calculated numerically and analytically for an exothermic chemical reaction inside a spherical batch reactor with natural convection. *Chem. Eng. Sci.* **62** (11), 3068–3082.

Jones, D.R. 1974 Convective effects in enclosed, exothermically reacting gases. *Int. J. Heat Mass Transfer* **17** (1), 11–21.

Liñán, A., Moreno-Boza, D., Iglesias, I., Sánchez, A.L. & Williams, F.A. 2016 The slowly reacting mode of combustion of gaseous mixtures in spherical vessels. part 1: Transient analysis and explosion limits. *Combust. Theory Modelling* **20** (6), 1010–1028.

Merzhanov, A.G. & Shtessel', E.A. 1973 Free convection and thermal explosion in reactive systems. *Acta Astronaut.* **18**, 191–199.

Shtessel', E.A., Pribytkova, K.V. & Merzhanov, A.G. 1971 Numerical solution of the problem of a thermal explosion taking account of free convection. *Combust. Explos. Shock Waves* **7** (2), 137–146.

Chapter 6

The slowly reacting mode of combustion in spherical vessels: solution for large Rayleigh numbers

Specific consideration is given in this chapter to the description of buoyancy effects for larger values of Ra, where results of relevant integrations are reported for values of the Rayleigh number up to $Ra = 7 \times 10^6$, thereby covering the entire range of flow conditions under which the flow may be expected to remain laminar. Besides numerical integrations, perturbation methods are used to investigate the flow structure that develops in the asymptotic limit $Ra \gg 1$, which is shown here to include a thin chemically frozen boundary layer driven by buoyancy, surrounding the vessel surface, and an inner chemically reacting inviscid region. The analysis at leading order provides the formulation of a boundary-value problem that determines the rescaled FK explosion curve, including the critical explosion conditions. The solution is obtained by an approximate method involving an integral form of the boundary-layer equations, which is found to produce predictions for the critical Damköhler number that compare favorably with the results of numerical integrations.

6.1 Selected numerical results

As previously mentioned, the evolution of the reactive flow in the vessel depends fundamentally on the Damkhöhler number. If Da is smaller than a critical value Da_c, larger for larger Ra, the temperature and velocity evolve to approach a steady distribution for moderately large values of t, whereas for $Da > Da_c$ the transient stage ends with a thermal runaway at a finite ignition

time. The determination of Da_c for a given Ra based on transient computations requires consideration of increasing values of Da until critical conditions are achieved, as was done previously in (Campbell *et al.*, 2007; Liu *et al.*, 2008, 2010). Alternatively, the explosion limit for a given Ra can be obtained directly by investigating the existence of steady solutions for the slowly reacting mode of combustion, with the value of Da_c corresponding to the turning point of the stationary explosion curve giving the variation of the peak temperature with Da, that being the criterion proposed in Frank-Kamenetskii's original theory. We shall see below that both computational approaches lead to predictions of explosion limits that are virtually identical.

6.1.1 FK analysis of thermal-explosion limits

We begin by considering steady FK solutions, described by integrating the steady version of (4.4)–(4.6) supplemented by (4.8) with the boundary conditions (4.9) at the vessel wall. A standard iterative root–finding technique (Newton–Raphson) is employed in the integrations. The linearized system of equations is solved using the software package FreeFem++ (Hecht, 2012), which employs finite elements for the spatial discretization. A summary of the steady solutions obtained for different values of Da and Ra is given in Fig. 6.1.

The upper plot in Fig. 6.1 shows explosion diagrams (i.e., curves representing the peak temperature $\phi_{\max}$ as a function of the Damköhler number Da) for six different values of the Rayleigh number, including the classical FK results corresponding to $Ra = 0$, for which the turning point occurs at $Da_{\rm FK} \simeq 3.32$ with $\phi_{\max} \simeq 1.61$ (Frank-Kamenetskii, 1955). Because of the enhanced heat transfer associated with the convective motion, the turning points of the resulting curves occur at larger values of Da_c for increasing Ra. This variation is represented in the intermediate plot of Figure 6.1. As expected from previous analyses, the departures $Da_c - Da_{\rm FK}$ of the critical Damköhler number from the buoyancy-free value $Da_{\rm FK}$ remain fairly small for values of Ra on the order of a few hundred. For these conditions of weak convective motion the asymptotic prediction $Da_c = Da_{\rm FK}(1 + \delta_2 Ra^2)$, derived previously in the limit $Ra \ll 1$ (Sánchez *et al.*, 2016), agrees well with the numerical results. The quantitative effect of buoyancy on the explosion boundary becomes clearly noticeable for $Ra \gtrsim 500$, for which the departures $Da_c - Da_{\rm FK}$ become of order unity. The monotonic growth of Da_c with Ra continues for increasing Ra. As seen in the plot, for sufficiently large values of $Ra \gtrsim 10^4$, the curve $Da_c(Ra)$ displays the asymptotic behavior $Da_c \propto Ra^{1/4}$, corresponding to a straight line with slope 1/4 in the log-log scale used in the figure. The dashed curve $Da_c = \Lambda_c Ra^{1/4}$ in the plot is the asymptotic prediction for $Ra \gg 1$, to be derived later in § 6.2.

The motion induced by buoyancy and its associated effects on the temperature field are investigated on the bottom plots of Figure 6.1 by representing the isotherms (left half of each

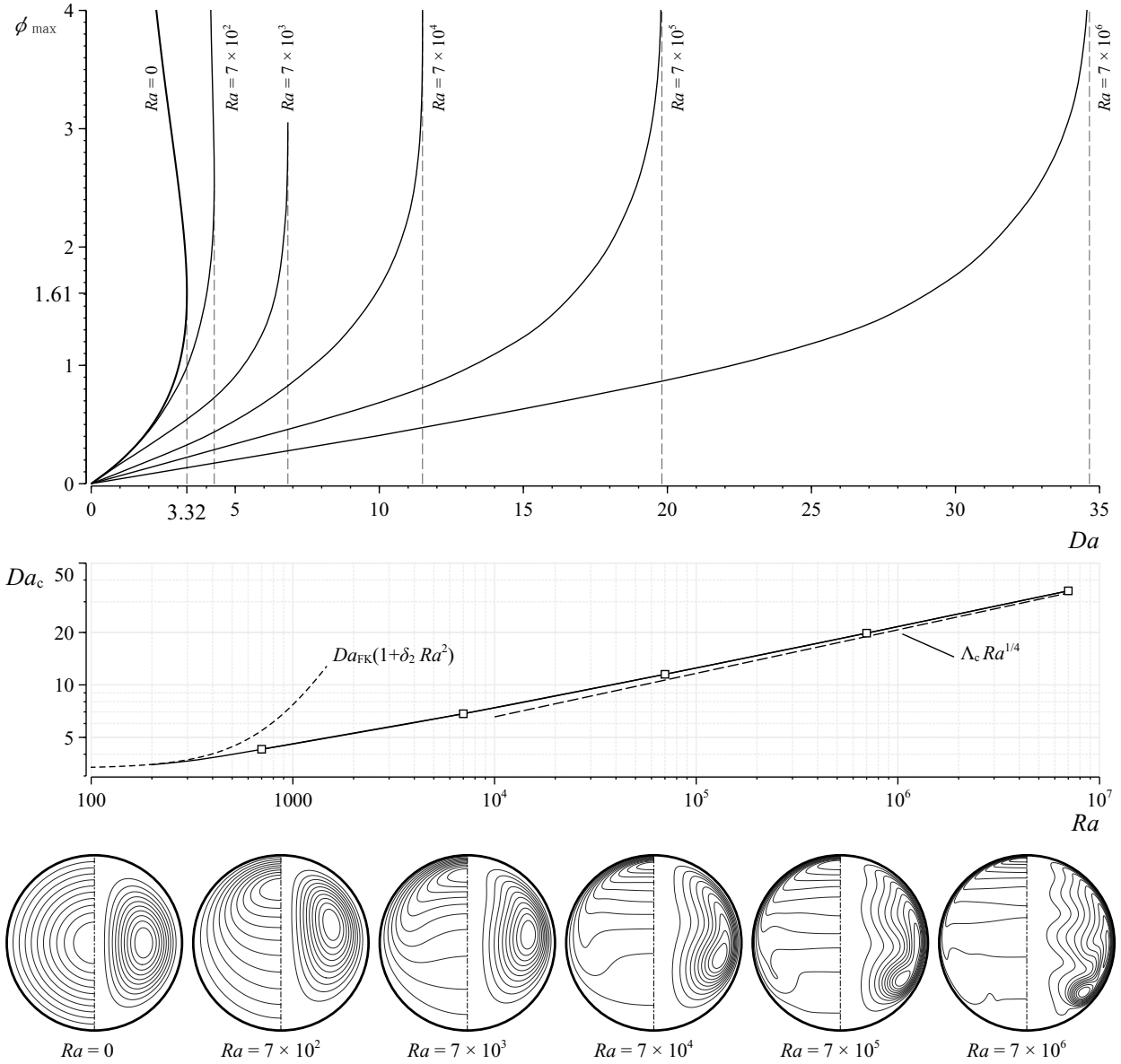

Figure 6.1: Results of numerical integrations of steady reactive flows for different values of Ra and Da. The upper plot shows the variation with Da of the peak temperature in the vessel for six different values of $Ra = 7 \times (0, 10^2, 10^3, 10^4, 10^5, 10^6)$. The middle plot shows the variation with Ra of the critical Damköhler number, including as dashed curves the asymptotic predictions $Da_c = Da_{\rm FK}(1 + \delta_2 Ra^2)$, derived in (Sánchez *et al.*, 2016) for $Ra \ll 1$, as well as the new result $Da_c = \Lambda_c Ra^{1/4}$ for $Ra \gg 1$, to be derived later in section 6.2. The bottom plots show ten isotherms (left half) and ten streamlines (right half) for the conditions corresponding to the six turning points of the upper plot.

circular plot) and streamlines (right half) corresponding to the solutions at the turning points of the six different explosion curves. A total of ten isocurves of temperature and stream function are shown in each subplot. The isotherms are equally spaced between the value $\phi = 0$ at the wall and

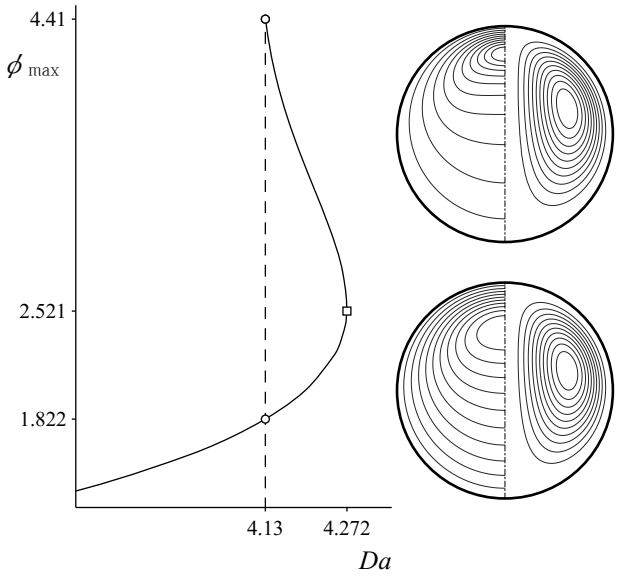

Figure 6.2: Detailed view of the explosion curve near the turning point for $Ra = 700$. The circular plots show isotherms (left half) and streamlines (right half) corresponding to $Da = 4.13$ for the solutions along the upper (unstable) branch and the lower (stable) branch. A total of 10 equally spaced isocurves is shown in each plot, with peak values of temperature and stream function given by $\phi_{\max} = 4.410$ and $\psi_{\max} = 1.594 \times 10^{-3}$ for the upper plot and $\phi_{\max} = 1.822$ and $\psi_{\max} = 1.380 \times 10^{-3}$ for the lower plot.

the peak value $\phi_{\max}$. Similarly, the selection of streamlines correspond to equally spaced values of the stream function ψ, defined such that $rv_r = \partial\psi/\partial z$ and $rv_z = -\partial\psi/\partial r$ with $\psi = 0$ at the wall, and the peak values being $\psi_{\max} = (1.6822 \times 10^{-3}, 1.5575 \times 10^{-3}, 5.728 \times 10^{-4}, 1.361 \times 10^{-4}, 2.7973 \times 10^{-5}, 5.6811 \times 10^{-6})$ for $Ra = 7 \times (0, 10^2, 10^3, 10^4, 10^5, 10^6)$.

It can be seen that the Frank-Kamenetskii vortex induced by buoyancy, symmetric about the equatorial plane for $Ra \ll 1$, evolves in a non-monotonic manner for increasing Ra, with the accompanying velocity, directed upwards in the central hot region, causing a vertical displacement of the peak temperature, which readily destroys the spherical symmetry of the temperature distribution, as noticed in early experimental observations (Tyler, 1966; Ashmore *et al.*, 1967). The streamline pattern indicates that the center of the vortex, which initially migrates upwards, moves eventually downwards to occupy a location near the wall, where a high-velocity boundary-layer flow develops for $Ra \gg 1$, as inferred by the close spacing between adjacent streamlines. The structure of the flow in that limit, which includes a central region of stratified temperature with a hot kernel near the "north pole" of the vessel, is to be considered in detail in section 6.2.

Unlike numerical schemes based on pseudo-transient methods, the root–finding technique employed here not only is able to describe the lower branch of stable solutions, extending between the origin of the explosion diagram $\phi_{\max} - Da$ and the turning point of the bending bifurcation,

but it can also be employed in principle to describe the unstable solutions lying beyond the turning point, corresponding to larger values of $\phi_{\max}$. For illustrative purposes, a detailed view of the turning point of the curve corresponding to $Ra = 700$ is shown in Fig. 6.2, along with the isotherms and streamlines corresponding to two different solutions for the same $Da < Da_c$. The description of the solutions along the upper branch becomes more difficult for larger Ra, because the curvature of the associated explosion curves at the turning point becomes smaller, leading to rapid variations of ϕ_{max} for $Da_c - Da \ll 1$ that hinder the convergence of the root-finding scheme. For these larger values of Ra, the value of Da_c reported here is defined as the maximum value of Da for which a converged solution is found. Numerical methods based on continuation techniques might be better suited for the description of the complete multi-branch explosion curve developing beyond the first turning point, but this alternative approach is not further pursued here because of the limited practical interest in these unstable solutions.

6.1.2 Transient computations

To complement the above steady solutions, transient histories corresponding to the initial conditions (4.10) were computed by marching in time the equations (4.4)–(4.6) supplemented with (4.8), with the boundary conditions given in (4.9). Besides the parameters Ra and Da, the Prandtl number $Pr = 0.7$, and the specific-heat ratio $\gamma = 1.4$, the results of the transient computations depend also on ϕ_I, the rescaled initial gas temperature in the container. As previously discussed, to ensure that the chemical reaction is negligible before the wall temperature is suddenly increased at $t = 0$, this negative temperature must satisfy $-\phi_I \gg 1$. The value $\phi_I = -10$ is employed in the computations reported below.

As in the steady computations, finite elements were used for the spatial discretization. The time-marching technique employed a characteristics-Galerkin method (Hecht, 2012; Carpio & Prieto, 2014) with a fixed time step Δt. The resulting system of linearized equations was solved at each time step using FreeFem++ (Hecht, 2012). The temporal evolution, including the associated ignition time for supercritical cases, was found to be independent of the choice of Δt provided that a sufficiently small value is employed. The solutions shown below in Figs. 6.3–6.5 correspond to $\Delta t = 10^{-5}$.

As expected, the transient computations reproduce the FK explosion boundary $Da_c(Ra)$ shown in the middle plot of Fig. 6.1 in that, regardless of the value of Ra, the unsteady flow for all subcritical values of the Damköhler number $Da < Da_c(Ra)$ was seen to evolve to reach the final steady–state solutions shown in Fig. 6.1 with indistinguishable differences, whereas for $Da > Da_c(Ra)$ a localized thermal runaway occurs at a finite time $t = t_i$, larger for smaller values of $Da - Da_c$.

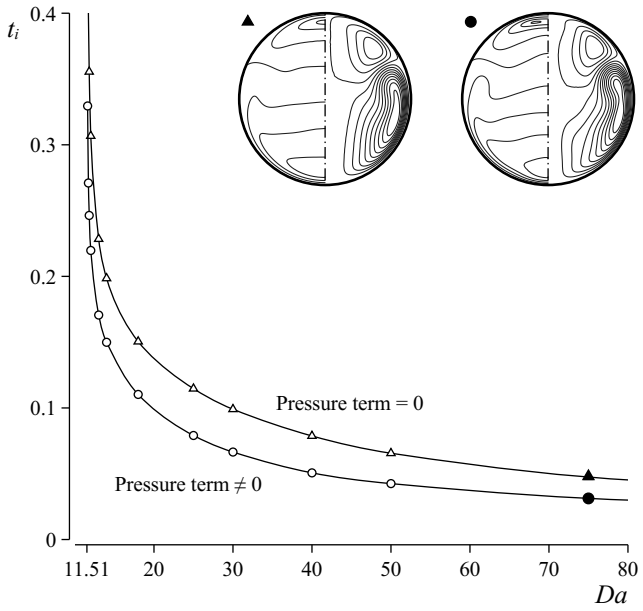

Figure 6.3: Ignition time for $Ra = 7 \times 10^4$ as a function of $Da > Da_c(Ra) \simeq 11.51$. The inset shows isotherms and streamlines for $Da = 75$ at $t \approx t_i$.

The variation of t_i with Da is shown in Fig. 6.3 for $Ra = 7 \times 10^4$. In the plot, the ignition time is defined as the last time for which a bounded solution is found in the numerical integration. Because of the precipitous character of the temperature increase, other definitions of the ignition time, based for instance on a given threshold value for the local rate of temperature increase, would produce almost identical results. The plot includes the curve $t_i(Da)$ obtained by neglecting in the energy equation (4.6) the term involving the temporal pressure increase. In view of these results, it can be concluded that computations of thermal explosions omitting this term, as was done in many previous studies (Liu *et al.*, 2008, 2010), may result in significant overpredictions of ignition times in chambers with rigid walls. The plot also indicates that, as expected, the computation of the critical value Da_c at which $t_i \to \infty$ is not affected by the presence of this unsteady term. To illustrate changes in the morphology of the ignition kernel, the insets in the figure show snapshots of isotherms and streamlines immediately before ignition for $Da = 75$. For this particular case, the ignition kernel is centered at a point along the axis when the term $\mathrm{d}\hat{p}/\mathrm{d}t$ is removed, but ignition occurs in a thin reacting annulus, slightly detached from the container axis, when this term is retained in the computation, as may be seen at the top of the insets.

As previously stated, the results in Fig. 6.3 correspond to $\phi_I = -10$. Since the duration of the heating period needed to increase the gas temperature in the container to values close to the wall value depends fundamentally on ϕ_I, lower values of ϕ_I result in larger ignition times, as was verified in additional computations. Nevertheless, the explosion limits, measured by the critical

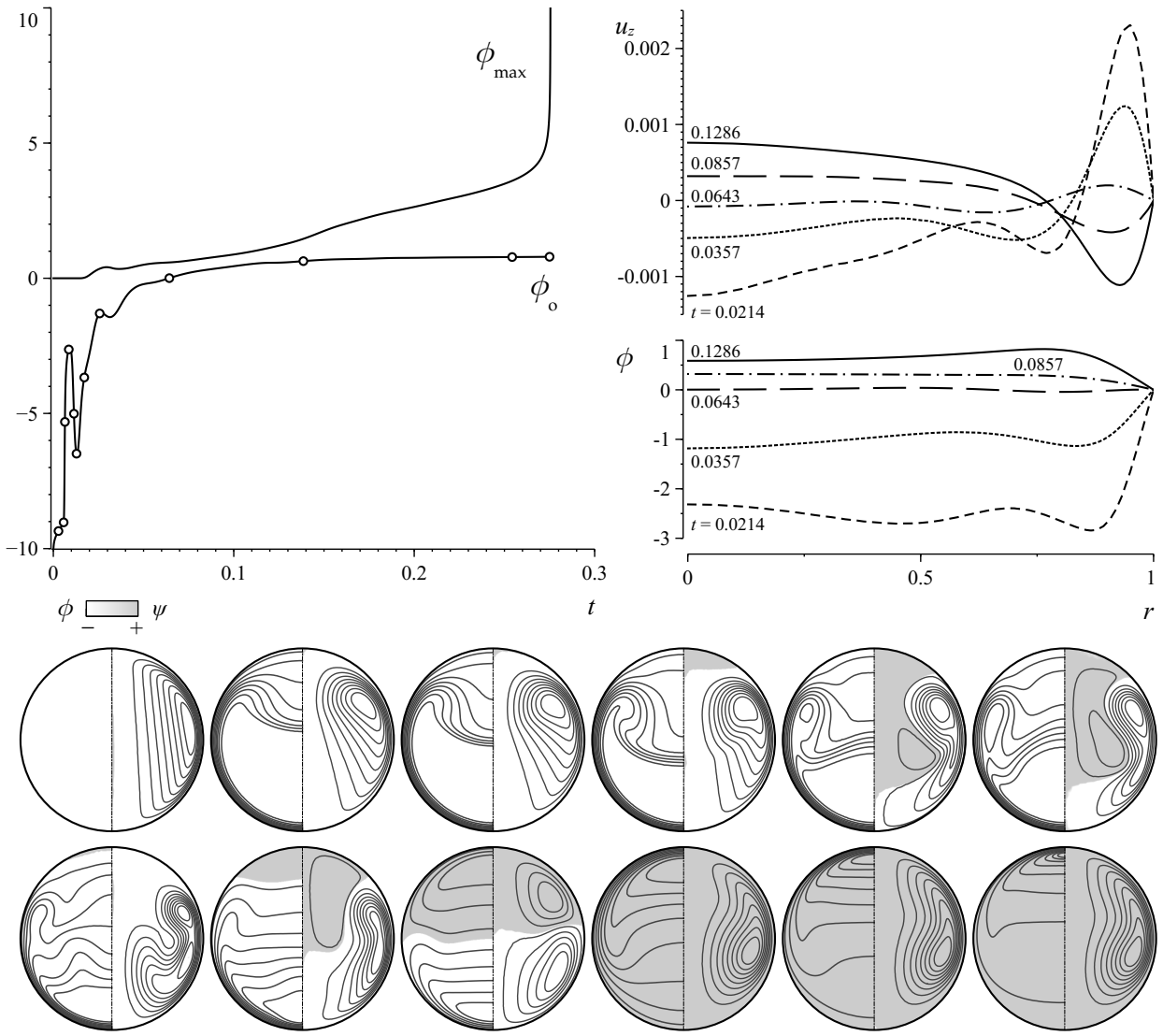

Figure 6.4: Results of transient numerical integrations of (4.4)–(4.6) with initial temperature $\phi_I = -10$, $Da = 11.75$, $Ra = 7 \times 10^4$. The temporal evolution of the temperature at the center ϕ_o and of the peak temperature $\phi_{\max}$ is shown in the top left panel, whereas sample equatorial profiles of vertical velocity u_z and temperature ϕ are plotted in the top right panel for times indicated in the figure. As in Figure 6.1, isotherms (left) and streamlines (right) are shown in the bottom panel for times marked with circles in the curve $\phi_o(t)$. The values of the stream function and temperature corresponding to each isocurve are selected to be equally spaced between the zero wall values and the peak values. The shade indicate positive values of the temperature (left half) and stream function (right half).

Damköhler number Da_c, were found to be independent of the selection of ϕ_I for all $\phi_I \leq 0$, in agreement with our previous results for buoyancy-free systems (Liñán *et al.*, 2016).

The role of buoyancy in the development of the thermal explosion is investigated in Fig. 6.4 for $Ra = 7 \times 10^4$ and $\phi_I = -10$ when the Damköhler number is $Da = 11.75$, only slightly above the

critical value $Da_c = 11.51$ predicted by the turning-point FK criterion. The upper left panel shows the temperature at the center of the vessel ϕ_o and the peak temperature $\phi_{\max}$, the latter displaying a precipitous growth at $t = t_i \simeq 0.28$. The twelve panels at the bottom show isotherms and streamlines at representative instants of time, marked with circles in the curve $\phi_o(t)$. The shading is used in the panels to indicate positive temperatures (above the wall value) and positive values of the stream function, corresponding to counterclockwise motion in the right-hand-side panels.

The heating of the gas from the hot wall affects initially a thin boundary layer that moves upwards under the action of gravity, entraining the surrounding cold gas and inducing a counterclockwise motion on the right inside the vessel. Because of the spherical geometry of the container, the boundary layer collides at the top of the sphere, ejecting downwards along the axis the gas that has been heated while ascending next to the wall. A secondary vortex with clockwise motion is seen to emerge from the collision region, thereby further complicating the dynamics. This convective transport rapidly heats the upper half of the vessel, while the bottom, nearly stagnant, remains initially cold.

The chemical reaction, initially negligible, begins to occur near the top of the sphere, causing the temperature to increase there above the wall value (i.e. positive values of ϕ) for $t \gtrsim 0.017$. The shaded region representing the hot gas extends rapidly downstream, changing in a fundamental way the gas motion. This can be seen in the snapshot corresponding to $t = 0.0643$ (the third from the left on the bottom row). In the upper half of the vessel $\phi > 0$, so that in the corresponding near-wall boundary layer the gas temperature is lower than that found outside. Consequently, buoyancy pulls the fluid downwards near the wall, supporting clockwise motion in this region. The opposite effect is found on the lower half of the vessel, where the temperature still remains negative. As a result, the flow at this intermediate time is characterized by the existence of two annular counterrotating vortices. For longer times, the hot gas occupies the entire vessel, and the resulting motion is given by a single vortex with clockwise motion, as in the steady cases displayed in Fig. 6.1. The change in sign of the heat flux from the wall and the corresponding flow reversal along the boundary layer are illustrated in the upper right plot of Fig. 6.4 by plotting the radial distributions of vertical velocity and temperature at the equatorial plane $z = 0$ at different instants of time.

As seen in the last three snapshots in Fig. 6.4, corresponding to $t = (0.1386, 0.2543, 0.2750)$, for this near-critical case the transient ignition history shows a relatively long stage of slow evolution in which the streamline pattern at all times is very similar to that of the FK solution at the turning point (see the plot for $Ra = 7 \times 10^4$ in Fig. 6.1). This quasi-steady motion is accompanied by a slow temperature evolution in which the values found in the central region remain almost constant, as seen in the evolution of ϕ_o, while the temperature distribution near the top develops

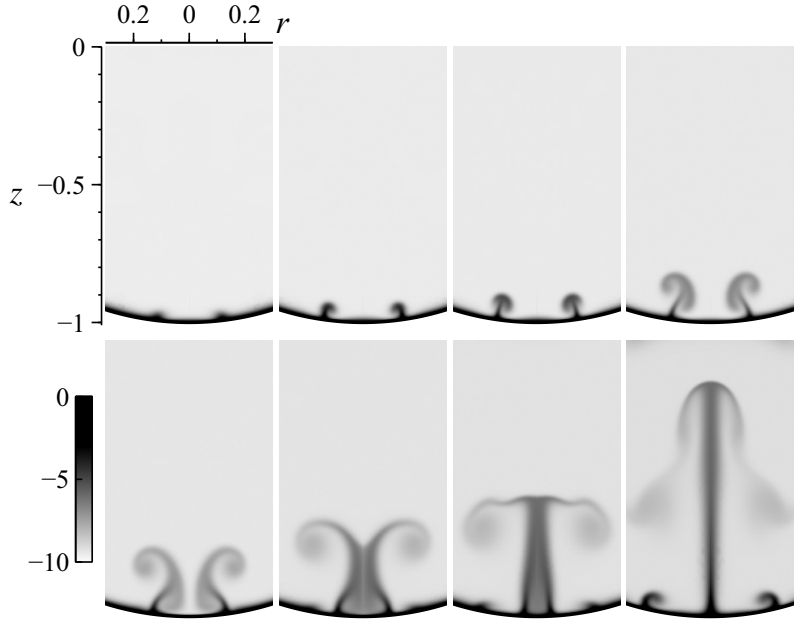

Figure 6.5: Snapshots at $t = (0.93, 1.07, 1.14, 1.29, 1.43, 1.64, 1.79, 2.00) \times 10^{-3}$ showing the formation of a plume as a result of a thermal instability near the bottom of the vessel for $Ra = 7 \times 10^6$. The shading represents temperature, varying between -10 (light) and 0 (dark).

an increasingly sharp peak that eventually transitions into a rapid runaway.

The heating dynamics becomes even more complicated for larger values of the Rayleigh numbers because of the development of flow instabilities. In particular, the thin layer of heated gas near the bottom may be subject to Rayleigh-Taylor-like instabilities that lead to the ejection of hot gas. This is illustrated in the series of snapshots shown in Fig. 6.5, corresponding to the initial stages of the heating process for $Ra = 7 \times 10^6$. It can be seen that the ejection occurs in the form of a toroidal plume, which soon develops into a thermal rising along the axis to eventually meet the jet of fluid coming down from the top collision region. The ejection process repeats itself in a quasi-periodic fashion, thereby providing an effective mechanism that contributes to the heating of the vessel interior.

It is worth noting that the dynamics described here is limited by the axisymmetric character of the integrations. The computations are not capable of describing the three-dimensional boundary-layer instabilities that are expected to be responsible for the transition to turbulence that has been postulated to occur for $Ra \gtrsim 10^6$ (Liu *et al.*, 2008, 2010). Uncertainties remain concerning exactly when transition occurs, but it seems likely that the patterns revealed in Fig. 6.5 will play some role in post-transitional development of the flow.

6.2 Slowly reacting flow for $Ra \gg 1$

6.2.1 Flow structure

The computations shown in Fig. 6.1 reveal that the structure of the flow in the limit $Ra \gg 1$ includes a central region of slowly moving hot gas bounded by a high-velocity near-wall boundary layer. The scales and the dominant balances applying in each region can be identified by an order-of-magnitude analysis. Thus, since the temperature increment must be $\phi \sim 1$ for the thermal explosion to develop, the buoyancy force in (4.5) can be anticipated to be of order unity when $Da \sim Da_c$, inducing streamwise velocities of order $Ra^{-1/2}$ in a near-wall boundary layer of characteristic thickness $Ra^{-1/4}$, as inferred from the convection-diffusion balance in (4.5). The flow in the central region, outside the boundary layer, is induced by the boundary-layer entrainment, with characteristic velocities of order $Ra^{-3/4}$. This slow motion does not induce an appreciable pressure disturbance inside the container, where (4.5) reduces in the first approximation to $-\nabla p' + \phi\, \boldsymbol{e}_z = 0$. This hydrostatic balance requires that the pressure p' and the temperature ϕ be a function of z only. This is consistent with the results shown in Fig. 6.1, where the isotherms for $Ra \gg 1$ are nearly horizontal outside the boundary layer. Since the velocities induced by boundary-layer entrainment are of order $Ra^{-3/4}$, the effective Peclet number, measuring in the central region the relative importance of convective and conductive rates, is of order $Ra^{1/4} \gg 1$, so that the effect of heat conduction can be neglected in the first approximation when writing (4.6) there. The resulting convection-reaction balance $Ra\, \boldsymbol{v}\cdot\nabla\phi = Da\, \mathrm{e}^{\phi}$, with $\boldsymbol{v} \sim Ra^{-3/4}$, indicates that for $Da \sim 1$ the temperature increase associated with the chemical reaction is limited to small values of order $Ra^{-1/4}$, insufficient to produce a significant increase in the reaction rate from its near-wall value, and that temperature increments of order unity, needed to trigger the thermal explosion, require values of the Damköhler number of order $Ra^{1/4}$. In this near-explosion regime, $Da \sim Ra^{1/4}$, the chemical reaction occurs mainly in the central region, while the boundary layer remains chemically frozen in the first approximation, because the transport rates there are larger than the reaction term by a factor of order $Ra^{1/4}$, as can be seen from (4.6).

Before proceeding with the analysis, it is worth pointing out that the flow structure identified here is fundamentally similar to that emerging in fully developed flow in a curved pipe at large values of the Dean number (Dennis & Riley, 1991). In both cases, the inviscid internal flow is coupled with a thin boundary layer that develops between two stagnation-point self-similar regions. Also, as we shall see below, the difficulties in the numerical solution stem in both cases from the elliptic character of the boundary-layer problem, associated with the existence of recirculating flow.

6.2.2 The boundary-layer problem

The leading-order form of the simplified equations in the chemically frozen boundary layer and in the central inviscid region are written now in terms of appropriately rescaled variables. The boundary layer developing at the wall is described in terms of the local distance to the wall $y = Ra^{1/4}[1 - (r^2 + z^2)^{1/2}]$ and the angle $\theta = \cos^{-1} z$, which measures the distance along the wall from the vessel top, giving the equations

$$\frac{\partial}{\partial\theta}(U\sin\theta) + \frac{\partial}{\partial y}(V\sin\theta) = 0 \tag{6.1}$$

$$\frac{1}{Pr}\left(U\frac{\partial U}{\partial\theta} + V\frac{\partial U}{\partial y}\right) = \frac{\partial^2 U}{\partial y^2} + (\phi_c - \phi)\sin(\theta) \tag{6.2}$$

$$U\frac{\partial\phi}{\partial\theta} + V\frac{\partial\phi}{\partial y} = \frac{\partial^2\phi}{\partial y^2} \tag{6.3}$$

where $U = Ra^{1/2}(zv_r - rv_z)$ and $V = -Ra^{3/4}(rv_r + zv_z)$ are the rescaled streamwise and transverse velocity components, respectively. The boundary conditions for $0 < \theta < \pi$ are

$$y = 0: \quad U = V = \phi = 0 \tag{6.4}$$

$$y \to \infty: \quad U = \phi - \phi_c(\theta) = 0. \tag{6.5}$$

Here $\phi_c(\theta)$ is the temperature outside the boundary layer, in the central inviscid region, given by the convection-reaction balance

$$\bar{v}_z\frac{\mathrm{d}\phi_c}{\mathrm{d}z} = \Lambda e^{\phi_c} \tag{6.6}$$

where $\Lambda = Ra^{-1/4}Da$ is a rescaled Damköhler number and $\bar{v}_z = Ra^{3/4}v_z$ is the rescaled vertical velocity, also a function of z, as required for consistency.

The conduction-free equation (6.6) describes the increase of the temperature of the ascending gas due to chemical reaction, from the value $\phi_c = 0$, found near the bottom $z = -1$, to reach the peak value $\phi_{\max}$ as $z \to 1$. The vertical velocity appearing as a factor in (6.6) can be obtained at a given height z by equating the upward mass flux $\pi(1 - z^2)\bar{v}_z$ in the container interior to the downward mass flux $2\pi(1 - z^2)^{1/2}\int_0^\infty U\mathrm{d}y$ across the boundary layer to give

$$\bar{v}_z = \frac{2\int_0^\infty U\mathrm{d}y}{(1 - z^2)^{1/2}}, \tag{6.7}$$

and the accompanying radial velocity $\bar{v}_r = Ra^{3/4}v_r$ is given by $\bar{v}_r = -(r/2)\mathrm{d}\bar{v}_z/\mathrm{d}z$, as follows from continuity. The geometrical relations $\sin\theta = (1 - z^2)^{1/2}$ and $\sin(\theta)\mathrm{d}\theta = -\mathrm{d}z$ can be used together with (6.7) to express (6.6) in the form

$$\frac{\mathrm{d}\phi_c}{\mathrm{d}\theta} = -\frac{\Lambda\sin^2(\theta)e^{\phi_c}}{2\int_0^\infty U\mathrm{d}y}, \tag{6.8}$$

yielding the solution

$$\phi_c(\theta) = \ln\left[e^{-\phi_{\max}} + \frac{\Lambda}{2}\int_0^\theta \frac{\sin^2(\tilde{\theta})}{\int_0^\infty U \mathrm{d}y}\mathrm{d}\tilde{\theta}\right]^{-1}, \tag{6.9}$$

upon integration with the initial condition $\phi_c(0) = \phi_{\max}$.

The integration of (6.1)–(6.3) must be initiated at $\theta \ll 1$, where there exists a self-similar solution. At the leading order described here, the solution is identical to that encountered near the attachment point of the buoyancy-driven boundary layer that develops over a hot sphere in a stagnant atmosphere when the Grashof number is large (Potter & Riley, 1980). The local flow, first described for the hot sphere in (Chiang *et al.*, 1964), can be analyzed by introducing the normalized coordinate $\zeta = \phi_{\max}^{1/4} y$ together with the stream function $\psi = \phi_{\max}^{1/4}\theta^2 F(\zeta)$ and the reduced temperature $G = (\phi_{\max} - \phi)/\phi_{\max}$ to give

$$F_{\zeta\zeta\zeta} + (2FF_{\zeta\zeta} - F_\zeta^2)/Pr + G = 0, \tag{6.10}$$

$$G_{\zeta\zeta} + 2FG_\zeta = 0, \tag{6.11}$$

with boundary conditions

$$F(0) = F_\zeta(0) = G(0) - 1 = 0 \tag{6.12}$$

$$F_\zeta(\infty) = G(\infty) = 0, \tag{6.13}$$

where the subscript ζ denotes differentiation with respect to this coordinate. The integration of (6.10)–(6.13) for $Pr = 0.7$ provides the profiles shown in Fig. 6.6 along with the value of $F(\infty) = 0.63702$, which can be used to write the relationship $\bar{v}_z(z = 1) = 2\phi_{\max}^{1/4} F(\infty)$ between the boundary temperature and the uniform entrainment velocity at $\theta = 0$. The uniformity of the boundary-layer entrainment rate near the top is consistent with the negligible radial variation of the vertical velocity $\bar{v}_z(z)$ in the reactive core region. The functions $F(\zeta)$ and $G(\zeta)$ provide the profiles of streamwise velocity and temperature

$$U = \phi_{\max}^{1/2}\theta F_\zeta \quad \text{and} \quad \phi = \phi_{\max}(1 - G) \qquad \text{at} \quad \theta \ll 1, \tag{6.14}$$

to be used as initial condition for integration of (6.1)–(6.3).

The apparent parabolic nature of (6.2) and (6.3) suggests a marching procedure in which (6.1)–(6.3) supplemented with (6.9) are integrated for increasing θ subject to the boundary conditions (6.4). The integration must be initiated at $\theta \ll 1$ using the self-similar profiles (6.14). In this scheme, the value of Λ corresponding to a given maximum temperature $\phi_{\max}$ is obtained from (6.9) as an eigenvalue by imposing the condition that $\phi_c \to 0$ as $\theta \to \pi$. This eigenvalue problem bears similarity with that encountered in the analysis of fully developed flow in curved pipes at large Dean number (Dennis & Riley, 1991). As in that case, the time-marching integration strategy

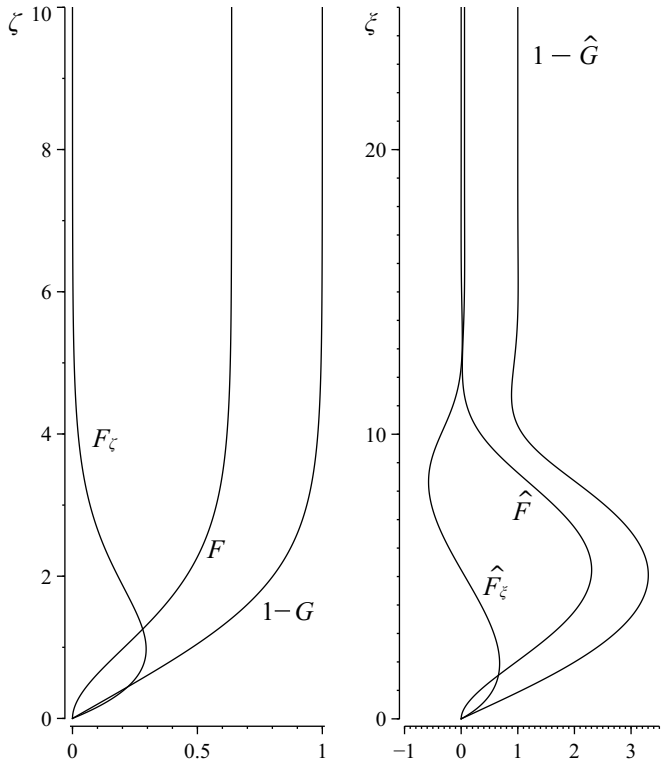

Figure 6.6: Results of the integration of (6.10)–(6.13) (left panel) and of (6.15)–(6.18) (right panel), showing the functions $F(\zeta)$, $F'(\zeta)$, $1-G(\zeta)$ and $\hat{F}(\xi)$, $\hat{F}'(\xi)$, $1-\hat{G}(\xi)$, respectively. The integrations indicate that $F(\infty) = 0.63702$ and $\hat{F}(\infty) = 0.05903$.

delineated above fails because of the appearance of recirculating flow. This is observed to emerge at an intermediate location between $\theta = \pi/2$ and $\theta = \pi$, with the velocity profile U exhibiting regions of negative U. This behavior seems to be consistent with the streamline patterns depicted in Fig. 6.1 for $Ra \gg 1$.

Because of the presence of backflow, the character of the resulting boundary-layer problem changes from parabolic to elliptic. The associated boundary-value problem requires consideration of the specific conditions found near the bottom $\theta = \pi$. There, the flow exhibits a self-similar solution, with the core temperature vanishing on approaching $\theta = \pi$ according to the power law $\phi_c = A(\pi-\theta)^\lambda$, consistent with the local scalings $U \propto (\pi-\theta)^{1+\lambda/2}$ and $y \propto (\pi-s)^{-\lambda/4}$, where the value of the exponent $\lambda = 8/5$ is determined from the convective-reactive balance (6.8). Writing (6.1)–(6.3) in terms of the local coordinate $\xi = A^{1/4}(\pi-\theta)^{2/5}y$, stream function $\psi = A^{1/4}(\pi-\theta)^{12/5}\hat{F}(\xi)$, and temperature increment $\phi_c - \phi = A(\pi-\theta)^{8/5}\hat{G}(\xi)$ yields

$$\hat{F}_{\xi\xi\xi} + \left(\tfrac{9}{5}\hat{F}_\xi^2 - \tfrac{12}{5}\hat{F}\hat{F}_{\xi\xi}\right)/Pr + \hat{G} = 0 \tag{6.15}$$

$$\hat{G}_{\xi\xi} - \tfrac{12}{5}\hat{F}\hat{G}_\xi - \tfrac{8}{5}\hat{F}_\xi(1-\hat{G}) = 0 \tag{6.16}$$

with boundary conditions

$$\hat{F}(0) = \hat{F}_\xi(0) = \hat{G}(0) - 1 = 0 \tag{6.17}$$

$$\hat{F}_\xi(\infty) = \hat{G}(\infty) = 0, \tag{6.18}$$

where the subscript ξ denotes differentiation with respect to this coordinate. The profiles $\hat{F}$, $\hat{F}_\xi$, and $\hat{G}$ are shown in Fig. 6.6 for $Pr = 0.7$. In connection with this self-similar solution it is worth noting that the boundary-layer thickness diverges as $(\pi-\theta)^{-2/5}$ as $\theta \to \pi$, indicative of a boundary layer that empties near the bottom, a flow feature consistent with the streamline patterns observed in the bottom plots of Fig. 6.1 for $Ra \gg 1$. This type of local behavior is fundamentally different from that emerging in free convection from a heated sphere, where the eruption of the fluid into the plume above the sphere is the result of the collision of the boundary layer at the upper stagnation point, as described by Potter and Riley (Potter & Riley, 1980). Also of interest is that the rescaled streamwise velocity $\hat{F}_\xi$ shown in Fig. 6.6 displays an oscillatory profile with multiple zeros. An emptying boundary layer with oscillatory velocity profile is also encountered near the inside bend of curved pipes at large Dean number (Smith, 1975), thereby further highlighting the similarities between both flows. The self-similar profiles can be used to write the velocity and temperature distributions as

$$U = A^{1/2}(\pi-\theta)^{9/5}\hat{F}_\xi, \;\; \phi_c - \phi = A(\pi-\theta)^{8/5}\hat{G} \;\text{ at } \pi - \theta \ll 1, \tag{6.19}$$

where the constant factor $A = [(5\Lambda)/(16\hat{F}(\infty))]^{4/5}$, obtained from (6.8), can be evaluated with use made of of the boundary value $\hat{F}(\infty) = 0.05903$ determined from the integration of (6.15)–(6.18).

Equations (6.1)–(6.3) must be integrated for $0 < \theta < \pi$ together with (6.9) subject to the boundary conditions (6.4) and to the local boundary distributions (6.14) and (6.19) at $\theta \ll 1$ and $\pi - \theta \ll 1$, respectively. In the solution, the value of Λ corresponding to a given $\phi_{\max}$ is an eigenvalue of the problem. The numerical solution of the above boundary–value problem was attempted using different methods, involving either a pseudo-transient scheme for advancing (6.1)–(6.3) or the simultaneous solution for U, V, and ϕ by means of a Newton-Raphson method, with the eigenvalue Λ updated after each iteration using (6.9). Despite significant efforts, difficulties associated with the strong sensitivity of the results to small changes in Λ precluded convergence of the method, so that a numerical solution to the problem could not be achieved. It is worth pointing out that similar difficulties have been encountered in connection with the boundary-value problem arising in curved pipes at large Dean number (Dennis & Riley, 1991), whose numerical solution also remains elusive to date. For this latter problem, an approximate solution based on the integral form of the boundary-layer equations was successfully employed by Ito (Ito, 1969). The same strategy is followed below to obtain the reduced explosion curve $\phi_{\max}$ as a function of Λ and the associated critical value Λ_c.

6.2.3 Von-Karman integral formulation

The approximate solution begins by integrating (6.2) and (6.3) across the boundary layer to give the two ordinary differential equations

$$\frac{1}{Pr}\frac{\mathrm{d}}{\mathrm{d}\theta}\left(\sin\theta\int_0^\infty U^2\mathrm{d}y\right) = -\sin\theta\left.\frac{\partial U}{\partial y}\right|_{y=0} + \sin^2\theta\int_0^\infty(\phi_c-\phi)\mathrm{d}y, \tag{6.20}$$

$$\frac{\mathrm{d}}{\mathrm{d}\theta}\left(\sin\theta\int_0^\infty U(\phi_c-\phi)\mathrm{d}y\right) - \sin\theta\frac{\mathrm{d}\phi_c}{\mathrm{d}\theta}\int_0^\infty U\mathrm{d}y = \sin\theta\left.\frac{\partial\phi}{\partial y}\right|_{y=0}. \tag{6.21}$$

Guided by the method employed in (Ito, 1969), it is further assumed that the boundary layer has a finite thickness $\delta(\theta)$ and that the temperature and streamwise velocity across the boundary layer can be expressed in the form

$$\phi = \phi_c\, k(\eta) \quad \text{and} \quad U = \phi_c \sin(\theta)\,\delta^2 f(\eta) + U_o h(\eta), \tag{6.22}$$

where the description for U incorporates a velocity correction $U_o(\theta)$ in addition to the direct effect of the gravitational acceleration. The functions $k(\eta)$, $f(\eta)$, and $h(\eta)$ of the normalized transverse coordinate $\eta = y/\delta$ are introduced to define the shape of the profiles. These shape functions are defined such that $k-1 = f = h = 0$ for $\eta \geq 1$, with polynomial expressions employed below for describing $k(\eta)$, $f(\eta)$, and $h(\eta)$ in the range $0 \leq \eta \leq 1$. In principle, a second-order polynomial for k and f and a third-order polynomial for h suffice to satisfy the boundary conditions

$$\begin{cases} k = f = h = 0 \text{ and } \frac{\mathrm{d}^2k}{\mathrm{d}\eta^2} = \frac{\mathrm{d}^2f}{\mathrm{d}\eta^2} + 1 = \frac{\mathrm{d}^2h}{\mathrm{d}\eta^2} = 0 \text{ at } \eta = 0 \\ k - 1 = f = h = 0 \text{ at } \eta = 1, \end{cases} \tag{6.23}$$

stemming from (6.4). Smoother profiles with vanishing derivatives at $\eta = 1$ can be obtained by increasing the order of the polynomials. In particular, the results shown below correspond to

$$k = \eta(2 - 2\eta^2 + \eta^3),\, f = \tfrac{1}{6}\eta(1-\eta)^3,\, h = \eta(1+3\eta)(1-\eta)^3 \tag{6.24}$$

which satisfy the additional boundary conditions

$$\frac{\mathrm{d}k}{\mathrm{d}\eta} = \frac{\mathrm{d}f}{\mathrm{d}\eta} = \frac{\mathrm{d}h}{\mathrm{d}\eta} = \frac{\mathrm{d}^2k}{\mathrm{d}\eta^2} = \frac{\mathrm{d}^2f}{\mathrm{d}\eta^2} = \frac{\mathrm{d}^2h}{\mathrm{d}\eta^2} = 0 \text{ at } \eta = 1. \tag{6.25}$$

The temperature in the interior of the vessel $\phi_c(\theta)$, the velocity correction $U_o(\theta)$, and the boundary-layer thickness $\delta(\theta)$ are to be computed by integration of (6.8) written in the form

$$\frac{\mathrm{d}\phi_c}{\mathrm{d}\theta} = -\frac{\Lambda\sin^2(\theta)e^{\phi_c}}{2\delta\left(\phi_c\sin(\theta)\delta^2\int_0^1 f\mathrm{d}\eta + U_o\int_0^1 h\mathrm{d}\eta\right)}, \tag{6.26}$$

together with the momentum and energy equations (6.20) and (6.21) written with use made of the expressions

$$\int_0^\infty U^2 \mathrm{d}y = \phi_c^2 \sin^2(\theta)\, \delta^5 \int_0^1 f^2 \mathrm{d}\eta + 2U_o \phi_c \sin(\theta)\, \delta^3 \int_0^1 fh \mathrm{d}\eta + U_o^2 \delta \int_0^1 h^2 \mathrm{d}\eta \tag{6.27}$$

$$\int_0^\infty U(\phi_c - \phi) \mathrm{d}y = \phi_c^2 \sin(\theta)\, \delta^3 \int_0^1 f(1-k) \mathrm{d}\eta + U_o \phi_c\, \delta \int_0^1 h(1-k) \mathrm{d}\eta \tag{6.28}$$

$$\int_0^\infty (\phi_c - \phi) \mathrm{d}y = \phi_c\, \delta \int_0^1 (1-k) \mathrm{d}\eta \tag{6.29}$$

$$\int_0^\infty U \mathrm{d}y = \phi_c \sin(\theta)\, \delta^3 \int_0^1 f \mathrm{d}\eta + U_o\, \delta \int_0^1 h \mathrm{d}\eta \tag{6.30}$$

$$\left.\frac{\partial U}{\partial y}\right|_{y=0} = \phi_c \sin(\theta)\, \delta \left.\frac{\mathrm{d}f}{\mathrm{d}\eta}\right|_{\eta=0} + \frac{U_o}{\delta} \left.\frac{\mathrm{d}h}{\mathrm{d}\eta}\right|_{\eta=0} \tag{6.31}$$

$$\left.\frac{\partial \phi}{\partial y}\right|_{y=0} = \frac{\phi_c}{\delta} \left.\frac{\mathrm{d}k}{\mathrm{d}\eta}\right|_{\eta=0}. \tag{6.32}$$

The equations were integrated by marching in θ. The integration is started with the initial values

$$\phi = \phi_{\max}, \quad U_o = C_U\, \phi_{\max}^{1/2} \theta, \quad \delta = C_\delta\, \phi_{\max}^{-1/4} \quad \text{at} \quad \theta \ll 1, \tag{6.33}$$

consistent with the previously identified self-similar solution (6.14). The constant factors C_U and C_δ are determined from the system of algebraic equations obtained by substituting (6.33) into (6.20) and (6.21), yielding the values $C_U = 0.021683$ and $C_\delta = 4.05827$ for the shape functions (6.24). The condition $\phi_c(\pi) = 0$ is used to determine the value of Λ corresponding to a given value of $\phi_{\max}$, producing the results shown in Fig. 6.7.

The lower plot in Fig. 6.7 represents typical profiles of δ, U_o, and ϕ_c for a large value of $\phi_{\max}$ (e.g., $\phi_{\max} = 7$ in the computation shown in the figure). Although the model (6.22) allows for the presence of backflow in the boundary layer, as would occur if U_o reaches sufficiently large negative values, such recirculating flow conditions were not achieved for any $\phi_{\max}$; instead, U_o was seen to remain always positive for $0 \le \theta \le \pi$. The nonzero value of U_o as $\theta \to \pi$, indicative of boundary-layer collision, can be attributed to the inherent limitations of this approximate model. As in Ito's analysis (Ito, 1969), the thickness of the mixing layer $\delta(\theta)$ shows a non-monotonic behavior for increasing θ and eventually diverges as $\theta \to \pi$, the latter boundary-layer thickening being consistent with the self-similar scaling $\delta \sim (\pi - \theta)^{-2/5}$ identified earlier for $\pi - \theta \ll 1$.

The upper plot in Fig. 6.7 shows the reduced explosion curve (i.e., the variation of the reduced Damköhler number Λ with $\phi_{\max}$). The integral method is not capable of describing the

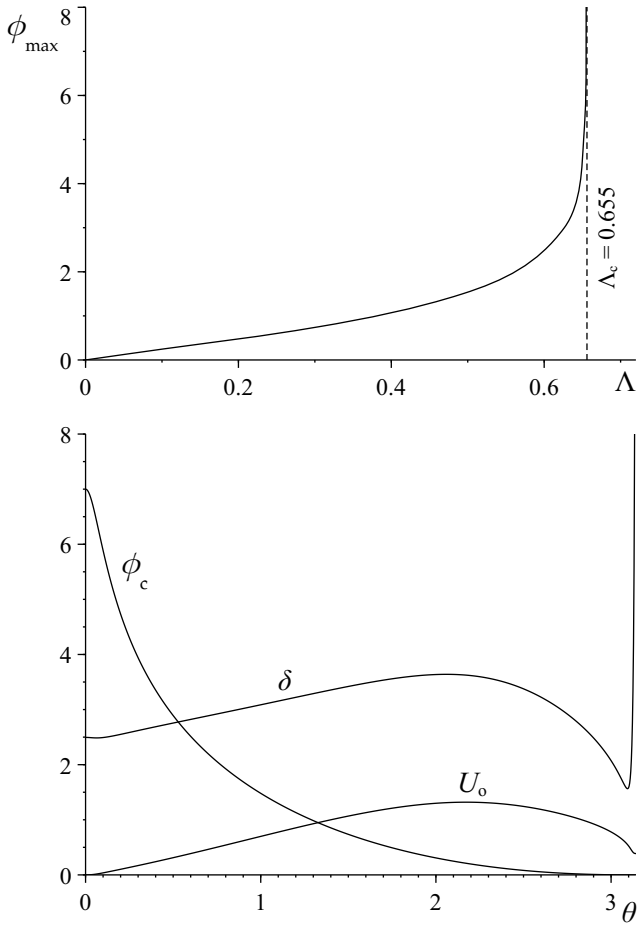

Figure 6.7: Results of numerical integrations of (6.20), (6.21) and (6.26) for the shape functions given in (6.24).

bending bifurcation; it yields instead a value of Λ that approaches a limiting value $\Lambda = \Lambda_c$ as $\phi_{\max} \to \infty$, seen in the upper plot. The vertical asymptote, rather than the turning point, identifies in this case the explosion limit, thereby providing the leading-order prediction

$$Da_c = \Lambda_c Ra^{1/4}. \tag{6.34}$$

For the polynomials (6.24) used in Fig. 6.7 the critical Damköhler number is found to correspond to $\Lambda_c \simeq 0.655$. Although a different selection of shape functions $k(\eta)$, $f(\eta)$, and $h(\eta)$ results in a different value of Λ_c, the associated changes were verified in additional computations to be only moderate. For instance, use of third-order polynomials for k and f and a fourth-order polynomial for h (satisfying (6.23) and having vanishing first-order derivatives at $\eta = 1$) yields instead the value $\Lambda_c = 0.616$. Since (6.34) can be expected to have relative errors of order $Ra^{-1/4}$ (that being the order of magnitude of the terms left out in the leading-order asymptotic description), the differences in Λ_c, on the order of 5%, are not very important for practical purposes, in that up to large values of $Ra \sim 10^6$ they lead to differences in predictions of Da_c that are comparable to or smaller than

the inherent errors of the leading-order result (6.34).

The asymptotic prediction (6.34) evaluated with $\Lambda_c = 0.655$ is compared in the middle plot of Fig. 6.1 with the critical Damköhler numbers computed numerically from integration of (4.4)–(4.6). As can be seen, the accuracy of the prediction is truly remarkable. The relative departures between the two curves remain of order $Ra^{-1/4}$, consistent with the relative errors present in the leading-order development leading to (6.34). Achievement of this degree of success in numerical accuracy with a von-Karman integral method is perhaps somewhat surprising.

6.3 Concluding remarks

Simplified equations, derived for the slowly reacting mode of combustion and accounting for buoyancy-induced motion as well as for the time variations of the pressure in the confined environment of the vessel, provide a useful basis for developing insights into fluid dynamics and heat-transfer mechanisms associated with this ignition process. Numerical integrations of the transient problem successfully describe the development of the thermal explosion. The integrations indicate that, despite the complex dynamics arising during the transient stage, the predictions of explosion limits derived from Frank-Kamenetskii's criterion (i.e., based on the existence of steady solutions with negligible fuel consumption) remain accurate over the whole range of Rayleigh numbers explored in this Chapter.

In the limit $Ra \gg 1$ appropriate scalings can be identified for deriving predictions of critical explosion conditions when the flow is dominated by buoyancy. A characteristic structure emerges, including an inviscid convective-reactive core of slowly rising hot fluid, surrounded by a descending near-wall boundary-layer flow driven by the negative buoyancy associated with the cooler walls. The presence of backflow in the boundary layer gives this boundary-layer problem an elliptic character, resulting in an appreciably complicated boundary-value problem which needs results of analyses of special, simpler boundary layers at the top and bottom of the vessel for determining the appropriate boundary condition for the computation of the boundary layer along the curved walls. An approximate solution method, employing an integral form of the boundary-layer equations, combined with presumed shapes for the temperature and velocity profiles, circumvents computational difficulties that are encountered in attempts to integrate numerically the elliptic boundary-value problem that arises for the boundary layer on the curved walls. The most significant result of the asymptotic analysis for $Ra \gg 1$ is the leading-order prediction (6.34) of the critical Damköhler number for explosion as a function of the Rayleigh number. The value of the proportionality factor $\Lambda_c \simeq 0.655$, obtained from the approximate analysis appears to be surprisingly accurate, as may be seen in the comparisons of critical explosion conditions shown in the

middle plot of Fig. 6.1.

This work serves to extend the Frank-Kamentskii theory of thermal explosions of ideal gas mixtures in rigid spherical vessels throughout the entire range of conditions over which buoyancy produces interior flows that remain laminar. The associated fluid-flow influences on explosion conditions become important only for Rayleigh numbers above a few hundred, and transitions to turbulent flow occur at Rayleigh numbers of a few million, whence the current results may be useful over about four orders of magnitude of the Rayleigh number. Both numerical and conceptual challenges were encountered, but the correct scalings for laminar flows at large Rayleigh numbers were established, along with the determination of reasonably accurate values for associated constants that appear in the scaling relations. Future studies for large Rayleigh numbers may address peculiar geometrical effects that are known to be encountered in vessels of different shapes (as indicated in the introduction of Chapter 4), or turbulent flows at higher Rayleigh numbers.

Chapter 6, in part, has been published in the *Internationl Journal of Heat and Mass Transfer*, "Thermal explosions in spherical vessels at large Rayleigh numbers", by I. Iglesias, D. Moreno-Boza, A. L. Sánchez, A. Liñán and F. A. Williams (2017) **115**, 1042-1053. The dissertation author is the primary investigator in this publication.

Future prospects

This section serves as a brief description of relevant topics in connection with what has been presented throughout Part II that can be subject of future investigation.

For instance, it is important to add that, although for simplicity our analysis was restricted to spherical vessels, the treatment can be generalized to non-symmetrical vessels, using (3.22) and (3.23) along with the linearized form of the continuity and momentum equations, with the latter including a term associated with the spatial variations of the pressure, which although small compared with p_o/β, play an important role in establishing the gas motion. It is also worth mentioning that the analyses presented in this dissertation can be readily extended to determine explosion lengths and critical explosion radii of pipes carrying combustible gaseous mixtures, a problem analyzed later in Appendix A.

On the other hand, while the present analysis pertains only to the classical one-step Arrhenius heat-release description underlying the FK theory. Extensions of the early FK theory incorporating realistic chemistry in descriptions of hydrogen-oxygen systems, have been shown to predict explosion conditions in spherical vessels in excellent agreement with experiments (Sánchez *et al.*, 2014), including critical pressures along the so-called third explosion limit (Sánchez & Williams, 2014). Possible influences of buoyant fluid motion on the resulting critical ignition conditions have

not been addressed. Corrections accounting for buoyancy effects could be incorporated in these analyses following the general procedure used here, accounting for the significant differences in the chemical-kinetic descriptions. In the absence of such studies, it remains unclear how significant the influences of the buoyant fluid motion will be on ignition in systems with real chemical kinetics, although it may be conjectured that the influence on the third limit, which retains a thermal-explosion character, may be comparable with what has been found here, while for the second limit, the branched-chain explosion, the influence may be larger.

In addition to the future worthwhile investigations of different fluid-mechanic and chemical-kinetic aspects of problems of this kind, as indicated above, it would also be of interest to address different geometrical configurations, other than the sphere. For example, the problem that has been analyzed by the present expansion procedure has not yet been considered in cylindrical geometry. Related ignition experiments have, in fact, been performed with gases contained in long cylindrical tubes, and an analysis of the present type may well be even simpler in cylindrical coordinates. Concerning the idealized reactive slab bounded by two isothermal infinite horizontal walls, which has been considered in a number of previous theoretical analyses (Jones, 1973; Kolesnikov, 1992; Joulin *et al.*, 1996; Kagan *et al.*, 1997), the resulting FK vortices could be investigated for different convective cells, including also rectangular and hexagonal shapes. These are just some of the many possible future investigations along these lines that could be revealing.

Future studies for large Rayleigh numbers may address peculiar geometrical effects that are known to be encountered in vessels of different shapes (as indicated in the introduction of Chapter 4), or turbulent flows at higher Rayleigh numbers. As indicated previously in the main text, our analysis may be limited for values of Ra for which the flow is inherently turbulent. Therefore, it is of practical interest the assessment of the range of Rayleigh numbers for which the predictions on the critical conditions for thermal explosion remain accurate.

Bibliography

Ashmore, P.G., Tyler, B.J. & Wesley, T.A.B. 1967 Experimental investigations of conductive and convective heat transfer in relation to thermal ignitions. *Proc. Combust. Inst.* **11**, 1133–1140.

Campbell, A.N., Cardoso, S.S.S. & Hayhurst, A.N. 2007 A comparison of measured temperatures with those calculated numerically and analytically for an exothermic chemical reaction inside a spherical batch reactor with natural convection. *Chem. Eng. Sci.* **62** (11), 3068–3082.

Carpio, J. & Prieto, J.L. 2014 An anisotropic, fully adaptive algorithm for the solution of convection dominated equations with semi-lagrangian schemes. *Comput. Methods in Appl. Mech. Eng.* **273**, 77–99.

Chiang, T., Ossin, A. & Tien, C.L. 1964 Laminar free convection from a sphere. *J. Heat Transfer* **86** (4), 537–541.

Dennis, S.C.R. & Riley, N. 1991 On the fully developed flow in a curved pipe at large dean number. *Proc. Roy. Soc. Lond. A* **434** (3), 473–478.

Frank-Kamenetskii, D.A. 1955 *Diffusion and heat exchange in chemical kinetics*. Princeton University Press.

Hecht, F. 2012 New development in freefem++. *J. Numer. Math.* **20** (3-4), 251–265.

Ito, H. 1969 Laminar flow in curved pipes. *Z. Angew. Math. Mech.* **49** (1), 653–663.

Jones, D.R. 1973 The dynamic stability of confined, exothermically reacting fluids. *Int. J. Heat Mass Transfer* **16** (1), 157–167.

Joulin, G., Mikishev, A.B. & Sivashinsky, G.I. 1996 A Semenov–Rayleigh–Benard problem. Unpublished.

Kagan, L., Berestycki, H., Joulin, G. & Sivashinsky, G. 1997 The effect of stirring on the limits of thermal explosion .

Kolesnikov, A.K. 1992 Convective instability of the horizontal reacting liquid layer in presence of various complicating factors. *Int. J. Heat Mass Transfer* **35**, 1091–1101.

Liñán, A., Moreno-Boza, D., Iglesias, I., Sánchez, A.L. & Williams, F.A. 2016 The slowly reacting mode of combustion of gaseous mixtures in spherical vessels. part 1: Transient analysis and explosion limits. *Combust. Theory Modelling* **20** (6), 1010–1028.

Liu, T.-Y., Campbell, A.N., Cardoso, S.S.S. & Hayhurst, A.N. 2008 Effects of natural convection on thermal explosion in a closed vessel. *Phys. Chem. Chem. Phys.* **10** (36), 5521–5530.

Liu, T.-Y., Campbell, A.N., Hayhurst, A.N. & Cardoso, S.S.S. 2010 On the occurrence of thermal explosion in a reacting gas: The effects of natural convection and consumption of reactant. *Combust. Flame* **157** (2), 230–239.

Potter, J.M. & Riley, N. 1980 Free convection from a heated sphere at large Grashof number. *J. Fluid Mech.* **100** (4), 769–783.

Sánchez, A.L., Iglesias, I., Moreno-Boza, D., Liñán, A. & Williams, F.A. 2016 The slowly reacting mode of combustion of gaseous mixtures in spherical vessels. part 2: Buoyancy-induced motion and its effect on the explosion limits. *Combust. Theory Modelling* **20** (6), 1029–1045.

Sánchez, A.L. & Williams, F. A. 2014 Recent advances in understanding of flammability characteristics of hydrogen. *Prog. Energy Combust. Sci.* **41**, 1–55.

Sánchez, A. L, Fernández-Tarrazo, E. & Williams, F. A 2014 The chemistry involved in the third explosion limit of h 2–o 2 mixtures. *Combust. Flame* **161** (1), 111–117.

Smith, F.T. 1975 Pulsatile flow in curved pipes. *J. Fluid Mech.* **71** (1), 15–42.

Tyler, B.J. 1966 An experimental investigation of conductive and convective heat transfer during exothermic gas phase reactions. *Combust. Flame* **10**, 90–91.

Appendix A

Large-activation-energy analysis of gaseous reacting flow in pipes

In the last Chapter of this dissertation, the exothermic reaction of an initially cold gaseous mixture flowing with a moderately large Reynolds number along a cylindrical pipe with constant wall temperature is analyzed. This work emerges as an extension of Frank-Kamenetskii's theory of thermal explosions, presented in Chapter 3, applied to a different geometry. An overall irreversible reaction with an Arrhenius rate having a large activation energy is used for the chemistry description. The flow is chemically frozen in the cold entrance region, where the velocity evolves towards the Poiseuille profile as the gas temperature increases to reach the wall value, ushering in a reaction stage during which the rate of heat transfer from the wall changes from positive to negative. The subsequent downstream evolution of the flow depends critically on the competition between the heat released by the chemical reaction and the heat-conduction losses to the wall, as measured by the Damköhler number δ, first introduced by Frank-Kamenetskii in his seminal analysis of thermal explosions in cylindrical vessels. For values of δ below the critical value $\delta = 2$ corresponding to the quasi-steady explosion limit, heat losses to the wall keep the gas temperature close to the wall value, so that the chemical reaction occurs slowly along the pipe in a flameless mode, which is analyzed to give an implicit expression for the streamwise reactant distribution. By way of contrast, for $\delta > 2$ the slow reaction rates occur only in an initial ignition region, which ends abruptly when very large reaction rates cause a temperature runaway, or thermal explosion, at a well-defined location, whose computation must account for the temperature found at the end of the entrance region. The predictions of the large-activation-energy analyses, including ignition distances for $\delta > 2$ and flameless reactant consumption rates for $\delta \leq 2$, show good agreement with numerical computations of the reactive pipe flow for finite values of the activation energy.

A.1 Introduction

The safe storage and transportation of reactant gas mixtures requires conditions that ensure a negligibly small reaction rate, achieved in storage vessels and transport pipes by lowering sufficiently the wall temperature. The seminal investigation of this problem is due to Frank-Kamenetskii (FK) (Frank-Kamenetskii, 1939), who studied a reacting mixture undergoing an exothermic chemical reaction in a centrally symmetric closed vessel with constant wall temperature. His analysis employed an overall irreversible reaction with an Arrhenius rate having a large activation energy, an appropriate model to represent the strong temperature dependence of the rate-controlling oxidation reactions in typical fuel-air mixtures (Frank-Kamenetskii, 1955; Zel'dovich *et al.*, 1985). The resulting gas-temperature distribution is seen to depend on the competition of the heat released by the chemical reaction and the heat losses to the wall, characterized by the Damköhler number δ, defined as the ratio of the conduction time across the vessel to the relevant characteristic time (i.e. the homogeneous thermal-explosion time at constant pressure) evaluated at the wall temperature (Zel'dovich *et al.*, 1985). A slowly reacting flameless mode of combustion is found for values of δ below a critical value, when the heat losses to the wall are able to limit the temperature rise, in such a way that the reaction rate does not change in order of magnitude from its near-wall value. Since the overall heat-release rate is proportional to the volume of reacting gas while the heat-loss rate to the wall is proportional to the wall surface, for a given wall temperature there exists a limiting size, corresponding to a critical value of δ, above which a slow reaction cannot be maintained, and is replaced by a localized temperature runaway that leads to the formation of a flame (Dold, 1985, 1989). More recent analyses of slowly reacting mixtures in closed vessels have addressed additional aspects of the problem, including the effects of pressure increase on the ignition time (Liñán *et al.*, 2016) and of buoyancy-induced motion on explosion limits (Kagan *et al.*, 1997; Liu *et al.*, 2008, 2010; Sánchez *et al.*, 2016).

The results of the FK analysis find direct application in connection with the safety storage of reactant mixtures, defining critical sizes for thermal explosions in chemically reacting systems. A related problem addressed here is that of reactant transportation in pipes, analyzed previously in a simplified configuration (Barenblatt *et al.*, 1997). Specifically, we consider below the discharge of a reactant mixture stored in a cold vessel at temperature T_I' through a pipe whose wall temperature is kept at a constant temperature $T_o' > T_I'$ with $T_o' - T_I' \sim T_o'$. The Damköhler number δ introduced by Frank-Kamenetskii for the analysis of thermal explosions in cylindrical vessels emerges as the main governing parameter (Barenblatt *et al.*, 1997). Our analysis identifies the existence of an entrance region with negligible chemical reaction, where the gas temperature increases from T_I' towards T_o' by heat conduction from the wall, immediately followed by a region of incipient chemical reaction

that governs the transition towards a persistent slowly reacting mode of combustion for $\delta \leq 2$ or the development of a thermal runaway for $\delta > 2$. Ignition events are analyzed to determine the explosion distance for $\delta > 2$, a computation that requires consideration of the upstream chemically frozen region of temperature accommodation. Specific attention is given to near-critical conditions with delayed ignition events. The development includes also an analytic description of the slowly reacting mode of combustion established downstream the transition region in subcritical configurations with $\delta \leq 2$.

A.2 Formulation

Consider a gaseous reactant mixture with initial temperature, density, and reactant mass fraction T_I', ρ_I', and Y_o discharging from a storage vessel along a pipe of radius a whose wall temperature is kept at a fixed value $T_o' > T_I'$. As in Frank-Kamenetskii's work (Frank-Kamenetskii, 1939), our analysis considers an overall Arrhenius reaction, with the mass of reactant consumed per unit volume per unit time $\dot{m}$ given by

$$\dot{m}/\rho' = k(T')Y_r = B\exp[-E/(RT')]Y_r, \tag{A.1}$$

where ρ', T', and Y_r represent the density, temperature and reactant mass fraction. The temperature-dependent reaction-rate constant

$$k = B\exp[-E/(RT')] = B\exp[-E/(RT_o')]\exp[\beta(T'-T_o')/T'], \tag{A.2}$$

includes a frequency factor B and an activation energy E, with R denoting the universal gas constant. The characteristic activation temperature E/R is assumed to be large compared with the wall temperature, resulting in a temperature-sensitive rate constant that changes from its wall value $B\exp[-E/(RT_o')]$ by a factor of order unity when $T'-T_o' \sim RT_o'^2/E = T_o'/\beta \ll T_o'$, where $RT_o'^2/E$ is the so-called FK temperature and $\beta = E/(RT_o') \gg 1$ is the nondimensional activation energy. A direct consequence of this strong temperature dependence is that, for initially cold mixtures with $T_o' - T_I' \sim T_o'$, the case considered here, the chemical reaction is effectively frozen in the storage vessel.

In this overall-reaction model the heat-release rate of the reaction per unit volume is given by $q\dot{m}$, where q denotes the amount of heat released per unit mass of reactant consumed. Correspondingly, the time t_e needed for the heat-release rate of the chemical reaction—evaluated at T_o' with the initial reactant mass fraction Y_o—to increase the enthalpy by an amount c_pT_o'/β, proportional to the FK temperature $RT_o'^2/E$, is given by

$$t_e = \frac{1}{\alpha\beta B\exp[-E/(RT_o')]}, \tag{A.3}$$

where $\alpha = (qY_o)/(c_pT'_o)$ is the dimensionless temperature rise, based on T'_o, for constant-pressure adiabatic combustion, with c_p representing the specific heat at constant pressure, taken as constant for simplicity. In relevant combustion applications the parameter α takes values that are of the order of, although typically larger than, unity. The chemical time t_e defined in (A.3) can be compared with the characteristic heat-conduction time across the pipe

$$t_c = a^2/D_T, \tag{A.4}$$

where D_T is the thermal diffusivity evaluated at T'_o, to define the FK parameter

$$\delta = t_c/t_e = (a^2/D_T)\alpha\beta B \exp[-E/(RT'_o)], \tag{A.5}$$

a Damköhler number characterizing the slowly reacting mode of combustion of enclosed reactant mixtures, with the value $\delta = 2$ identifying the explosion limit in cylindrical vessels (Frank-Kamenetskii, 1939, 1955; Zel'dovich *et al.*, 1985).

The discharge is assumed to occur at low Mach numbers, resulting in spatial pressure differences in the pipe that are small compared with the vessel pressure, so that the equation of state can be written in the simplified form $\rho' T' = \rho'_I T'_I$. A convenient characteristic value for the streamwise flow velocity $U = G/(\rho'_o \pi a^2)$ can be defined from the known mass flow rate G by using the density $\rho'_o = \rho'_I T'_I/T'_o$ evaluated at $T' = T'_o$. This velocity defines the Peclet number of the pipe flow $Pe = Ua/D_T$, comparable in magnitude to the associated Reynolds number $Re = Pe/Pr$, with Pr denoting the order-unity Prandtl number of the gaseous mixture. The following analysis pertains to configurations with moderately large values of the Reynolds number $Re \sim Pe$ in the range $10 \lesssim Re \lesssim 2000$, for which the flow in the pipe is stable and slender, with a characteristic streamwise development length $\ell = Pe\, a$ much larger than the pipe radius a. The resulting steady laminar flow can be analyzed in the boundary-layer approximation by integrating

$$\frac{\partial}{\partial x}(\rho u) + \frac{1}{r}\frac{\partial}{\partial r}(r\rho v) = 0 \tag{A.6}$$

$$\rho u\frac{\partial u}{\partial x} + \rho v\frac{\partial u}{\partial r} = -P_l(x) + \frac{Pr}{r}\frac{\partial}{\partial r}\left(rT^\sigma\frac{\partial u}{\partial r}\right) \tag{A.7}$$

$$\rho u\frac{\partial T}{\partial x} + \rho v\frac{\partial T}{\partial r} = \frac{1}{r}\frac{\partial}{\partial r}\left(rT^\sigma\frac{\partial T}{\partial r}\right) + \frac{\delta}{\beta}\rho Y \exp[\beta(T-1)/T] \tag{A.8}$$

$$\rho u\frac{\partial Y}{\partial x} + \rho v\frac{\partial Y}{\partial r} = \frac{1}{Le\, r}\frac{\partial}{\partial r}\left(rT^\sigma\frac{\partial Y}{\partial r}\right) - \frac{\delta}{\alpha\beta}\rho Y \exp[\beta(T-1)/T] \tag{A.9}$$

for $x > 0$ and $0 < r < 1$ supplemented with the equation of state

$$\rho T = 1 \tag{A.10}$$

and subject to the initial conditions

$$x = 0: \quad u - T_I = T - T_I = Y - 1 = 0 \tag{A.11}$$

at the pipe entrance, and the boundary conditions

$$\frac{\partial u}{\partial r} = v = \frac{\partial T}{\partial r} = \frac{\partial Y}{\partial r} = 0 \quad \text{at} \quad r = 0 \tag{A.12}$$

and

$$u = v = T - 1 = \frac{\partial Y}{\partial r} = 0 \quad \text{at} \quad r = 1 \tag{A.13}$$

for $x > 0$, as corresponds to axially symmetric flow bounded by a non-permeable constant-temperature wall with non-slip flow.

In the formulation the axial and radial coordinates x' and r' are scaled with $\ell = Pe\, a$ and a according to $x = x'/\ell$ and $r = r'/a$, while their associated velocity components u' and v' are scaled with U and D_T/a to give $u = u'/U$ and $v = v'/(D_T/a)$, respectively. With the scale selected for the axial velocity, its initial uniform value $u'_I = G/(\rho'_I \pi a^2)$ becomes $u'_I/U = \rho'_o/\rho'_I = T_I$ when expressed in dimensionless form, as shown in (A.11). The reactant mass fraction Y_r is normalized with its initial value Y_o to give $Y = Y_r/Y_o$, and the temperature and density are scaled with T'_o and ρ'_o to give the nondimensional variables $T = T'/T'_o$ and $\rho = \rho'/\rho'_o$. The unknown streamwise pressure gradient $P_l(x)$, to be determined as part of the integration, has been scaled with its characteristic value $\rho'_o U^2/\ell$. Its presence in pipe flow ensures mass-flux conservation. Besides the Prandtl number Pr, the Lewis number Le, and the assumed exponent σ for the power-law temperature dependence of the transport coefficients, the problem depends on four nondimensional parameters, namely, the activation energy $\beta = E/(RT'_o)$, the heat-release parameter $\alpha = (qY_o)/(c_p T'_o)$, the Damköhler number δ, and the initial-to-wall temperature ratio $T_I = T'_I/T'_o < 1$. The analysis below considers the simplified solution that arises for moderately large values of β with $\alpha \sim 1$, $\delta \sim 1$, and $1 - T_I \sim 1$.

A.3 Sample numerical results

Figure A.1 shows results of numerical integrations of (A.6)–(A.13) for $\sigma = 0.7$, $Pr = 0.7$, $Le = 1.0$, $\beta = 10$, $\alpha = 5$, and $T_I = 0.5$. A standard Crank-Nicholson method (Pletcher *et al.*, 2012) was used to advance the fluid variables in the streamwise direction whereas a collocation technique (Driscoll *et al.*, 2014) was used for the radial discretization of the corresponding operators at each axial station. For stability, a modified backward Euler method was used for the initial steps. Typical values of the step size were $\Delta x = 10^{-4}$ for the initial steps and $\Delta x = 10^{-3}$ after 4 or 5 steps. Computations with both finer and coarser grids were performed to ensure that the results were independent of the grid size.

The plots in Fig. A.1 show the evolution along the axis of the temperature $T(x, 0)$, reactant mass fraction $Y(x, 0)$, and reduced reaction rate

$$\omega(x, 0) = Y \exp[\beta(T - 1)/T]$$

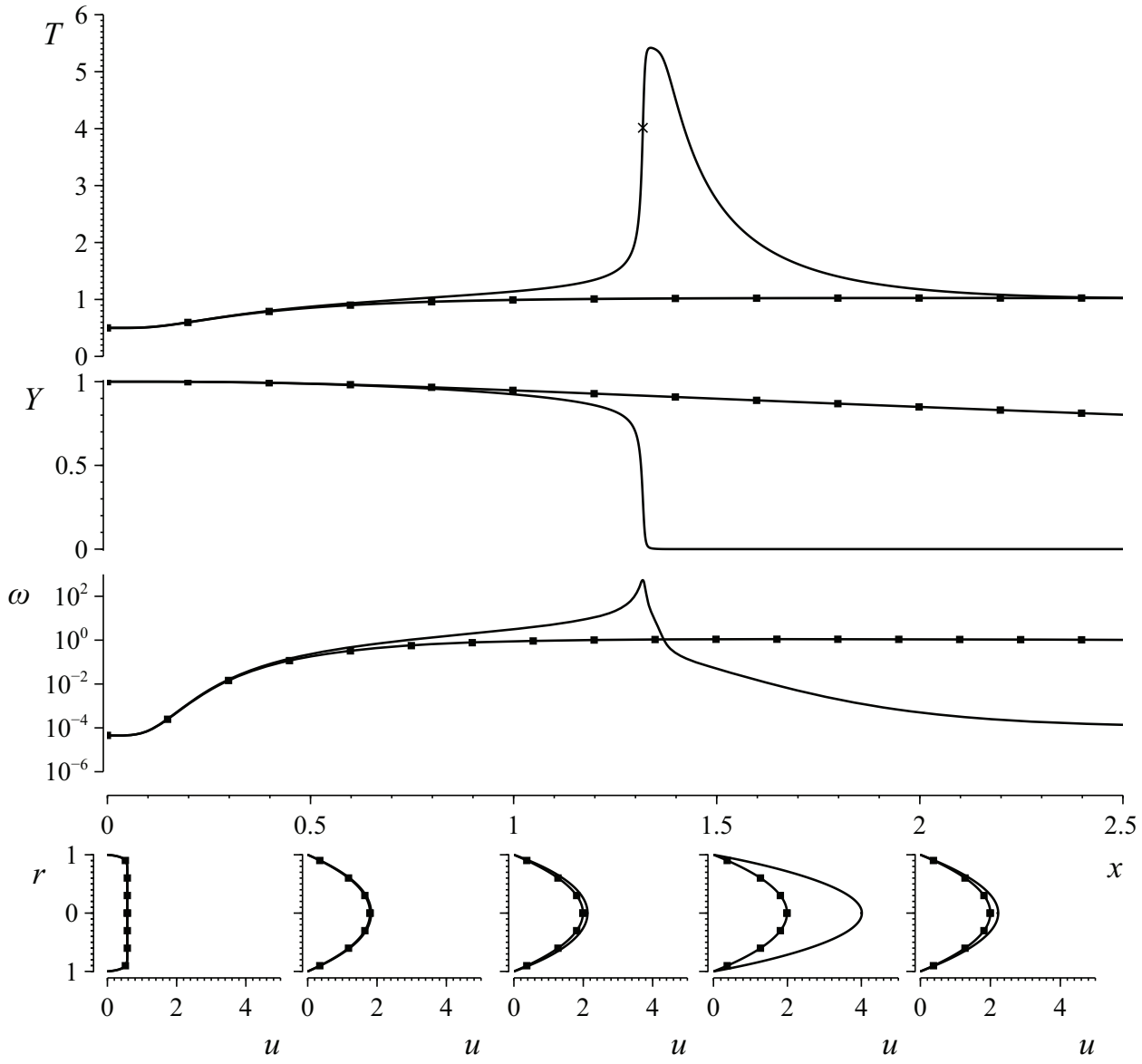

Figure A.1: The variation with axial distance of $T(x,0)$, $Y(x,0)$, and $\omega(x,0) = Y\exp[\beta(T-1)/T]$ obtained by numerical integration of (A.6)–(A.13) with $\sigma = 0.7$, $Pr = 0.7$, $Le = 1.0$, $\beta = 10$, $\alpha = 5$, and $T_I = 0.5$ for $\delta = 1.0$ (squares) and $\delta = 5.0$ (plain curves); the bottom plots show the axial velocity profiles at five different locations $x = (0, 0.5, 1.0, 1.5, 2.0)$. The cross on the temperature curve for $\delta = 5.0$ indicates the location of the inflection point, used in the numerical integrations to characterize the ignition distance.

for two different values of $\delta = (1.0, 5.0)$, along with the corresponding radial profiles of axial velocity at different streamwise locations. The two Damköhler numbers are selected as representative of subcritical and supercritical ignition events. In both cases, the integrations reveal the existence of an initial chemically frozen region, with exponentially small values of $\omega \ll 1$, where the gas temperature increases as a result of the heat transferred from the wall, while the reactant mass

fraction does not change significantly. Because of the associated decrease in density, the velocity is seen to increase as its profile evolves from the initial uniform distribution $u = T_I$ towards a parabolic distribution $u = 2(1 - r^2)$.

While the initial evolution is nearly identical for both values of δ, the subsequent downstream evolution is very different. Thus, for $\delta = 1.0$ the reaction rate ω increases to a maximum value of order unity, leading to the establishment of a slowly reacting mode of combustion with $T(x, 0) - 1 \sim \beta^{-1}$ and small reactant consumption rates $\omega/(\alpha\beta) \sim 1/(\alpha\beta) \ll 1$. By way of contrast, for $\delta = 5$, the reaction rate continues to increase to very large values, leading to a rapid temperature increase at a well defined ignition location $x \simeq 1.32$, where the reactant is rapidly depleted as the temperature reaches its peak value. In the equilibrium region found farther downstream the temperature decreases as a consequence of heat losses to the wall, eventually approaching the wall value $T = 1$ for $x \gg 1$. Following the criterion used in ignition studies in homogeneous systems, the inflection point of the curve $T(x, 0)$, marked with a cross in Fig. A.1, can be used as a definition of the ignition distance in these computations; other criteria, such as the location of the peak temperature, would give essentially the same results in the limit $\beta \gg 1$.

A.4 The chemically frozen entrance region

As discussed above, the flow in the tube includes an entrance development region of characteristic length $\ell = Pe\, a$, corresponding to values of x of order unity, where the velocity profile evolves from an initial uniform profile $u = T_I$ to a Poiseuille profile $u = 2(1 - r^2)$ while the temperature evolves from the initial value $T = T_I < 1$ to the wall value $T = 1$. As a consequence of the exponential temperature dependence of the reaction rate discussed earlier, the chemical reaction can be entirely neglected as long as $1 - T \gg \beta^{-1}$, so that the reactant mass fraction remains equal to its initial value $Y = 1$ in this entrance region, as can be seen by integrating the chemically frozen version of (A.9) with initial condition $Y = 1$ at $x = 0$ and boundary conditions $\partial Y/\partial r = 0$ at $r = 0$ and $r = 1$. The associated distributions of u and T are obtained by integration of (A.6)–(A.8) with the initial and boundary conditions given in (A.11)–(A.13); the chemical reaction being discarded in (A.8). The solution depends on the initial temperature T_I and on the transport description through the values of σ and Pr, with the realistic values $\sigma = 0.7$ and $Pr = 0.7$ selected in the integrations reported below, as is appropriate for fuel-air gas mixtures (Rosner, 2012).

The resulting chemically frozen, low-Mach-number laminar gas flow has been treated in the past (Kays & Nicoll, 1963; Davenport & Leppert, 1965; Worsøe-Schmidt & Leppert, 1965) to assess effects of variable gas properties on the friction coefficient and heat-transfer rate, including recent efforts to characterize the solution for extreme values of T_I (Higuera, 2011). These previous analyses,

which extended to variable density the classical constant-density entry–flow results (Van Dyke, 1964), did not consider specifically the asymptotic behavior of the solution for values of x moderately larger than unity, where the temperature differences from the wall value and of the velocity from the Poiseuille distribution become small. This asymptotic behavior is needed in reacting flows for the analysis of the initiation of the reaction as the temperature increases to near-wall values such that $1 - T \sim \beta^{-1}$. In this region of incipient chemical reaction, located downstream from the entrance region, the heat-transfer rate from the wall changes from positive to negative as a result of the chemical heat release. As seen in Fig. A.1, depending on the conditions, the temperature either continues to increase, leading to a thermal runaway at a finite distance downstream, or reaches a maximum value $T - 1 \sim \beta^{-1}$ corresponding to a quasisteady balance between the heat released by the chemical reaction and the heat losses to the walls.

The asymptotic temperature distribution for the non-reacting gaseous pipe flow at $x \gg 1$ is given by

$$T - 1 = -C \exp(-\lambda_1^2 x/2) \exp(-\lambda_1 r^2/2) L_{(\lambda_1-2)/4}(\lambda_1 r^2), \tag{A.14}$$

as can be obtained by using separation of variables in

$$2(1 - r^2)\frac{\partial}{\partial x}(T - 1) = \frac{1}{r}\frac{\partial}{\partial r}\left[r\frac{\partial}{\partial r}(T - 1)\right], \tag{A.15}$$

derived by linearizing (A.8) for $T - 1 \ll 1$ with $u \simeq 2(1 - r^2)$ and $v \simeq 0$. Here $L_{(\lambda_1-2)/4}$ is the Laguerre polynomial of order $(\lambda_1 - 2)/4$, with the value of $\lambda_1 = 2.704$ determined as the smallest root of the equation $L_{(\lambda-2)/4}(\lambda) = 0$ associated with the condition $T = 1$ at $r = 1$. The factor C is an unknown positive constant of order unity that must be obtained from the numerical integration of the entrance flow, giving the results shown in Fig. A.2. The plot shows the variation with T_I of C and $(2/\lambda_1^2) \ln C$; the latter is to be employed later in evaluating the ignition distance through (A.24).

A.5 Slowly reacting flow

The exponential temperature decay (A.14) is modified as the chemical reaction begins to have a significant effect, which occurs when the temperature drop from the wall value $1 - T$ decreases to values of order β^{-1} across most of the pipe section. The condition $1 - T = \beta^{-1}$ evaluated with use made of the temperature drop along the axis $1 - T(x, 0) = C \exp(-\lambda_1^2 x/2)$ given in (A.14) provides

$$x_d = (2/\lambda_1^2) \ln(C\beta), \tag{A.16}$$

as an expression for the downstream location x_d where the reaction becomes important, marking the end of the chemically frozen flow. The following region of incipient chemical reaction, where

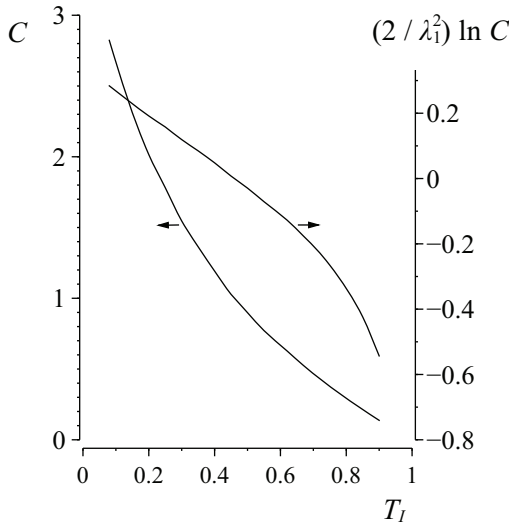

Figure A.2: The factor C for the asymptotic temperature distribution (A.14) found at the end of the chemically frozen entrance region, obtained numerically by fitting (A.14) to the results of integrations of (A.6)–(A.8) with the initial and boundary conditions given in (A.11)–(A.13) and with the chemical reaction neglected in (A.8). The plot also shows the associated value of $(2/\lambda_1^2)\ln C = 0.274\ln C$, which carries in (A.24) the dependence of the ignition distance on the initial temperature.

$T-1 \sim u-2(1-r^2) \sim v \sim \rho-1 \sim \beta^{-1} \ll 1$, can be described in terms of the translated coordinate $\hat{x} = x - x_d$ and the rescaled temperature increment $\theta = \beta(T' - T'_o)/T'_o$, reducing the problem to the integration of

$$2(1-r^2)\frac{\partial\theta}{\partial\hat{x}} = \frac{1}{r}\frac{\partial}{\partial r}\left(r\frac{\partial\theta}{\partial r}\right) + Y\delta \mathrm{e}^{\theta} \tag{A.17}$$

$$2(1-r^2)\frac{\partial Y}{\partial\hat{x}} = \frac{1}{Le\, r}\frac{\partial}{\partial r}\left(r\frac{\partial Y}{\partial r}\right) - \frac{1}{\alpha\beta}Y\delta \mathrm{e}^{\theta} \tag{A.18}$$

with initial conditions

$$\theta + \exp(-\lambda_1^2\hat{x}/2)\exp(-\lambda_1 r^2/2)L_{(\lambda_1-2)/4}(\lambda_1 r^2) = Y - 1 = 0 \quad \text{as} \quad \hat{x} \to -\infty \tag{A.19}$$

and boundary conditions

$$\frac{\partial\theta}{\partial r} = \frac{\partial Y}{\partial r} = 0 \quad \text{at} \quad r = 0 \qquad \text{and} \qquad \theta = \frac{\partial Y}{\partial r} = 0 \quad \text{at} \quad r = 1. \tag{A.20}$$

The initial conditions for integration of (A.17) and (A.18), given in (A.19), are obtained by matching with the solution found in the entrance region at intermediate distances $1 \ll x \ll x_d$, corresponding to large negative values of the translated coordinate $\hat{x} = x - x_d$, represented by the limit $\hat{x} \to -\infty$ in (A.19). In particular, the initial temperature distribution is obtained by writing the temperature profile (A.14) in terms of $\hat{x} = x - x_d$ with use made of (A.16). The Frank-Kamenetskii linearization

$\exp[\beta(T-1)/T] = \exp[\theta/(1+\theta/\beta)] \simeq \mathrm{e}^{\theta}$ has been employed in writing the reaction rate in (A.17) and (A.18), as it is appropriate in the limit $\beta \gg 1$ with $\theta \sim 1$.

A.6 The first reaction stage

The analysis of the chemical reaction at distances $\hat{x} = x - x_d \sim 1$ determines whether the solution undergoes a thermal runaway, as occurs for supercritical cases with $\delta > 2$, or whether the flow evolves into a quasisteady slow mode of combustion that persists farther downstream, as occurs for $\delta \leq 2$. In this transition region $x \sim 1$ with $\theta \sim 1$ the change in reactant mass fraction is small, of order $1 - Y \sim (\alpha\beta)^{-1} \ll 1$, as follows from (A.18), so that the problem reduces to the integration of

$$2(1-r^2)\frac{\partial\theta}{\partial\hat{x}} = \frac{1}{r}\frac{\partial}{\partial r}\left(r\frac{\partial\theta}{\partial r}\right) + \delta \mathrm{e}^{\theta} \tag{A.21}$$

subject to the initial and boundary conditions given above in (A.19) and (A.20). Selected results of computations are shown in Fig. A.3. In the integrations, a low-storage standard RKW3 method (Spalart *et al.*, 1991) was used for advancing in $\hat{x}$ with a variable step size with minimum value $\Delta\hat{x} = 10^{-3}$. The pseudospectral technique (Driscoll *et al.*, 2014) used previously in integrating (A.6)–(A.13) was employed for the radial discretization of (A.21). The integration was initiated with the temperature profile given in (A.19) evaluated at a selected negative value of $\hat{x}$ and the results were found to be independent of the selection for values of the initial location smaller than -1.

For subcritical cases with $\delta \leq 2$ the temperature evolves towards the steady distribution

$$\theta_{\mathrm{FK}} = 2\ln\left\{\frac{2/(1+\sqrt{1-\delta/2})}{1+(\delta/2)[r/(1+\sqrt{1-\delta/2})]^2}\right\} \tag{A.22}$$

corresponding to the cylindrical FK problem

$$\frac{1}{r}\frac{\mathrm{d}}{\mathrm{d}r}\left(r\frac{\mathrm{d}\theta_{\mathrm{FK}}}{\mathrm{d}r}\right) = -\delta\, e^{\theta_{\mathrm{FK}}}, \quad \frac{\mathrm{d}\theta_{\mathrm{FK}}}{\mathrm{d}r}(0) = \theta_{\mathrm{FK}}(1) = 0. \tag{A.23}$$

The associated temperature along the axis $\theta(\hat{x}, 0)$ is seen to approach $\theta(\hat{x}, 0) = 2\ln[2/(1+\sqrt{1-\delta/2})]$ for $x \gg 1$, with the limiting value $\theta(\hat{x}, 0) = 2\ln 2$ reached for the critical case $\delta = 2$.

On the other hand, for $\delta > 2$ the transition stage ends with a thermal runaway at a finite downstream location $\hat{x}_t = x_t - x_d \sim 1$. An interesting finding of the numerical integrations of the ignition problem (A.21), illustrated in the transient histories on the left-hand side of Fig. A.3, is that the thermal runaway occurs at the axis for values of δ in the range $2 < \delta \lesssim 6.68$, whereas for $\delta \gtrsim 6.68$ the thermal runaway occurs in an increasingly thinner annular reacting layer at an intermediate radius, not far from the wall, while the gas in the center is still cold. A similar behavior was identified in (Liñán *et al.*, 2016) in connection with the transient ignition history in spherical containers.

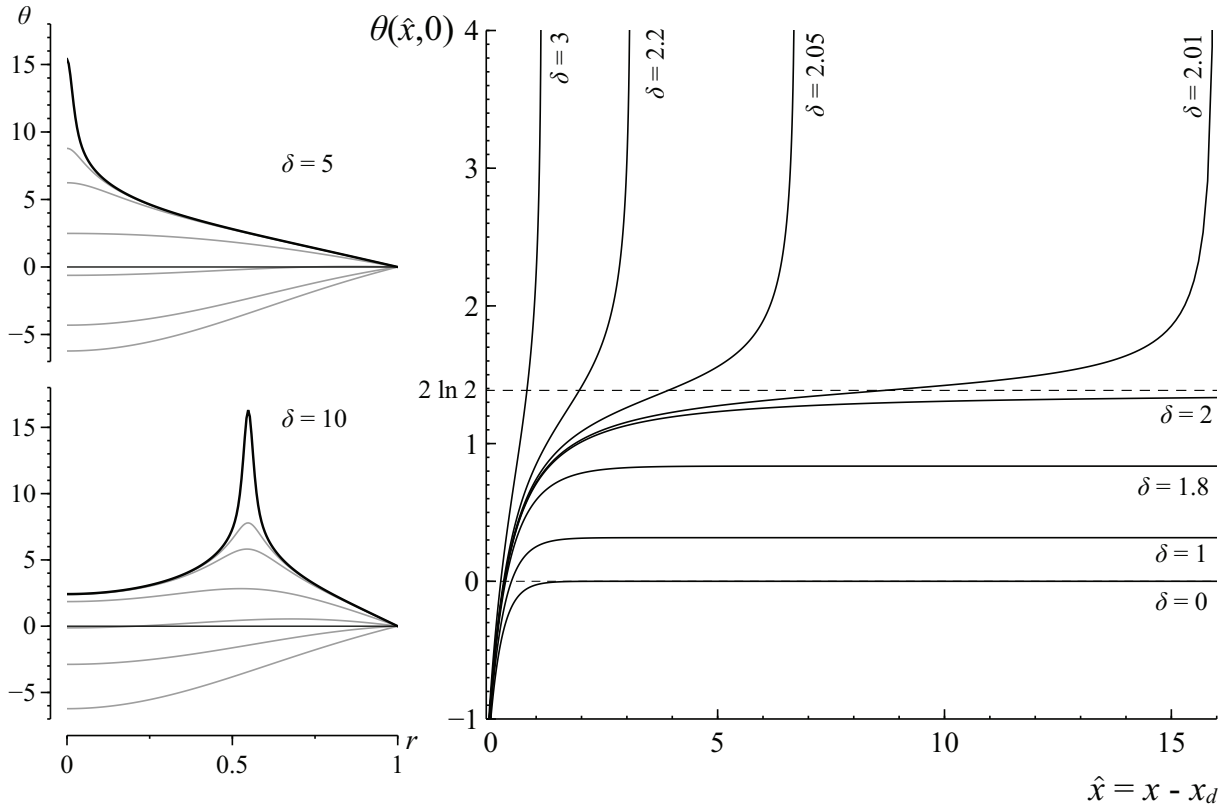

Figure A.3: The temperature evolution obtained by integration of (A.21) with the initial and boundary conditions given in (A.19) and (A.20) for different values of δ, including the evolution with distance of the temperature along the axis $\theta(\hat{x}, 0)$ for subcritical and supercritical cases along with selected temperature profiles for $\delta = 5$ $[\hat{x} = (0, 0.999, 4.999, 9.299, 9.678, 9.686, 9.687)]$ and $\delta = 10$ $[\hat{x} = (0, 2.010, 4.826, 5.933, 6.028, 6.032, 6.033)]$.

The resulting thermal-runaway location $\hat{x}_t$, a decreasing function of δ, is shown in Fig. A.4. The ignition distance computed here differs by a factor of order unity from that computed earlier in (Barenblatt *et al.*, 1997), where integrations of (A.21) were started with an initially uniform gas temperature, equal to the wall value. The present analysis, accounting for the presence of the reaction-free entry region, provides a prediction for the distance from the entrance of the pipe x'_t at which ignition occurs, given in nondimensional form $x_t = x'_t/[G/(\pi\rho'_o D_T)]$ by

$$x_t = x_d(T_I, \beta) + \hat{x}_t(\delta) = (2/\lambda_1^2)\ln C + (2/\lambda_1^2)\ln\beta + \hat{x}_t, \tag{A.24}$$

written with use made of (A.16). As can be seen, the value of x_t results from the addition of three separate terms that carry the influence of T_I, β, and δ, respectively. The first and third terms are given in Figs. A.2 and A.4, respectively, whereas the second term can be readily evaluated using $2/\lambda_1^2 \simeq 0.274$.

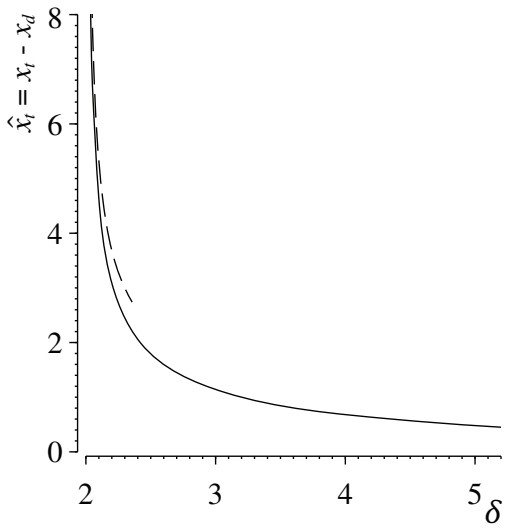

Figure A.4: The variation with $\delta > 2$ of the thermal-runaway distance $\hat{x}_t = x_t - x_d$, with the dashed curve representing the near-critical asymptotic result (A.32).

A.7 Ignition for near-critical conditions $\delta - 2 \ll 1$

For $0 < \delta - 2 \ll 1$ the thermal runaway occurs at very large distances $\hat{x}_t \gg 1$. As can be inferred from the results for $\delta = 2.01$ shown on the right-hand side of Fig. A.3, for these near-critical conditions the ignition history includes a relatively short initial period $\hat{x} \sim 1$, where the temperature increases to approach the critical FK profile $\theta_{\rm FK} = 2\ln[2/(1+r^2)]$ corresponding to $\delta = 2$, followed by a long quasi-steady evolution for $\hat{x} \sim (\delta-2)^{-1/2} \gg 1$ with $\theta - 2\ln[2/(1+r^2)] \sim (\delta-2)^{1/2} \ll 1$ which ends with a thermal runaway. This second stage can be investigated in terms of the asymptotically small parameter $\varepsilon = \delta/2 - 1$ to determine the resulting value of $\hat{x}_t \sim \varepsilon^{-1/2} \gg 1$.

The development begins by writing (A.21) in terms of the rescaled coordinate $\xi = \varepsilon^{1/2}\hat{x}$ and the off-equilibrium temperature departure $\theta - 2\ln[2/(1+r^2)] = \varepsilon^{1/2}\Theta(\xi, r)$ to give

$$2(1-r^2)\varepsilon\frac{\partial\Theta}{\partial\xi} = \frac{\varepsilon^{1/2}}{r}\frac{\partial}{\partial r}\left(r\frac{\partial\Theta}{\partial r}\right) + \frac{8}{(1+r^2)^2}\left[(1+\varepsilon)\mathrm{e}^{\varepsilon^{1/2}\Theta} - 1\right]. \tag{A.25}$$

Introducing the expansion $\Theta = \Theta_1 + \varepsilon^{1/2}\Theta_2 + \cdots$ and collecting terms of order $\varepsilon^{1/2}$ leads to

$$\frac{1}{r}\frac{\partial}{\partial r}\left(r\frac{\partial\Theta_1}{\partial r}\right) + \frac{8\Theta_1}{(1+r^2)^2} = 0; \qquad \frac{\partial\Theta_1}{\partial r} = 0 \text{ at } r = 0 \quad \text{and} \quad \Theta_1 = 0 \text{ at } r = 1, \tag{A.26}$$

which can be integrated to give

$$\Theta_1 = F(\xi)\frac{1-r^2}{1+r^2}. \tag{A.27}$$

The unknown function $F(\xi)$, carrying the streamwise dependence of the off-equilibrium temperature departure, can be obtained from the problem arising at order ε

$$\frac{1}{r}\frac{\partial}{\partial r}\left(r\frac{\partial\Theta_2}{\partial r}\right) + \frac{8\Theta_2}{(1+r^2)^2} = Q(\xi, r); \qquad \frac{\partial\Theta_2}{\partial r} = 0 \text{ at } r = 0 \quad \text{and} \quad \Theta_2 = 0 \text{ at } r = 1, \tag{A.28}$$

where

$$Q = 2\frac{(1-r^2)^2}{1+r^2}\frac{\mathrm{d}F}{\mathrm{d}\xi} - \frac{8}{(1+r^2)^2}\left[1+\frac{1}{2}\left(\frac{1-r^2}{1+r^2}\right)^2 F^2\right]. \tag{A.29}$$

Existence of solutions to the inhomogeneous problem (A.28) requires that $\int_0^1 Q(1-r^2)r/(1+r^2)\mathrm{d}r = 0$, providing the ordinary differential problem

$$\frac{1}{2}\frac{\mathrm{d}F}{\mathrm{d}\xi} = \frac{1+(F/2)^2}{17-12\ln 4}; \qquad F(0) = -\infty, \tag{A.30}$$

where the initial condition $F(0) = -\infty$ follows from matching with the upstream region $\hat{x} \sim 1$ of rapid temperature increase. The solution

$$F = 2\tan\left(\frac{\xi}{17-12\ln 4} - \frac{\pi}{2}\right) \tag{A.31}$$

diverges as $\xi \to \xi_t = (17-12\ln 4)\pi$, as corresponds to a thermal-runaway distance

$$\hat{x}_t = \varepsilon^{-1/2}\xi_t = \frac{(17-12\ln 4)\sqrt{2}\pi}{(\delta-2)^{1/2}} \simeq 1.62(\delta-2)^{-1/2}. \tag{A.32}$$

This asymptotic prediction is shown as a dashed curve in Fig. A.4.

As noted earlier in connection with the homogeneous ignition problem (Kassoy & Liñán, 1978), reactant consumption, not accounted for in the ignition equation (A.21), would necessarily become significant in configurations with sufficiently small values of $\delta - 2$, thereby modifying the result (A.32) as well as the thermal explosion limiting condition $\delta = 2$, with associated departures $\delta - 2$ that can be anticipated to be of order $1/(\alpha\beta) \ll 1$ (Liñán *et al.*, 2016).

A.8 Downstream flameless combustion for $\delta \leq 2$

For subcritical values of the Damköhler number $\delta \leq 2$ the temperature in the pipe evolves towards the quasi-steady distribution (A.22) for moderately large values of $\hat{x}$. Most of the reactant consumption, negligibly small in the entrance and transition regions, occurs downstream, at distances of order $\alpha\beta\ell$, such that the rescaled coordinate $X = (x - x_d)/(\beta\alpha)$ is of order unity, when (A.17) and (A.18) become

$$\frac{2}{\alpha\beta}(1-r^2)\frac{\partial\theta}{\partial X} = \frac{1}{r}\frac{\partial}{\partial r}\left(r\frac{\partial\theta}{\partial r}\right) + Y\delta \mathrm{e}^{\theta}, \tag{A.33}$$

$$2(1-r^2)\frac{\partial Y}{\partial X} = \frac{\alpha\beta}{Le\, r}\frac{\partial}{\partial r}\left(r\frac{\partial Y}{\partial r}\right) - Y\delta \mathrm{e}^{\theta}, \tag{A.34}$$

to be solved with the boundary conditions given earlier. Equation (A.34) indicates that during this second stage transverse diffusion of the reactant is so fast that its mass fraction remains spatially

uniform across the pipe at leading order, so that $Y \simeq \bar{Y}(X)$ with errors of order $1/(\alpha\beta)$, while the temperature evolves in a quasi-steady manner as dictated by

$$\frac{1}{r}\frac{\partial}{\partial r}\left(r\frac{\partial \theta}{\partial r}\right) + \bar{Y}\delta \mathrm{e}^{\theta} = 0, \tag{A.35}$$

the limiting form of (A.33) for $\beta\alpha \gg 1$.

As can be inferred from (A.23), the solution to (A.35) subject to $\partial\theta/\partial r = 0$ at $r = 0$ and $\theta = 0$ at $r = 1$ is just given by

$$\theta = 2\ln\left\{\frac{2/(1+\sqrt{1-\delta\,\bar{Y}/2})}{1+(\delta\,\bar{Y}/2)[r/(1+\sqrt{1-\delta\,\bar{Y}/2})]^2}\right\} \tag{A.36}$$

obtained by writing the FK temperature distribution (A.22) with δ replaced by the instantaneous Damköhler number $\delta\,\bar{Y}$. The evolution of $\bar{Y}(X)$ is given by

$$\frac{\mathrm{d}\bar{Y}}{\mathrm{d}X} = -2\int_0^1 \delta\,\bar{Y}\mathrm{e}^{\theta} r\mathrm{d}r, \qquad \bar{Y}(0) = 1, \tag{A.37}$$

obtained by integrating (A.34) multiplied by r, with use made of the non-permeability condition $\partial Y/\partial r = 0$ at $r = 1$. Since the energy balance is quasi-steady, the surface integral in (A.37), representing the overall rate of reactant consumption across the pipe, is proportional to the rate of heat transfer to the wall, as can be seen by using (A.35) to write (A.37) in the alternative form

$$\frac{1}{2}\frac{\mathrm{d}\bar{Y}}{\mathrm{d}X} = \int_0^1 \frac{\partial}{\partial r}\left(r\frac{\partial\theta}{\partial r}\right)\mathrm{d}r = \left(\frac{\partial\theta}{\partial r}\right)_{r=1}, \qquad \bar{Y}(0) = 1, \tag{A.38}$$

involving the reduced heat-loss rate to the wall

$$-\left(\frac{\partial\theta}{\partial r}\right)_{r=1} = \frac{\delta\bar{Y}}{1+\sqrt{1-\delta\,\bar{Y}/2}} \tag{A.39}$$

evaluated with use made of (A.36). Substituting (A.39) into (A.38) and integrating the resulting separable equation finally yields

$$\delta X = \left(1-\frac{\delta}{2}\right)^{1/2} - \left(1-\frac{\delta\bar{Y}}{2}\right)^{1/2} - \ln\left[\frac{1-\left(1-\delta\bar{Y}/2\right)^{1/2}}{1-(1-\delta/2)^{1/2}}\right] \tag{A.40}$$

as an implicit representation for the reactant mass fraction as a function of the rescaled streamwise distance $X = (x - x_d)/(\alpha\beta)$. The above expression applies for subcritical cases with $\delta \leq 2$.

A.9 Accuracy of the analytical predictions

The leading-order asymptotic analyses given above provide predictions of ignition distances for $\delta > 2$ and of slow flameless reactant consumption for $\delta < 2$ that apply strictly in the

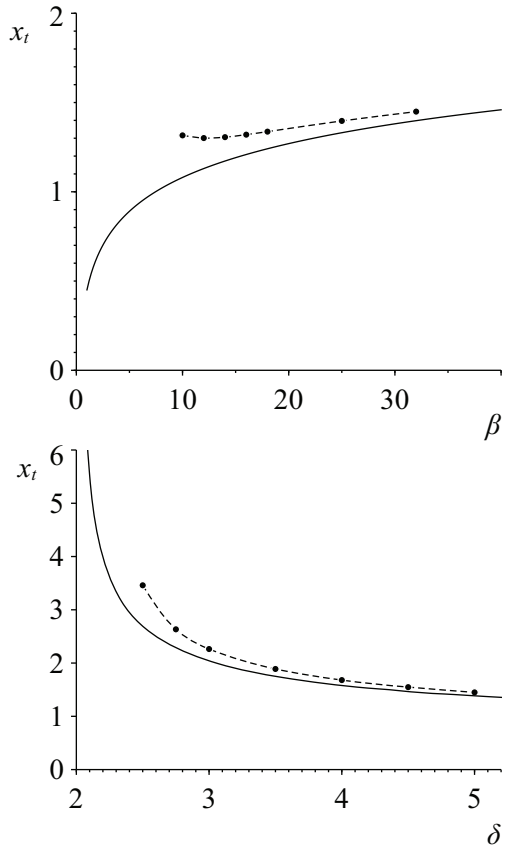

Figure A.5: The ignition distance for $T_I = 0.5$ obtained with the inflection-point criterion from numerical integrations of (A.6)–(A.13) for $\sigma = 0.7$, $Pr = 0.7$, $Le = 1.0$, and $\alpha = 5$ (circles) and evaluated with the asymptotic prediction (A.24) (solid lines). The upper plot shows the variation of x_t with β for $\delta = 5.0$ while the lower plot shows the variation of x_t with δ for $\beta = 32$.

limit $\beta \gg 1$. It is therefore worthwhile to test the accuracy of these predictions for large but finite values of β by comparing the analytical results with numerical integrations of the starting equations (A.6)–(A.13).

We begin by comparing in Fig. A.5 the ignition distance predicted by the expression (A.24) with that obtained numerically, with the inflection-point criterion employed to give a precise definition of x_t in the computations. A first set of computations, shown in the upper plot, consider increasing values of β for a fixed value of $\delta = 5$. The accuracy of the asymptotic results is seen to improve for increasing β, yielding corresponding relative errors that decrease in proportion to β^{-1}, as expected from the ordering of the corrections in the asymptotic description.

A second set of computations, for a fixed value of $\beta = 32$, considers ignition histories for different values of δ. The results are shown in the bottom plot of Fig. A.5. As can be seen, the accuracy of the prediction degrades as the ignition distance increases for smaller values of δ. The observed departures are attributable to the effect of reactant consumption, neglected in our leading-

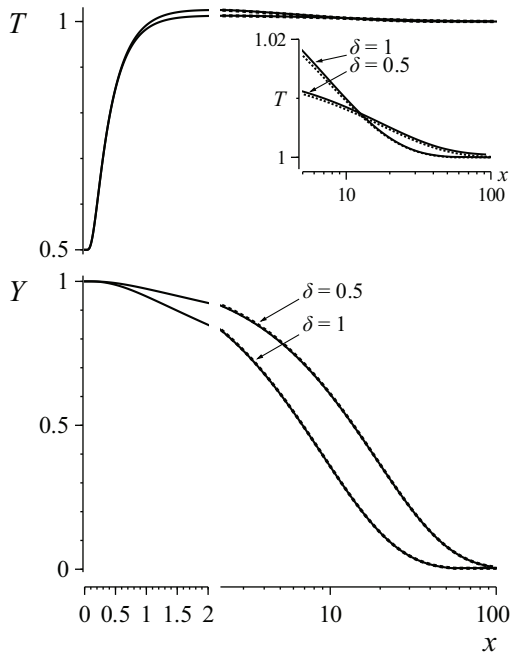

Figure A.6: The solid curves represent the evolution of the temperature and reactant mass fraction along the axis obtained by numerical integration of (A.6)–(A.13) with $\sigma = 0.7$, $Pr = 0.7$, $Le = 1.0$, $\beta = 10$, $\alpha = 5$, and $T_I = 0.5$ for two different subcritical values of δ, whereas the dashed curves are the predicted value of $\bar{Y}$, obtained by evaluating (A.40) with use made of $X = (x - x_d)/(\beta\alpha)$ and (A.16), and of the accompanying temperature along the axis, determined from (A.41).

order analysis, which becomes more noticeable for longer residence times, slowing down the reaction rate and leading to values of x_t that are larger than those predicted by (A.24). Incorporation of these reactant-consumption effects in the asymptotic analysis would require consideration of corrections of order β^{-1}, following the methodology developed earlier for the homogeneous problem (Kassoy & Liñán, 1978).

According to the asymptotic results, in the flameless mode of combustion established in the pipe for $\delta \leq 2$ the resulting reactant mass fraction, uniform across the pipe, decreases slowly with $X = (x - x_d)/(\beta\alpha)$ as dictated by (A.40), whereas the temperature increment from the wall value $T - 1 \sim \beta^{-1}$ follows the quasi-steady distribution (A.36), with a corresponding value at the axis given by

$$T(x, 0) = 1 + 2\beta^{-1} \ln \left[2 \Big/ \left(1 + \sqrt{1 - \delta\, \bar{Y}/2} \right) \right] . \tag{A.41}$$

These predictions are shown in Fig. A.6 along with numerical results for $\beta = 10$ and $\delta = (0.5, 1.0)$, the latter shown as solid curves. As can be seen, the dashed curves representing the analytical results fall on top of the solid curves from $x \sim 1$ all the way to the reactant depletion region, located at $x \simeq 50$ for $\delta = 1$ and at $x \simeq 100$ for $\delta = 0.5$. The degree of agreement achieved is

truly remarkable, indicating that the leading-order results developed here are sufficiently accurate to describe reactant consumption in flameless combustion in pipes for large but finite values of β.

A.10 Concluding remarks

The flow of an initially cold reactant mixture in a hot cylindrical pipe at moderately large values of the Reynolds number has been analyzed in the limit of large activation energies. The flow includes an entrance region where the gas temperature adapts to the wall value, followed by a shorter region of incipient reaction where the flow evolves to give either a rapid thermal runaway leading to the generation of a flame or a quasi-steady flameless mode of combustion that persists downstream along the pipe. Appropriate rescaled problems have been formulated and analyzed in the different regions, leading to predictions for the ignition distance in supercritical cases and for the slow downstream reactant consumption encountered in subcritical cases.

While the present analysis pertains only to the classical one-step Arrhenius heat-release description underlying the FK theory, future studies of flameless combustion in pipes incorporating realistic chemistry are clearly worth pursuing, using for instance reduced chemical-kinetic mechanisms, an approach that has been found to be useful in developing analytical predictions of explosion limits for hydrogen-oxygen systems (Sánchez *et al.*, 2014; Sánchez & Williams, 2014). Also, extensions of the analysis to address more general boundary conditions for the temperature at the wall could be attempted, for instance by consideration of a Newtonian heat–exchange law, as done previously for thermal explosions in closed vessels (Zel'dovich *et al.*, 1985). Effects of buoyancy-induced motion are also worth exploring, including modifications to the critical value $\delta = 2$ arising from enhanced heat-transfer rates, which could be described for small Rayleigh numbers using a perturbation analysis similar to that performed in Chapter 5.

This chapter, in part, has been published in *Combustion and Flame*, "Large-activation-energy analysis of gaseous reacting flow in pipes", by D. Moreno-Boza, I. Iglesias and A. L. Sánchez (2017) **178**, 217-224. The dissertation author is the primary investigator in this publication.

Bibliography

Barenblatt, G.I., Chorin, A.J. & Kast, A. 1997 The influence of the flow of the reacting gas on the conditions for a thermal explosion. *Proceedings of the National Academy of Sciences* **94** (24), 12762–12764.

Davenport, M.E. & Leppert, G. 1965 The effect of transverse temperature gradients on the heat transfer and friction for laminar flow of gases. *J. Heat Transfer* **87** (2), 191–196.

Dold, J.W. 1985 Analysis of the early stage of thermal runaway. *Quart. J. Mech. Appl. Math.* **38** (3), 361–387.

Dold, J.W. 1989 Analysis of thermal runaway in the ignition process. *SIAM Journal on Applied Mathematics* **49** (2), 459–480.

Driscoll, T.A., Hale, N. & Trefethen, L.N. 2014 *Chebfun Guide*. Pafnuty Publications, Oxford.

Frank-Kamenetskii, D.A. 1939 The temperature distribution in a reaction vessel and the time-independent theory of thermal explosions. *Zh. Fiz. Khim.* **13**, 738–755.

Frank-Kamenetskii, D.A. 1955 *Diffusion and heat exchange in chemical kinetics*. Princeton University Press.

Higuera, F.J. 2011 Laminar flow of a gas in a tube with large temperature differences. *Phys. Fluids* **23** (12), 123602.

Kagan, L., Berestycki, H., Joulin, G. & Sivashinsky, G. 1997 The effect of stirring on the limits of thermal explosion .

Kassoy, D.R. & Liñán, A 1978 The influence of reactant consumption on the critical conditions for homogeneous thermal explosions. *Quart. J. Mech. Appl. Math.* **31** (1), 99–112.

Kays, W.M. & Nicoll, W.B. 1963 Laminar flow heat transfer to a gas with large temperature differences. *J. Heat Transfer* **85**, 329–338.

Liñán, A., Moreno-Boza, D., Iglesias, I., Sánchez, A.L. & Williams, F.A. 2016 The slowly reacting mode of combustion of gaseous mixtures in spherical vessels. part 1: Transient analysis and explosion limits. *Combust. Theory Modelling* **20** (6), 1010–1028.

Liu, T.-Y., Campbell, A.N., Cardoso, S.S.S. & Hayhurst, A.N. 2008 Effects of natural convection on thermal explosion in a closed vessel. *Phys. Chem. Chem. Phys.* **10** (36), 5521–5530.

Liu, T.-Y., Campbell, A.N., Hayhurst, A.N. & Cardoso, S.S.S. 2010 On the occurrence of thermal explosion in a reacting gas: The effects of natural convection and consumption of reactant. *Combust. Flame* **157** (2), 230–239.

Pletcher, R.H., Tannehill, J.C. & Anderson, D. 2012 *Computational fluid mechanics and heat transfer*. CRC Press.

Rosner, D. E 2012 *Transport processes in chemically reacting flow systems*. Courier Corporation.

Sánchez, A.L., Iglesias, I., Moreno-Boza, D., Liñán, A. & Williams, F.A. 2016 The slowly reacting mode of combustion of gaseous mixtures in spherical vessels. part 2: Buoyancy-induced motion and its effect on the explosion limits. *Combust. Theory Modelling* **20** (6), 1029–1045.

Sánchez, A.L. & Williams, F. A. 2014 Recent advances in understanding of flammability characteristics of hydrogen. *Prog. Energy Combust. Sci.* **41**, 1–55.

Sánchez, A. L, Fernández-Tarrazo, E. & Williams, F. A 2014 The chemistry involved in the third explosion limit of h 2–o 2 mixtures. *Combust. Flame* **161** (1), 111–117.

Spalart, P.R., Moser, R.D. & Rogers, M.M. 1991 Spectral methods for the navier-stokes equations with one infinite and two periodic directions. *J. Comput. Phys.* **96** (2), 297–324.

Van Dyke, M 1964 Laminar boundary layers. edited by l. rosenhead. oxford university press, 1963. 688pp. ae4. 10s. *J. Fluid Mech.* **18** (3), 477–480.

Worsøe-Schmidt, P.M. & Leppert, G. 1965 Heat transfer and friction for laminar flow of gas in a circular tube at high heating rate: Solutions for hydrodynamically developed flow by a finite-difference method. *Int. J. Heat Mass Transfer* **8** (10), 1281–1301.

Zel'dovich, I.A., Barenblatt, G.I., Librovich, V.B. & Makhviladze, G.M. 1985 Mathematical theory of combustion and explosions. *Consultants Bureau, New York, NY* .